RESPONSE AND FAILURE MECHANICS OF STRUCTURAL MEMBER UNDER HIGH VELOCITY IMPACT

MD. JAHIDUL ISLAM

NATIONAL UNIVERSITY OF SINGAPORE

2011

RESPONSE AND FAILURE MECHANICS OF STRUCTURAL MEMBER UNDER HIGH VELOCITY IMPACT

MD. JAHIDUL ISLAM

(BSc. (Hons), BUET)

A THESIS SUBMITTED

FOR THE DEGREE OF DOCTOR OF PHILOSOPHY

DEPARTMENT OF CIVIL AND ENVIRONMENTAL ENGINEERING

NATIONAL UNIVERSITY OF SINGAPORE

2011

ACKNOWLEDGEMENTS

"*In the name of Allah, Most Gracious, Most Merciful*"

I would like to express my sincere thanks and gratitude to my supervisors, Professor Somsak Swaddiwudhipong and Dr. Liu Zishun for their constant encouragement and guidance during the course of my study and the preparation of this thesis. Their guidance and advice have contributed immeasurably to the successful completion of this thesis. Their patience, direction and suggestions have been very encouraging throughout my research project. I would also like to thank Professor Wang Chien Ming and Dr Qian Xudong for their helpful suggestions and comments.

My heartfelt appreciation is dedicated to Dr Kazi Md Abu Sohel and Dr Lee Siew Chin for their contributions and continuous supports. I am very appreciative of all the kind assistance from the staff members of the NUS Concrete and Structural Engineering Laboratory.

Finally, I would like to thank my parents and my sisters for their encouragement, devoted help and support for my study. I also wish to express my appreciation to all my friends and colleagues who have assisted me during the course of this research.

TABLE OF CONTENTS

SUMMARY

Response of structures under dynamic loading like high velocity projectile impact is a subject of great interest among practicing as well as research engineers. Among various approaches, namely, experimental, analytical and numerical, the latter supplemented by certain experimental verification is most promising, since it provides detailed comprehensive information which can be used to validate and improve engineering designs. For a successful numerical analysis, it is essential to implement an efficient discretization method and a robust material model. The purpose of this study is to develop a well organized numerical approach for high velocity impact studies of metallic plates and concrete slabs.

Numerical penetration and/or perforation studies involving finite element method (FEM) suffer from severe element distortion problem when subjected to high velocity impact. Severe element distortion causes negative volume problem and introduces numerical errors in the simulated results. This problem can be either resolved by implementing remedial measures, like element erosion approach or adopting meshfree methods. Element erosion approach is applied in the FEM by defining failure parameters as a condition for element elimination. Meshfree method, such as smooth particle hydrodynamics (SPH) method is capable of handling large deformation without any numerical problem, but at considerable computational resources. It is beneficial to adopt the coupled SPH – FEM (SFM) where the SPH is employed only in severely distorted regions and the FEM further away.

Effect of strain rate is significant for high velocity impact problems, and hence, two material models, modified Johnson – Cook (MJC) and modified

Holmquist – Johnson – Cook (MHJC) with an improved and effective strain rate expressions are proposed for metal and concrete, respectively. The MJC model includes a reasonably refined expression for adiabatic heating of metallic materials due to high strain rates. The MHJC model consists of simple but robust pressure-volume relationship for concrete subjected to high pressure and damage. Procedure for obtaining the MJC and MHJC model material properties are described. Both models are implemented as a user defined material model in a commercial software package LS-DYNA and verified against several high velocity impact problems.

The SFM is adopted to study high velocity perforation of steel, aluminum and titanium alloy Ti-6Al-4V target plates with varying thicknesses and various projectiles geometries. Effect of the SPH domain radius size is studied and it is found to be two to three times the projectile radius. The simulated residual velocities and the ballistic limit velocities from the SFM simulations exhibit good correlation with the published test data. The SFM is able to emulate the same failure mechanisms of the steel, aluminum and Ti-6Al-4V target plates as observed in various experimental investigations for initial impact velocity of 170 m/s and higher.

Element erosion approach is implemented for high velocity penetration and/or perforation study of concrete target plates. Maximum and minimum principal strains at failure are used as failure criteria. Since no direct method exists to determine these values, a calibration approach is used to establish suitable failure strain values. A range of erosion parameters is suggested and adopted in concrete penetration/perforation tests to validate the suggested values. Good correlation between the numerical and field data is observed.

Keywords: Finite element method (FEM), smooth particle hydrodynamics (SPH), high velocity impact, penetration, perforation, strain rate effects, adiabatic heating, material modeling.

LIST OF SYMBOLS

A_b	Area of pressure bar
A, B, a, C, b	Modified Johnson-Cook (JC) model parameters
$\mathcal{A}, \mathcal{B}, \mathcal{N}$	Modified Holmquist-Johnson-Cook (HJC) model constants
$[\boldsymbol{B}]$	Strain-displacement matrix
c	Sound velocity
C_C, C_T	Strain rate parameters
c_d	Damping parameter
C_k	Intercept of $u_s - u_p$ plot
C_0	Longitudinal wave velocity
C_p	Specific heat
c_s	Shear wave velocity
D	Damage
$[\boldsymbol{D}]$	Elasticity matrix
D	Diameter of the projectile
D_1 to D_5	JC model damage parameters
D_c	Critical damage
d_g, d_h	Damage constants for MHJC model
D_l, D_m	Damage constants for HJC model

d_p	SPH particle distance
D_p	Projectile shank diameter
E	Young modulus
e	Energy per unit mass
E_p	Plastic hardening modulus
E_t	Tangent modulus
F_{DIF}	Dynamic strength increase factor
f_b	Body force
f_t	Traction
f_c'	Unconfined compressive strength
$f_t^{'}$	Tensile strength
$\overline{f}_t^{'}$	Normalized tensile strength
G	Shear modulus
h	Smoothing length
h_s	Thickness of the target plate
I	Internal energy
I_1	First invariant of stress tensor
J_2	Second invariant of deviatoric stress tensor
K	Bulk modulus
$[K]$	Stiffness matrix
K_a	Modified bulk modulus

K_m, K_l, K_n	Material constants
K_I	Stress intensity factor
K_{IC}	Critical stress intensity factor
L	Length of the projectile
L_s	Projectile shank length
L_n	Projectile nose length
m	Mass
$[\boldsymbol{M}]$	Mass matrix
$[\boldsymbol{N}]$	Shape function matrix
o, q	Recht and Ipson model constants
P	Pressure
P^*	Normalized pressure
P_{comp}	Pressure for fully compacted concrete
P_{crush}	Crushing pressure
P_{lock}	Locking pressure
$P_{\max}, P_{\min}$	Maximum and minimum pressures at failure
$\Re$, $\wp$	Cowper-Symonds strain rate constants
r	Radius
S	Deviatoric stress
s	Surface area
$\dot{S}$	Deviatoric stress rate
s_1, s_2, s_3	Coefficient of $u_s - u_p$ plot

T	Temperature
t	Time
T_m	Melting Temperature
T_r	Room temperature
u	Displacement
u_p	Particle velocity
u_s	Shock velocity
$\ddot{u}$	Acceleration
V	Volume
v	Velocity
v_{bl}	Ballistic limit velocity
v_i	Initial impact velocity
v_r	Residual velocity
W	Smoothing kernel function
w	Work done
cfs	Compressive failure strain
tfs	Tensile failure strain
β	Percentage of plastic work converted to heat
γ_0	Gruneisen constants
Δ	Increment
ε	Strain
ε_p	Equivalent plastic strain
$\varepsilon_{\max}$, $\varepsilon_{\min}$	Maximum and minimum principal strains at failure

$\dot{\varepsilon}_0$	Reference strain rate
$\dot{\varepsilon}_p$	Plastic strain rate
ε_p^f	Plastic fracture strain
$\varepsilon_{\min}^f$	Minimum fracture strain
ε_{eff}^p	Effective plastic strain
$\varsigma, \zeta, \vartheta$	Constants
κ	Scalar factor
μ	Volumetric strain
μ_m	Volumetric strain of fully compacted concrete
μ_p	Equivalent volumetric strain
μ_f	Friction coefficient
μ_{comp}	Volumetric stain at P_{comp}
μ_{crush}	Crushing volumetric strain
μ_{lock}	Locking volumetric strain
$\bar{\mu}$	Modified volumetric strain
ν	Poisson's ratio
ξ	Problem dimension
Π	Artificial viscous pressure
ρ	Density
ρ_{grain}	Grain density
ρ_m	Density of fully compacted concrete

σ	Stress
σ_e	von-Mises stress
σ_y	Yield stress
σ_{ave}	Average of normal stresses
σ_{eq}	Equivalent stress
$\sigma_{\max}$	Maximum principal stress at failure
σ_{eq}^{f}	Equivalent stress at failure
σ_C^*	Normalized stress
σ_{eq}^*	Normalized equivalent stress
$\sigma_{\max}^*$	Normalized maximum strength
τ	Shear stress
χ	Geometric constants
Ω	Sub-domain of influence
ω	Rotation rate

LIST OF FIGURES

LIST OF TABLES

Chapter 1 Introduction

The response of structures and materials subjected to dynamic loading has been a subject of interest for military, civil, automotive and aeronautical engineering. Understanding of material failure under high velocity impact is essential in the analysis and design of protective structures. Protections for personnel and vehicles from bullet, missile and explosive require development of lightweight protection. Designing offshore structures too requires better understanding of high velocity impact problems like collision between objects, penetration of fragments, etc. In the automotive industries, crashworthiness and energy absorption capabilities for vehicles are major issues which can be studied using high velocity impact analysis. Protection of aircrafts and spacecrafts against impact of flying objects (such as debris, birds, etc) or meteoroids are still a major concern for aerospace industry.

1.1 Penetration and/or Perforation of Structures Under High Velocity Projectile Impact

Backman and Goldsmith (1978) defines "penetration of projectile" as, when a missile penetrates into a target but does not complete its progress through the target body. However, if a projectile bounces from the impact surface or moves along a curved path after entering the target and emerges with a reduced velocity from the target through impact surface is termed as "ricochet". On the other hand, when the projectile finishes its penetration completely, it is called "perforation" (Zukas, 1990). Figure 1.1 gives a schematic explanation of both penetration and perforation when a conical projectile impacts into a target plate.

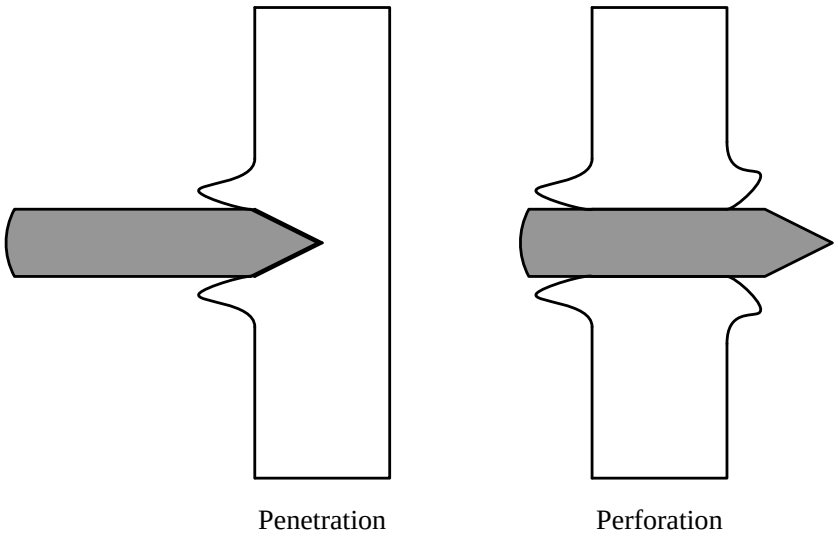

Figure 1.1 Penetration and perforation of target by conical nose projectile.

Projectile penetration and/or perforation related problems have been investigated for centuries and a lot of effort has been given to better understand the phenomenon involving colliding bodies. Various techniques, namely, experimental, analytical and numerical, have been developed to predict the resistance of structures under projectile impacts. Experimental investigations involve a large number of test results and empirical formulas. Despite being the best way to solve most problems, it has drawbacks including high cost, significant amount of time requirement for the experimental setup and specimen preparation, and the inability to use for others materials, geometries and impact velocities outside the test range. The analytical model is based on the development and use of the engineering model. Development of the analytical model involves the conservation of laws and deformation or failure mechanisms from test observations. The third approach is the numerical method which becomes more popular in recent years with the increasing advancement of the computational technology. Numerical models are capable of offering solutions with greater accuracy provided that a robust discretization method along with an appropriate material model is adopted. Although each method has its own merits and

demerits, the numerical approach is the most robust among them, since it provides detailed information exclusively which can be used to validate and improve engineering models at a reasonable cost.

Earlier numerical studies of high velocity impact were fundamentally based on the hydrodynamics theory of shock wave propagation through solids. Since the hydrodynamics theory did not include strength effects, solids were treated as fluid with no viscosity. Johnson (1977) introduced a Lagrangian finite element formulation with explicit time integration method for high velocity impact problems. Although the finite element method (FEM) has several advantages over other numerical methods, it has a major drawback. In the presence of large deformation, which is common for high velocity impact, mesh based FEM suffers from severe element distortions that cause several problems (Børvik et al., 2002; Camacho and Ortiz, 1997; Chou et al., 1988; Islam et al., 2011; Zukas, 1990). A deformed element has one very small side and one very long side. Since time steps in numerical simulations are calculated based on the smallest element length, an element with a small side increases the computational time unrealistically by reducing the time steps in each computational cycle. A longer element side also introduces errors by averaging the result over the length. Large deformation may also cause negative volume problems and therefore resulting in premature termination of the analysis.

Schwer and Day (1991) presented several techniques such as remeshing, element erosion, tunneling, local modified symmetry constraint and NABOR nodes techniques to solve the element distortion problem in the FEM. Among these remedial techniques, remeshing and element erosion methods are most popular. In remeshing approach, after some cycles or based on unacceptable element geometries, a new (more regular) mesh replaces the distorted mesh (Chou et al., 1988; Schwer and Day, 1991; Zukas, 1990). Although remeshing solves severe element distortion problems, it

suffers from several drawbacks such as, computationally expensive, projection error and reduction of the numerical analysis accuracy (Liu, 2002). In the element erosion method, severely distorted elements are removed or eroded from further analysis to allow the computational analysis to continue. The element erosion method is a widely adopted method because of its simplicity in implementation (Børvik et al., 2003; Chen, 1990, 1993; Dey, 2004; Holmquist et al., 1993; Johnson et al., 1998; Wilkins, 1978). The element erosion can be performed based on certain user defined failure criteria such as pressure, stress, strain, damage and/or temperature. However, to the author's knowledge, there are yet no direct approaches available to determine these erosion parameters.

Smooth particle hydrodynamics (SPH), a mesh-free method, is capable of handling large deformation in high velocity impact problems without severe element distortion problem. The SPH method was developed by Lucy (1977), and Gingold and Monaghan (1977). Although it was originally developed for astrophysics problem, it has been employed for the solid mechanics problems since early 1990s (Libersky and Petschek, 1991; Libersky et al., 1993). Liberksy et al. (1993) adopted a 3D-SPH code MAGI to simulate the metal cylinder impact and hyper velocity impact tests. The results obtained were comparable to the experimental data. Since then, the SPH method has been adopted in a number of impact and fracture related problems. Liu et al. (2002; 2004) successfully employed the SPH method to study the dynamic response of structures under high velocity impact.

Although the SPH method is a preferred choice for high velocity impact simulations, it is not that well developed as the FEM. It is computationally less efficient than the FEM and suffers from instability problems in certain conditions (Johnson, 1994). However, the significant factor of the SPH method is that it is Lagrangian based which allows it to link with the standard finite element Lagrangian

formulations (Attaway et al., 1994; Johnson, 1994; Johnson et al., 1993; Johnson et al., 1996). Therefore, by combining the SPH method with the FEM, where the SPH method is used at the region of large deformation and damage, and the FEM elsewhere, one obtains a logical development for high velocity projectile penetration/perforation simulations (Liu et al., 2010; Swaddiwudhipong et al., 2011). Although the coupling between the FEM and SPH is not a new idea, there are very few studies made to study the efficiency of the approach.

1.2 Materials

For the design of protective structures, various materials such as, steel, aluminum, titanium, concrete etc. are of particular interest. Steel and aluminum have high strength and ductility; titanium and titanium alloys have an excellent high strength to weight ratio; and concrete is a low cost material with wide applications.

1.2.1 Metals

Metals are an important class of materials and are characterized by some specific properties, namely, high strength and ductility, high electrical and thermal conductivity and characteristic luster of their surfaces (Rösler et al., 2007). Ductility and strength of metals can be increased further by alloying of metals. Steel, aluminum and titanium alloys are widely used for various protective structures, and hence, a brief discussion of three alloys, namely, Weldox 460 steel, AA5083-H116 aluminum and Ti-6Al-4V titanium are given.

Weldox 460 (the number indicates the yield strength in MPa) is a high strength steel with high ductility and better weldability. Its high strength is achieved by rolling it at a certain temperature along with a controlled cooling (SSAB, 1999). It is a ferrite-pearlite structure and pealite is the reason for high ductility in the material properties (Dey, 2004). Weldox 460 steel has been used for various structures like,

offshore structures, water towers, overhead travelling cranes, cranes, turbines, buildings, silos, bridges, etc.

Because of their excellent strength to weight ratio and good corrosion resistance, aluminum alloys are widely employed in marine structures (such as offshore topsides and ship hulls), automobile, sport equipment and aerospace industries. Particularly, aluminum-magnesium alloys (AA5XXX class) have high strength, excellent corrosion resistance and good welding quality which make them an excellent choice for transportation fields where reduced weight is desirable without compromising the structural integrity. These alloys are also used for military purpose against ballistic penetrators and low temperatures (Hatch, 1984). Aluminum-magnesium alloy AA5083-H116 is the second strongest alloy in AA5XXX class alloys (Børvik et al., 2004) where temper H116 is a special strain hardening treatment with special temperature control.

Titanium is the fourth most abundant structural element. It is known as the space-age element because of its superior mass efficiency and excellent corrosion resistance (Kirk-Othmer, 2010). Mass efficiency is the ratio of weight per unit area of rolled homogenous armor (RHA) steel over weight per unit area of test material. Titanium has 30% – 80% more mass efficiency compared to RHA (Burkins et al., 1996; Montgomery and Wells, 2001). The alpha phase titanium is stable up to the beta transus temperature of 882°C, beyond which and up to the melting temperature titanium exist in the beta phase (Burkins et al., 1996). The phase altering temperature can be shifted by adding alloys to titanium. Alpha beta alloys consist of both alpha and beta stabilizer alloys. Inclusion of alloying elements aluminum and vanadium in Ti-6Al-4V moves the beta transus temperature to 996°C. Ti -6Al-4V has high strength to weight ratio and toughness, and excellent resistance against corrosion which allow it to use in aerospace, defense and biomedical applications.

1.2.2 Concrete

Concrete has been used in civil engineering structures since early eighteenth century. It has been used for hardened shelters, bunkers, runways, and nuclear reactors. Concrete is a composite material involving aggregates (coarse and fine) and binding materials. It has several advantages, including the ability to be cast in any shape, durability, fire resistance, easy availability of the ingredients, cost effectiveness and high compressive strength. Low tensile strength and ductility are some of the most prominent disadvantages of concrete. But, by using reinforcement with the concrete, tensile strength and ductility of concrete can be increased to some degree.

1.3 Perforation of Metal Target

Residual and ballistic limit velocities are the most common notions to identify the structure performance against projectile penetration. There are several definitions of ballistic limit available in the literature. Among them, the most accepted definition is the Navy ballistic limit, reported in the Air Force Flight Dynamics Lab (1976) technical report. It is stated that, the ballistic limit velocity is the lowest projectile velocity that is required for the projectile to penetrate completely and to emerge from the target.

To date, significant advances have been observed in the ballistic studies of metals (such as steel, aluminum, titanium alloys, etc) at sub-ordnance (25 – 500 m/s) and ordnance (500 – 1300 m/s) velocity ranges (Backman and Goldsmith, 1978; Børvik et al., 2009; Børvik et al., 2003; Corbett et al., 1996; Corran et al., 1983; Dey, 2004; Wilkins, 1978; Zukas, 1990). Ballistic responses of targets under projectile impact are affected by several factors, like relative thicknesses of target and projectile geometries (Wilkins, 1978).

Pitler and Hulich (1950) noticed the potential of titanium alloys as lightweight armor application against smaller ballistic threats like fragment-simulating projectile

(FSP). The FSP with 20 mm diameter and 54 gm mass can simulate fragmentation of high-explosive shell explosion. Threats against the smaller ballistic projectiles are evaluated from the ballistic perforation tests. Because of the high cost of Ti-6Al-4V, very few studies have been performed to achieve the ballistic limit velocities. Burkins et al. (2001) performed penetration/perforation tests of the aerospace specification MIL-T-9046J titanium alloys Ti-6Al-4V to determine the ballistic limit velocities on various plate thicknesses. However, to the author's knowledge, no numerical study has been performed for Ti-6Al-4V with FSP an initial velocity ranging between 900-1300 m/s.

1.3.1 Target Thickness and Projectile Geometry Effects on Perforation of Metal Targets

Corran et al. (1983) investigated ballistic limit velocities of mild steel, stainless steel and aluminum alloy target plates of thickness between 1.3 – 6.4 mm against blunt projectiles of 12 mm diameter. All materials showed a change in pattern in the ballistic limit velocity versus thickness plots, especially in the range of 4 – 6 mm thicknesses. Børvik et al. (2003) observed similar behavior while conducting perforation of Weldox 460 E steel at sub-ordnance velocity range. Arne tool steel blunt projectiles with diameter of 20 mm were impacted against target plates with varying thicknesses ranging from 6 – 30 mm. For target plate thickness of 10 mm and/or less, ballistic limit velocities showed a change in pattern. Forrestal et al. (1990) conducted perforation of 5083-H131 aluminum target plates of various thicknesses (12.7 mm, 50.8 mm and 76.2 mm) by 8.31 mm diameter tungsten conical projectiles. Børvik et al. (2004) performed perforation tests of AA5083-H116 aluminum target plates with varying thicknesses (15 – 30 mm) impacted by 20 mm diameter Arne tool steel conical nose projectiles. In both cases, the ballistic limit versus target plate thickness plot showed a linear relationship indicating identical failure pattern for

various thicknesses. Above studies indicate a relationship between the failure pattern and the target plate thickness to the projectile diameter ratio, which can be attributed to the change in projectile energy absorption.

Projectile nose geometries play a significant role on the ballistic failure pattern of the target material, since it is related to the energy absorption for projectile perforation (Dey, 2004; Leppin and Woodward, 1986; Wilkins, 1978; Wingrove, 1973). Wingrove (1973) conducted perforation of 10 mm thick 2014 aluminum alloy by 7 mm diameter 4340 steel projectile with various nose geometries (blunt, hemispherical and ogival) and observed a change in target failure patterns. In the experiment, the blunt projectile showed the least resistance against penetration; whereas the conical projectile exhibited the most. Wilkins (1978) compared ballistic limit velocities for blunt and conical steel projectiles with 7.65 mm diameter perforating 4340 steel target plates of various thicknesses (6.35 – 9.5 mm). When the target plate was thick, the conical projectile required less energy for perforation than the blunt projectile. However, with decrease in target thicknesses an opposite trend was observed. Leppin and Woodward (1986) and Dey (2004) found similar behavior for aluminum and steel target materials, respectively. Studies indicate a distinct relationship between the ballistic limit velocity with the projectile nose geometry and target plate thickness.

1.3.2 Material Models for Metals

It is essential to adopt a suitable material model to describe material behaviors during impact simulations. Such models should be robust enough to include all the significant aspects of dynamic loadings, and it should be mathematically sound, computationally user friendly and requires minimum numbers of attainable constants. Mechanical behavior of metals, such as strength, ductility, etc., changes with the loading rates and temperatures. Therefore, it is imperative to include the strain rate

and temperature effects in the design of structural components for the high velocity impact, explosion and other dynamic problems.

Several constitutive models with a relatively small number of material constants are available for numerical simulations, like Johnson-Cook (JC), Zerilli-Armstrong (ZA), Bodner-Partom (BP), Khan-Huang-Liang (KHL), etc. Johnson and Cook (1983) developed the JC model for metals subjected to large strains, high strain rates and temperatures. It is well suited for implementing in computational codes and has a vast library of material parameters for various materials. The ZA model, proposed by Zerilli and Armstrong (1987), based on the dislocation mechanics with strain hardening, coupled strain rate and thermal effects. It has two forms, one for body-centered cubic (BCC) materials and one for face-centered cubic (FCC) materials. Unlike the JC model, strain hardening in the ZA for BCC materials is independent of strain rate and temperature, but it is a disadvantage for metals where strain hardening depends on strain rate and temperature (Liang and Khan, 1999). Bodner and Partom (1975) introduced the BP model for large deformations with a set of equations to represent elastic-viscoplastic strain-hardening material behavior. Bonder and Rubin (1994) and Bodner and Rajendran (1995) further modified the model by including an improved strain rate and temperature effects expressions. Khan and Liang (1999) formulated the Khan-Huang-Liang (KHL) model based on the work done by Khan and Huang (1992). In this model work-hardening is described as a coupled effect of strain and strain rate. Although all the constitutive models have their own advantages or disadvantages for certain materials, the JC model is universally used for most metals.

Failure due to adiabatic shear is common to high strain rates problems for metals (Børvik et al., 2001b; Chen et al., 2009; Dey et al., 2007; Dumoulin et al., 2010; Solberg et al., 2007). Taylor and Quinney (1934) mentioned that the work done

due to plastic deformation in metal was converted to heat. Dissipation of the heat depends on the thermal diffusion distance which is the distance of heat transfer during a time period, and hence, varies inversely with the strain rate. Thus the heat generated in the specimen by the plastic work remains within the specimen for high strain rates and considered to be an adiabatic condition. However, not all the converted heat remains within the material and a small portion of it is diffused mostly due to radiation and heat conduction. Temperature rise due to the adiabatic condition at high strain rates needs to include in the material models for metals. The JC model does not include this condition, and hence, a modification is needed.

1.4 Penetration and Perforation of Concrete

Study of the concrete structures while subjected to high velocity projectile impact is an intricate problem due to the complex response of concrete material. Under such loading condition, concrete exhibits strain rate sensitivity and complex damage.

1.4.1 Strain Rate Effect on Concrete Under High Velocity Impact

Dynamic loading tests on concrete have been conducted since early twentieth century. Several experimental results showed significant increase in concrete strength when subjected to either compressive or tensile higher loading rates (Bischoff and Perry, 1991; Gary and Klepaczko, 1992; Malvern et al., 1985; Mellinger and Birkimer, 1966; Ross et al., 1989). Limiting crack velocities (Tedesco et al., 1997) and the viscoelastic characteristics of the cement paste (Li and Meng, 2003) are two of the most prominent reasons behind strain rate sensitivity of concrete. Test results indicate that tensile strength increment under high strain rate is much more than the compressive strength increment and a critical strain rate exists beyond which a sharp increase in the strength occurs.

1.4.2 Numerical Analysis of Concrete Penetration and/or Perforation

Concrete and other geo-materials exhibit perfectly-plastic behavior when subjected to high confining pressures. However, strain softening response is evident when concrete is subjected to low confining pressures. Murray and Lewis (1995) proposed an elasto-plastic cap model involving concrete responses, like hardening, softening, dilation, degradation of modulus due to cyclic loading/unloading, damage accumulation and irreversible deformation. Plastic flow occurs due to the frictional movement of the microcrack surfaces which cause permanent deformation without any modulus degradation. Because of the complexity of the model, it requires a good number of material constants that makes it rather difficult to implement more frequently. Holmquist et al. (1993) and Riedel et al. (1999) developed the Holmquist-Johnson-Cook (HJC) and RHT concrete models respectively that consist of features like, high pressure, strain rate effect, material damage. Both models are almost similar except for a few cases, such as unlike the HJC model, the RHT includes a third invariant of deviatoric stress into the pressure-shear expression which is able to distinguish the compressive and tensile meridians. Taylor et al. (1986) introduced a microcrack based continuum damage model (TCK) which is able to calculate damage from nucleation and growth of randomly distributed cracks under tensile loading conditions. Although all the material models have their own advantages and disadvantages, the HJC model is popular for high velocity penetration and/or perforation, because of its lower number of material constants requirements compared to other models. However, the HJC model has a single expression for strain rate effect. It is not suitable for high strain rates since concrete behavior below and above the critical strain rate is different. Pressure-volume relationship is also quite complex and involves a good number of material constants. A further improvement and simplification is desired for the model.

Chen (1993) carried out the perforation study on 140 MPa strength concrete using a 2D axi-symmetric approach in LS-DYNA2D and compared the residual velocities with those measured by Hanchak et al. (1992). For concrete, Chen (1993) used the strain values of 0.15 and 1.0 as a failure criterion in the erosion algorithm along with the material model for compression and tension failure, respectively. Polanco-Loria et al. (2008) performed 2D axi-symmetric perforation study of both the 48 MPa and 140 MPa concretes (Hanchak et al., 1992) in LS-DYNA, and used failure strain value of 1.0. Furthermore, in a 2D axi-symmetric finite element analysis of ogive nose steel projectile penetration into concrete with unconfined compressive strength of 43 MPa, Johnson et al. (1998) simulated the penetration of the projectile with striking velocity of 315 m/s by using an erosion strain value of 3.0. Beissel and Johnson (2000) also chose a similar value for erosion while carrying out a 2D axi-symmetric penetration of concrete by ogive-nose steel projectile in a Lagrangian hydrocode. Although these numerical results were in good agreement with the experimental data, a wide range of erosion parameter values were used for different perforation/penetration cases and none of them were consistent. Therefore, further studies are required to find a consistent set of failure parameters which can be used for ogive-nose projectiles penetration/perforation problems of concrete targets.

1.5 Failure Mechanisms

To understand the penetration and/or perforation process, it is necessary to have a very good idea of the failure patterns of the target. Common failure mechanisms in ductile target are dishing, radial flow, plugging, discing, adiabatic shear failure, ductile fracture, spalling and petaling (Backman and Goldsmith, 1978; Woodward, 1984; Zukas, 1990). Failure of target materials can happen by any individual or in combination of the above mentioned failure mechanisms. Brittle failures only involve fragmentation and spalling. A detail illustration of various

failure patterns are shown in Figure 1.2. Failure patterns are demonstrated based on the target thicknesses and projectile geometries. A simple classification of target thickness can be given based on the ratio of target plate thickness, h_s to projectile diameter, d. The target plate is considered a thick plate when the ratio is more than one, and a thin plate otherwise (Zukas, 1990).

Projectile shape and strength, and the target thickness affect the target failure mechanism. In case of a hard sharp pointed projectile penetration into a soft ductile target, the projectile produces high stress enough to surpass the target shear strength and the projectile progress through the target by laterally moving the material. However, a thin target plate is dished away from the sharp projectile by bending and stretching and the failure occurs by dishing. When a blunt nosed projectile impacts a thick target with a high velocity, material in front of the projectile in the target is forced to move in the direction of impact which causes extensive shear deformation in the target, along the periphery of the projectile. Adiabatic shear failure occurs due to lack of heat conduction (possible when subjected to high strain rate) near the shear zone in the target plate, which results in thermal softening of materials. When thermal softening rate in the target material surpasses the work hardening rate, material in the narrow shear zone becomes softer and the additional deformation of material occurs throughout the plate thickness, until fracture occurs by plugging. For thin plate, in addition to adiabatic shear failure with plug diameter less than the projectile diameter, radial flow of the material is observed during the impact event (Leppin and Woodward, 1986).

When a projectile impacts a brittle material, like concrete, localized failure of material is observed. At the loading surface concrete fails primarily due to compression by crushing of materials along the path of the projectile while creating a crater region. Compression waves develop and travel toward the opposite surface and

after reflecting at the free surface these waves are converted into tensile waves. Because of the low tensile strength of concrete, tensile failure occurs at the opposite surface in the form of spalling. In between these two regions, failure occurs in the tunnel region in terms of compaction at high confining pressure. Size of the tunnel region increases with the slab thickness.

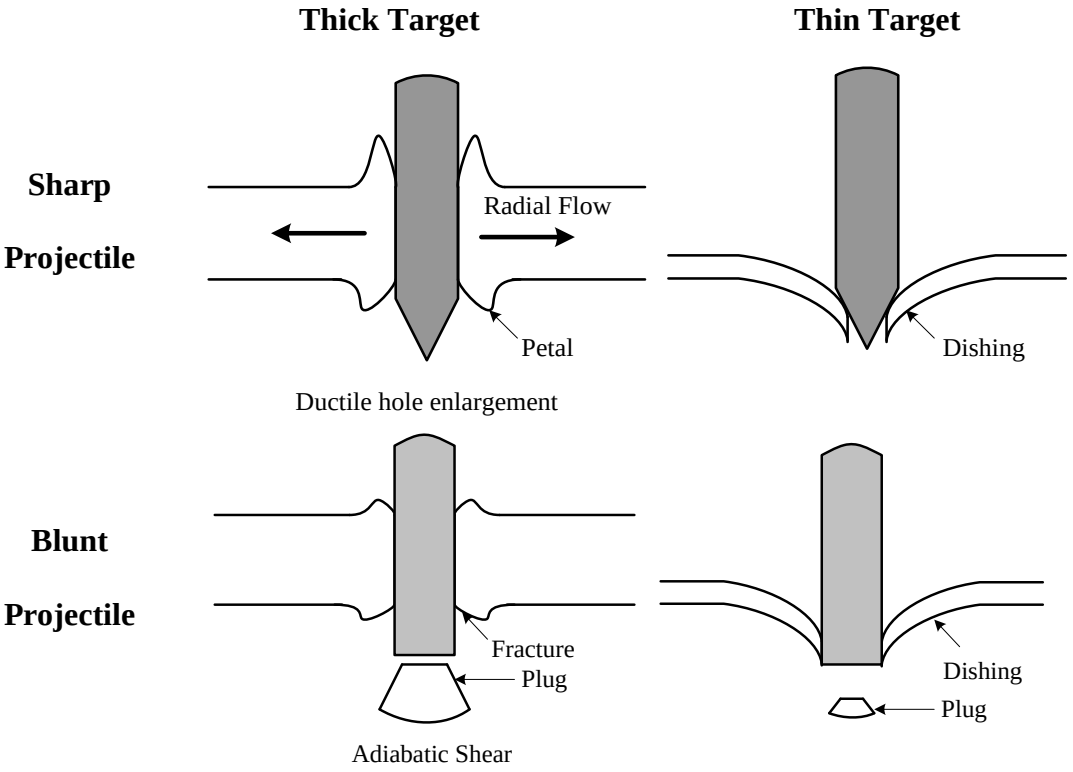

Figure 1.2 Different failure modes during projectile penetration/perforation process.

1.6 Observations From Literature Review

The above literature review indicates that the FEM is currently the most popular choice for high velocity impact studies. However, the FEM is subjected to severe element distortion problem when adopted for high velocity impact simulations and requires special remedial approaches, like element erosion, remeshing, etc. Because of its simplicity in implementation, element erosion method is widely used, but inconsistent since there is no direct approach available to determine the erosion

criteria. Further studies are required to find a consistent set of erosion criteria for an intended target material. Another option to avoid severe element distortion is to use the coupled SPH-FEM (SFM). Although the SFM method has been proposed already, very few studies have been conducted to fully understand its potential. Literature review also pointed out that the metal target failure patterns depend on the target plate thickness to projectile diameter ratio and projectile nose geometry. The SFM can be implemented to study the failure patterns in more details and calculate the ballistic limit and residual velocities.

The JC and HJC models are widely used for high velocity impact simulations of metals and concrete, respectively. The JC model incorporates large strain, high strain rates, temperature and damage effects in the constitutive model. However, it does not include temperature effect due to the adiabatic condition at high strain rates. Strain rate expression is also subjected to instability in case of very low strain rates, and hence, a modification is required. Improvement of the mater model should include a power law expression for strain rate to rectify the numerical instability problem. Furthermore, an additional expression is needed to calculate the temperature rise due to adiabatic condition in high velocity impact problems.

Strain rate expression in the HJC model does not reflect the physical behavior of concrete at high strain rates. Concrete behave differently under compression and tension loading conditions. Furthermore, pressure-volume characteristic of the HJC model is complex and requires triaxial test results which are very hard to achieve. Therefore, it is essential to propose a new model for concrete.

1.7 Objectives and Scope of the Study

The objective of this research is to propose a robust approach for numerical study of high velocity impact problems involving metallic plates and concrete slabs. Although experimental results are essential, numerical methods give complete

analysis of the problems. For a successful numerical simulation, it is essential to adopt an efficient material model with a small number of attainable material constants and an efficient discretization method. Although there are several material models available in the literature, they are not robust enough. Furthermore, it is essential to choose an efficient numerical approach with best possible outcome. Hence, the objectives of this study are as follows:

1. To propose and verify two simple but effective material models with a limited number of material constants for metallic plates and concrete slabs subjected to high velocity impact.
2. To adopt the coupled SPH-FEM (SFM) for high velocity impact perforation of metal target plates.
3. To develop the finite element (FE) model with element erosion method for high velocity impact penetration and/or perforation of concrete targets.

To achieve the aforementioned objectives, the scope of this research includes:

1. Proposing a constitutive model for metals with emphasis on strain rate and adiabatic temperature effects. Simple steps to determine the material constants for the proposed material model and validation of the model by comparing the numerical results with the test data for problems subjected to high strain rates and temperature increments due to adiabatic conditions.
2. Development of a concrete constitutive model for high velocity impact studies with an efficient strain rate expression and a simple pressure-volume relationship, and verifying the proposed model for various penetration/perforation problems.
3. Application of the SFM for high velocity impact simulation of steel and aluminum alloy targets where the SPH method is used at the region of large deformation and damage, and the FEM elsewhere. Study of SPH domain

radius size and particle distance, friction and impact velocity effects for the proposed method.

4. Numerical simulation of titanium, steel and aluminum alloy target plates using the proposed material model and the SFM. Comparisons of the numerical residual and ballistic limit velocities with the test data.
5. Determination of element erosion parameters for the FEM simulation of concrete penetration and/or perforation based on the correlation with the experimental results. Verification of the parameters when applied for other penetration and/or perforation studies.

1.8 Organization of the Thesis

Organization of the remainder of the thesis is as follows. In Chapter 2, the governing equations of the finite element method (FEM) and smooth particle hydrodynamics (SPH) method are presented. Kernel function, artificial viscosity and variable smoothing length of the SPH method are described. The linking between the SPH and the FEM in the coupled SPH-FEM (SFM) is proposed. The governing equations for three material models, two for metals and one for concrete and equation of state are illustrated. Finally, the element erosion algorithm which is used with the FEM in high velocity impact simulations is included in this chapter.

In Chapter 3, two material models, modified Johnson-Cook (MJC) model for metals and modified Holmquist-Johnson-Cook (MHJC) model for concrete, are developed. Material constants identification procedures for the proposed MJC model are presented. Governing equations of the MHJC model are discussed. Finally, determination of the material properties of the MHJC model is presented.

In Chapter 4, the study of domain size, particle distance and friction effects in the SFM method are adopted. Using the SFM, the effect of target thickness and projectile nose geometries in high velocity impact perforations of steel are performed.

High velocity perforation simulations of aluminum alloy target plates with various thicknesses are included. The numerical residual and ballistic limit velocities are compared with the experimental observations.

In Chapter 5, the MJC model is validated by simulating two numerical examples, including a split Hopkinson pressure bar (SHPB) test of titanium alloy Ti-6Al-4V and perforation of 6 mm thick Weldox 460 E steel target plate. A number of other numerical examples are presented to demonstrate the validity of the proposed MJC model and SFM at impact velocity ranging from 100 – 1200 m/s. The examples involving perforation of titanium, steel and aluminum alloy targets. Residual and ballistic velocities from the numerical simulations are judged against the test data.

In Chapter 6, erosion parameters for concrete are investigated. Three examples including two perforation and one penetration simulations of concrete are adopted for determining the erosion parameters. The numerical results are compared with experimental data. For perforation cases, residual velocities and for the penetration case, penetration depths are evaluated. The erosion parameters are adopted in three penetration studies to validate the values. The verification of the MHJC model is conducted by simulating perforation of concrete target plate with a compressive strength of 48 MPa. Penetration studies are conducted using the proposed MHJC model along with element erosion in the finite element analysis.

Finally, concluding remarks of the present study are summarized in Chapter 7.

Chapter 2 Numerical Modeling

2.1 Introduction

In impact problems, dominant factors are shock wave propagation and energy absorption involving both high loading rate and minuscule response time. Therefore, detail characterization of these problems require high-speed photographic and other special measurements and hence it is difficult and most of the time expensive to attain experimentally. Therefore, various numerical methods such as finite element method (FEM), meshfree methods, finite difference method (FDM), extended finite element method (XFEM), generalized finite element method (GFEM), etc, become popular alternatives supplementing experimental techniques in impact phenomena.

In numerical methods, governing equations are solved over a spatial mesh or set of particles at successive time steps. FEM is one of the leading discretization procedures in engineering analysis. It is applied widely in the analyses of solids and structures and of fluids and heat transfer. In fact it is used in virtually every engineering analysis in recent years. In the FEM, a continuum is divided into discrete elements, which are connected together by a mesh. However, FEM has few limitations including failure to model the disintegration of the material domain accurately for the damaged mechanics. In order to improve the discretization approximation, new methods have been sought for, and indeed meshfree methods are developed under such extensive search. Unlike the FEM, meshfree methods do not require mesh to define the problem domain. Interpolation approximations are developed based on the scattered particles over the domain and on the boundary. Because of the changeable nodal connectivity principle, meshfree methods are

suitable for problems with large deformations. Meshfree methods like smooth particle hydrodynamics (SPH), element free Galerkin (EFG), etc, are employed successfully in various complex simulations such as damage, underwater explosion, crack growth, etc. However, the EFG method requires background mesh to perform numerical integrations, and hence, it is subjected disintegration problem while applied for damage analysis.

Despite having problem with severe element distortion problem, the FEM with remedial techniques is widely used for high velocity impact problems. The SPH method can easily handle problems involving large deformation and damage; however, it has its own disadvantages like tensile instability and is computationally more expensive. Because of that the SPH method has not been widely used for high velocity impact studies in the past. All the numerical simulations are performed in the commercial software package LS-DYNA.

2.2 Numerical Methods

2.2.1 Finite Element Method (FEM)

Finite element discretization method is widely used for various engineering problems through standard computer codes. Formulation of the FEM can be established using the displacement method normally through the principle of virtual work. Consider a three-dimensional (3D) body occupying volume *V* subjected to traction $f_{t_i}(t)$ over a portion of outer surface s_t and external body force $f_{b_i}(t)$ and the body is supported on the area s_s with prescribed displacement $u_i(t)$. Virtual work principle requires that:

$$\int_V \rho \ddot{u}_i \delta u_i dV + \int_V \sigma_{ij} \delta u_{i,j} dV - \int_V \rho f_{b_i} \delta u_i dV - \int_{s_t} f_{t_i} \delta u_i ds = 0 \tag{2.1}$$

where, ρ is the material density, σ_{ij} is the Cauchy's stress tensor, $\ddot{u}_i$ is the acceleration and δu_i is the arbitrary virtual displacement. The comma implies the covariant differentiation. Applying finite element spatial discretization of Eqn. (2.1), the governing equation becomes:

$$\left[\boldsymbol{M}\right]\left\{\ddot{\boldsymbol{u}}\right\}+\left[\boldsymbol{K}\right]\left\{\boldsymbol{u}\right\}=\left\{\boldsymbol{F}\right\} \tag{2.2}$$

where,

$$\left[\boldsymbol{M}\right]=\sum\int_{V_e}\rho\left[\boldsymbol{N}\right]^t\left[\boldsymbol{N}\right]dV_e \tag{2.3}$$

$$\left[\boldsymbol{K}\right]=\sum\int_{V_e}\left[\boldsymbol{B}\right]^t\left[\boldsymbol{D}\right]\left[\boldsymbol{B}\right]dV_e \tag{2.4}$$

in which, $\left[\boldsymbol{M}\right]$, $\left[\boldsymbol{K}\right]$, $\left[\boldsymbol{N}\right]$, $\left[\boldsymbol{D}\right]$ and $\left[\boldsymbol{B}\right]$ are the mass, stiffness, shape function, elasticity and strain-displacement matrices, V_e is the element volume and $\left\{\boldsymbol{F}\right\}$ is the equivalent nodal force vector of combined internal and external forces including those derived from the restitution of the bodies during the impact.

In dynamic analysis of structure energy dissipation is observed due to damping. The effect of damping can be considered by including velocity-dependent damping forces (d'Alembert's principle) as a part of the body force. After introducing damping force into Eqn. (2.2) we get,

$$\left[\boldsymbol{M}\right]\left\{\ddot{\boldsymbol{u}}\right\}+\left[\boldsymbol{C}\right]\left\{\dot{\boldsymbol{u}}\right\}+\left[\boldsymbol{K}\right]\left\{\boldsymbol{u}\right\}=\left\{\boldsymbol{F}\right\} \tag{2.5}$$

where, $\left[\boldsymbol{C}\right]$ is the damping matrix,

$$\left[\boldsymbol{C}\right]=\sum\int_{V_e}c_d\left[\boldsymbol{N}\right]^t\left[\boldsymbol{N}\right]dV_e \tag{2.6}$$

in which, c_d is the damping parameter.

Finite element governing equations can be formulated using either of the two approaches: Lagrangian or Eulerian. Details of the two formulations can be found in Anderson (1987) and Bathe (1996). In the Lagrangian formulation, FE mesh deforms and follows the material motion. Throughout the analysis process, each element mesh represents the same material piece, which it is defined for initially. Deformation, velocity, density, pressure, etc., are measured for each nodes of the element as time progresses. Mass of the element is constant in this formulation; however element volume may change with time due to compression/expansion of material. Advantages of this method are that, material interfaces and boundary conditions are easier to define as well as material stress histories can be defined more conveniently throughout the problem domain. However, for high velocity impact problem, Lagrangian formulation subjected to severe mesh distortion and negative volume problems. Severely distorted element reduces time step size, and hence causes unnaturally long computational time. It also reduces the computational accuracy of the deformed region.

In the Eulerian formulation, mesh is fixed in space and material flows through it. In general, the Eulerian mesh consists of rectangular grid of elements larger than the Eulerian material boundaries, to allow the flow and deformation of material. The Eulerian calculation approach is divided into two steps. In every time step, Lagrangian calculations are performed for nodes with temporarily fixed position and to follow it with a remapping of the deformed elements. Since Eulerian has no element distortion problem it can be used for fluid and gaseous problems and also in high velocity impact problems. However, it has certain disadvantages including difficulties in defining deformable material boundaries and contact between the projectile and the target bodies, making the method inapt for ballistic penetration and/or perforation study (Camacho and Ortiz, 1997). It is also computationally much

more expensive than the Lagrangian formulation. Because of these reasons, Lagrangian finite element formulation is adopted in this study.

2.2.2 Smooth Particle Hydrodynamics (SPH) Method

The SPH method was first developed by Lucy (1977), Gingold and Monaghan (1977) to describe astrophysics phenomena. The system is represented by a set of particles, and the variables are calculated using the smoothing kernel functions.

2.2.2.1 Kernel Approximation

The integral representation or kernel approximation of a function *f(x)* over a compact sub-domain of influence, Ω, and its divergence can be expressed as

$$\langle f(x)\rangle \cong \int_{\Omega} f(x')W(x-x',h)\,dx' \tag{2.7}$$

$$\langle \nabla . f(x)\rangle \cong -\int_{\Omega} f(x').\nabla W(x-x',h)\,dx' \tag{2.8}$$

where, *W* is the smoothing kernel function and *h* is the smoothing length that is a unit measure of the domain of influence of function *W* (Figure 2.1). The smoothing kernel function has to satisfy following properties:

- normalized in each sub-domain:

$$\int_{\Omega} W(x-x',h)\,dx' = 1 \tag{2.9}$$

- compact support, i.e.,

$$W(x-x',h) = 0 \text{ for } |x-x'| \geq 2h \tag{2.10}$$

- reduces to Dirac-delta function, when $h \to 0$

$$\lim_{h\to 0} W(x-x',h) = \delta(x-x') \tag{2.11}$$

The kernel approximation and its divergence can be written in terms of arbitrary set (*n*) of discrete interpolation points,

$$\langle f(x_i)\rangle \approx \sum_{j=1}^{n} f_j\left(x_j\right) W\left(x_i - x_j, h\right)\frac{m_j}{\rho_j} \tag{2.12a}$$

$$\approx \sum_{j=1}^{n} f_j W_{ij}\frac{m_j}{\rho_j} \tag{2.12b}$$

$$\langle \nabla . f(x_i)\rangle \approx -\sum_{j=1}^{n} f_j\left(x_j\right).\nabla W\left(x_i - x_j, h\right)\frac{m_j}{\rho_j} \tag{2.13a}$$

$$\approx \sum_{j=1}^{n} f_j.\nabla W_{ij}\frac{m_j}{\rho_j} \tag{2.13b}$$

where, i and j represents the particle number; m_j and ρ_j are the mass and density associated with particle *j*, respectively.

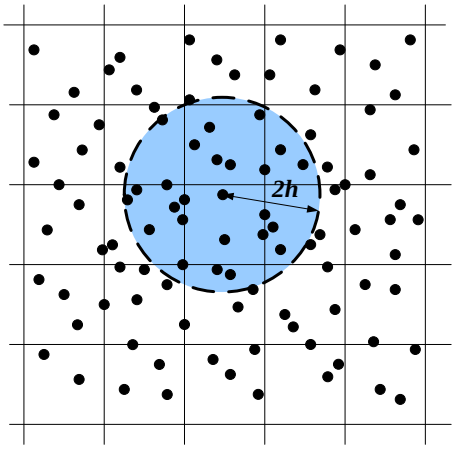

Figure 2.1 SPH particles with circular domain of influence.

2.2.2.2 Equation of Motion

The general forms of the conservation of mass, momentum and energy in solid mechanics are,

$$\frac{d\rho}{dt} = -\rho\frac{\partial v^{\alpha}}{\partial x^{\alpha}} \tag{2.14}$$

$$\frac{dv^{\alpha}}{dt} = \frac{1}{\rho}\frac{\partial \sigma^{\alpha\beta}}{\partial x^{\beta}} \tag{2.15}$$

$$\frac{de}{dt}=\frac{\sigma^{\alpha\beta}}{\rho}\frac{\partial v^{\alpha}}{\partial x^{\beta}} \tag{2.16}$$

where, v and e are the velocity and energy per unit mass respectively.

Using the chain rule, Eqs. (2.14-2.16) can be written as,

$$\frac{d\rho}{dt}=-\rho\frac{\partial v^{\alpha}}{\partial x^{\alpha}}=-\frac{\partial\left(\rho v^{\alpha}\right)}{\partial x^{\alpha}}+v^{\alpha}\frac{\partial\rho}{\partial x^{\alpha}} \tag{2.17}$$

$$\frac{dv^{\alpha}}{dt}=\frac{1}{\rho}\frac{\partial\sigma^{\alpha\beta}}{\partial x^{\beta}}=\frac{\partial}{\partial x^{\beta}}\left(\frac{\sigma^{\alpha\beta}}{\rho}\right)+\frac{\sigma^{\alpha\beta}}{\rho^{2}}\frac{\partial\rho}{\partial x^{\beta}} \tag{2.18}$$

$$\frac{de}{dt}=\frac{\sigma^{\alpha\beta}}{\rho}\frac{\partial v^{\alpha}}{\partial x^{\beta}}=\frac{\sigma^{\alpha\beta}}{\rho^{2}}\left[\rho\frac{\partial v^{\alpha}}{\partial x^{\beta}}\right]=\frac{\sigma^{\alpha\beta}}{\rho^{2}}\left[\frac{\partial\left(\rho v^{\alpha}\right)}{\partial x^{\beta}}-v^{\alpha}\frac{\partial\rho}{\partial x^{\beta}}\right] \tag{2.19}$$

Based on Eqs. (2.17-2.19) and the kernel approximation theory, the SPH governing equations are expressed as:

$$\left\langle\rho\frac{\partial v^{\alpha}}{\partial x^{\alpha}}\right\rangle\approx W\left(\rho v^{\alpha}\right)-\int v^{\alpha}\rho\frac{\partial W}{\partial x^{\alpha}}dV$$

$$\approx 0-\sum_{j=1}^{n}\left(v_j^{\alpha}-v_i^{\alpha}\right)\rho_j\frac{\partial W_{ij}}{\partial x^{\alpha}}\frac{m_j}{\rho_j}$$

$$\left\langle\frac{d\rho_i}{dt}\right\rangle\approx-\sum_{j=1}^{n}(v_i^{\alpha}-v_j^{\alpha})m_j\frac{\partial W_{ij}}{\partial x^{\alpha}} \tag{2.20}$$

$$\left\langle\frac{1}{\rho}\frac{\partial\sigma^{\alpha\beta}}{\partial x^{\beta}}\right\rangle\approx W\left(\frac{\sigma^{\alpha\beta}}{\rho}\right)+\int\frac{\sigma^{\alpha\beta}}{\rho^{2}}\rho\frac{\partial W}{\partial x^{\beta}}dV$$

$$\approx 0+\sum_{j=1}^{n}\left(\frac{\sigma_j^{\alpha\beta}}{\rho_j^{2}}-\frac{\sigma_i^{\alpha\beta}}{\rho_i^{2}}\right)\rho_j\frac{\partial W_{ij}}{\partial x^{\beta}}\frac{m_j}{\rho_j}$$

$$\left\langle\frac{dv_i^{\alpha}}{dt}\right\rangle\approx-\sum_{j=1}^{n}\left(\frac{\sigma_i^{\alpha\beta}}{\rho_i^{2}}-\frac{\sigma_j^{\alpha\beta}}{\rho_j^{2}}\right)m_j\frac{\partial W_{ij}}{\partial x^{\beta}} \tag{2.21}$$

$$\left\langle\frac{\sigma^{\alpha\beta}}{\rho}\frac{\partial v^{\alpha}}{\partial x^{\beta}}\right\rangle\approx\frac{\sigma^{\alpha\beta}}{\rho^{2}}\left[W\left(\rho v^{\alpha}\right)-\int v^{\alpha}\rho\frac{\partial W}{\partial x^{\beta}}dV\right]$$

$$\approx \frac{\sigma^{\alpha\beta}}{\rho^2}\left[0-\sum_{j=1}^{n}\left(v_j^{\alpha}-v_i^{\alpha}\right)\rho_j\frac{\partial W_{ij}}{\partial x^{\beta}}\frac{m_j}{\rho_j}\right]$$

$$\left\langle\frac{de_i}{dt}\right\rangle \approx \frac{\sigma_i^{\alpha\beta}}{\rho_i^2}\sum_{j=1}^{n}(v_i^{\alpha}-v_j^{\alpha})m_j\frac{\partial W_{ij}}{\partial x^{\beta}} \tag{2.22}$$

2.2.2.3 Kernel Function

For the SPH algorithm, kernel function is an important part. Cubic B-spline is the most commonly used smoothing kernel function which can be expressed as:

$$W(q,h)=\frac{\kappa}{h^{\xi}}\begin{cases}1-(3/2)q^2+(3/4)q^3 & q\le 1\\ (1/4)(2-q)^3 & 1<q\le 2\\ 0 & q>2\end{cases} \tag{2.23}$$

where, $q=\left(x_i-x_j\right)/h$, ξ (= 1, 2 or 3) is the dimension of the problem and κ is the scalar factor to comply with Eq. (2.7). Three values of κ corresponding to ξ (= 1, 2 or 3) are 2/3, 10/7π and 1/π, respectively. The 3D cubic B-spline kernel function ξ = 3, h =1 and $\kappa = 1/\pi$) is demonstrated in Figure 2.2.

Derivatives of the cubic B-spline kernel function are shown as:

$$\frac{dW}{dq}=\frac{\kappa}{h^{\xi}}\begin{cases}3\left(-q+(3/4)q^2\right) & q\le 1\\ -(3/4)(2-q)^2 & 1<q\le 2\\ 0 & q>2\end{cases} \tag{2.24}$$

$$\frac{d^2W}{dq^2}=\frac{\kappa}{h^{\xi}}\begin{cases}3\left(-1+(3/2)q\right) & q\le 1\\ (3/2)(2-q) & 1<q\le 2\\ 0 & q>2\end{cases} \tag{2.25}$$

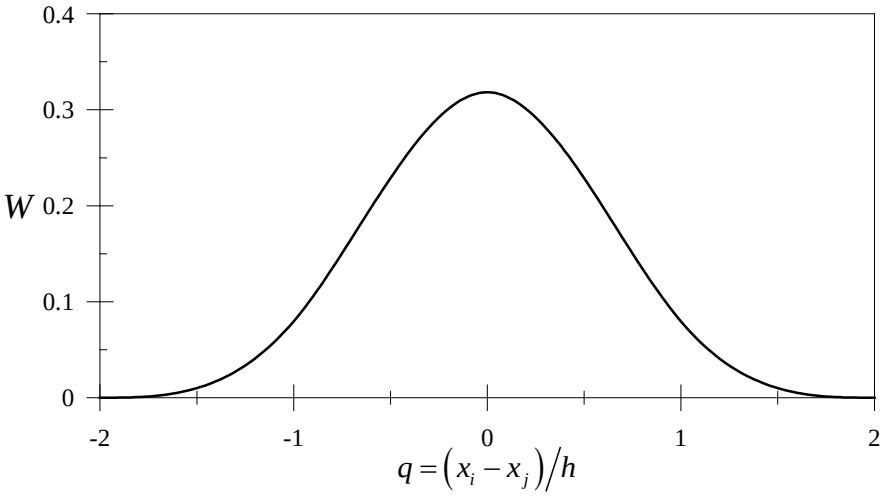

Figure 2.2 Cubic B-spline kernel function for 3D.

2.2.2.4 Artificial Viscosity

Simulation of shock waves in SPH method may cause spurious oscillations in both the pressure and the velocity fields (Li and Liu, 2004). In order to overcome the shock induced numerical instabilities, Monaghan and Gingold (1983) proposed including an artificial viscous pressure term (Π_{ij}) into the SPH equations. The artificial viscous pressure is expressed as,

$$\Pi_{ij} = \begin{cases} \dfrac{-\varsigma \bar{c}_{ij}\phi_{ij} + \zeta\phi_{ij}}{\bar{\rho}_{ij}} & \text{if} \quad (v_i - v_j)\cdot(x_i - x_j) < 0 \\ 0 & \text{otherwise} \end{cases} \tag{2.26}$$

where,

$$\phi_{ij} = \frac{h(v_i - v_j)\cdot(x_i - x_j)}{|x_i - x_j|^2 + \vartheta h^2} \tag{2.27}$$

$$\bar{c}_{ij} = (c_i + c_j)/2, \qquad \bar{\rho}_{ij} = (\rho_i + \rho_j)/2 \tag{2.28}$$

In Eq. (2.26), c is the sound speed, ς, ζ and ϑ are the constants. The SPH governing equations with the artificial viscosity term,

$$\left\langle \frac{d\rho_i}{dt} \right\rangle \approx -\sum_{j=1}^{n} (v_i^\alpha - v_j^\alpha) m_j \frac{\partial W_{ij}}{\partial x^\alpha} \tag{2.29}$$

$$\left\langle \frac{dv_i^\alpha}{dt} \right\rangle \approx -\sum_{j=1}^{n} \left(\frac{\sigma_i^{\alpha\beta}}{\rho_i^2} - \frac{\sigma_j^{\alpha\beta}}{\rho_j^2} + \Pi_{ij} \right) m_j \frac{\partial W_{ij}}{\partial x^\beta} \tag{2.30}$$

$$\left\langle \frac{de_i}{dt} \right\rangle \approx \sum_{j=1}^{n} \left(\frac{\sigma_i^{\alpha\beta}}{\rho_i^2} + \frac{\Pi_{ij}}{2} \right) (v_i^\alpha - v_j^\alpha) m_j \frac{\partial W_{ij}}{\partial x^\beta} \tag{2.31}$$

2.2.2.5 Constitutive Equation

In the elastic regime, the deviatoric stress rate can be determined through Hooke's law,

$$\dot{S}^{\alpha\beta} = 2G\dot{\varepsilon}' \tag{2.32}$$

where, G is the shear modulus and $\dot{\varepsilon}'$ is the deviatoric strain rate tensor.

To account for the finite rotation effect, Eq. (2.32) can be rewritten using the Jaumann rate definition as follows,

$$\dot{S}^{\alpha\beta} = 2G\left(\dot{\varepsilon}^{\alpha\beta} - \frac{1}{3}\delta^{\alpha\beta}\dot{\varepsilon}^{\gamma\gamma} \right) + S^{\alpha\gamma}\omega^{\beta\gamma} + S^{\gamma\beta}\omega^{\alpha\gamma} \tag{2.33}$$

where, strain rate and rotation rate are defined as,

$$\dot{\varepsilon}^{\alpha\beta} = \frac{1}{2}\left(\frac{\partial v^\alpha}{\partial x^\beta} + \frac{\partial v^\beta}{\partial x^\alpha} \right) \tag{2.34}$$

$$\omega^{\alpha\beta} = \frac{1}{2}\left(\frac{\partial v^\alpha}{\partial x^\beta} - \frac{\partial v^\beta}{\partial x^\alpha} \right) \tag{2.35}$$

The strain rate and rotation rate tensors are described as,

$$\dot{\varepsilon}_i^{\alpha\beta} = \frac{1}{2}\sum_{j=1}^{n} \frac{m_j}{\rho_j} \left[(v_i^\alpha - v_j^\alpha) \frac{\partial W_{ij}}{\partial x^\beta} + (v_i^\beta - v_j^\beta) \frac{\partial W_{ij}}{\partial x^\alpha} \right] \tag{2.36}$$

$$\omega_i^{\alpha\beta} = \frac{1}{2}\sum_{j=1}^{n} \frac{m_j}{\rho_j} \left[(v_i^\alpha - v_j^\alpha) \frac{\partial W_{ij}}{\partial x^\beta} - (v_i^\beta - v_j^\beta) \frac{\partial W_{ij}}{\partial x^\alpha} \right] \tag{2.37}$$

The Von Mises J_2 criterion and the associated flow rule are normally adopted to describe the plastic deformation in the type of target materials studied herein. For a high velocity impact problem, severe hydrostatic pressure is developed and usually evaluated via Mie-Gruneisen Equation of State (EOS) for solids.

2.2.2.6 Variable Smoothing Length

The smoothing length (*h*), describe the region of influence of the neighboring particles. The SPH method is subjected to tensile instability which causes clustering of particles and premature tensile failure (Liu et al., 2002). This problem can be resolved by employing more particles with a constant smoothing length or using a constant number of particles with a varying smooth length. Although the constant smoothing length approach requires less computational effort for most engineering applications, it is not suitable for penetration/perforation studies. In penetration/perforation problems, targets are subjected to both compression and tension and hence a constant smoothing length will increase the particle numbers inside the influence sub-domain, which will eventually increase the computational effort. Therefore, a varying smoothing length with a constant number of particles inside an influence sub-domain is a better option. In such a case, it is essential to keep the number of particles and the mass in the influence sub-domain unchanged in both time and space. The total mass *M* of a spherical influence sub-domain of radius *2h* with *n* number of particles can be expressed as:

$$M = n \times m = n \times \rho \times \frac{4}{3}\pi \left(2h\right)^3 = \frac{32}{3}\pi n \rho h^3 \tag{2.38}$$

To keep the mass of the influence sub-domain unchanged (i.e. $dM/dt = 0$), the conservation of mass requires that

$$\frac{d\rho}{dt} = -\rho \mathbf{div}\left(v\right) \tag{2.39}$$

$$\frac{dh}{dt} = \frac{1}{3} h \mathbf{div}(v) \tag{2.40}$$

where $\mathbf{div}(v)$ is the divergence of the flow. Smoothing length increases/decreases with the increasing/decreasing particle distances. The field variables in the SPH governing equations, Eqs. (2.29-2.31), can be directly updated using an explicit, leap-frog time integration algorithm.

2.2.2.7 Tensile Instability Management

SPH method is subjected to tensile instability problem (Liu, 2002). Because of this, SPH simulation may suffer a premature fracture and/or failure in tension. Therefore, it is essential to manage this problem. The stress-point method can be implemented to contain this problem and improve accuracy of the results in SPH simulations (Dyka et al., 1997; Liu, 2002). In this method, stress, density and internal energy values are calculated at points other than the centroid of the particles. The stress points are symmetrically located at a parametric distance away from the centroid of the particles. This method is similar to the full integration approach in the FEM.

2.2.3 Coupled SPH-Finite Element Method (SFM)

Both FEM and SPH methods have certain advantages and disadvantages which when combined, enhance their performance further. To optimize the computational resources, in the coupled SPH-FEM method (SFM), the SPH particles are employed in the region of large deformation and damage, while the rest of the domain is modeled by the finite element (FE) mesh. Compared to the SPH method, the SFM is able to reduce the requirement of computational resources significantly by lowering the number of SPH particles. Application of the SPH method is limited to selected regions of very large deformation, fracture and damage to mitigate any

numerical problems encountered in the FE approach. Moreover, using the FEM for the rest of the domain improves the accuracy of the results.

Both SPH and FE methods are based on the Lagrangian formulation. The SPH method can be easily included in an existing Lagrangian based FEM by considering SPH particles as elements with one node. Schematic overview of the Lagrangian SPH and FEM as shown in Figure 2.3 elaborates the major difference between the two methods, determination of strains, strain rate and forces. Same material model and equations of state are applicable for both methods. Therefore, it is possible to combine the two methods with appropriate conditions imposed at the interface.

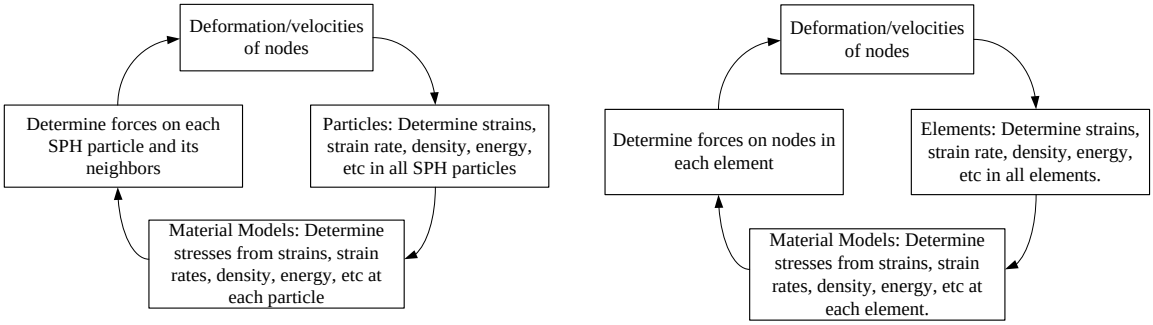

Figure 2.3 Lagrangian code structures for SPH particles and FEM elements.

Figure 2.4 describes link between the finite elements and SPH particles. The interface between elements and particles ensures continuous bonding of the two methods. At the interface, the SPH particles are constrained and moved with the elements. A node to surface contact option is used to link the SPH particles and finite element surfaces where, the SPH particles are considered as slave nodes and the side of the finite element surface is treated as the master surface. Possible penetration of the slave nodes are continuously monitored throughout the calculation procedure with slave nodes displacements. Upon detecting reasonable penetration, a contact constraint is applied to push back the slave nodes towards the master surface (Attaway et al., 1994). The influence sub-domain of the particles at/near the interface

zone such as the particle p_1, covers both the FE and SPH particles, and hence certain considerations are required in the computation. For strain and strain rate calculation of each particle (p_1), only the SPH particles inside the influence sub-domain ($p_1,...,p_6$) are considered, whereas the contributions from both SPH particles ($p_1,...,p_6$) and interface elements (E_a and E_b) inside the influence sub-domain are used to calculate the forces (Johnson, 1994). Finite element nodes ($n_1,...,n_6$) within the influence domain are not considered for force calculation except through the elements. Figure 2.5 demonstrates the sliding interface between the SPH particles and finite elements. This is particularly significant for penetration events where projectile is modeled using finite elements and the target consists of SPH particles. Again a node to surface contact is used where, the SPH particles are considered as slave nodes and the side of the finite element surface is treated as the master surface.

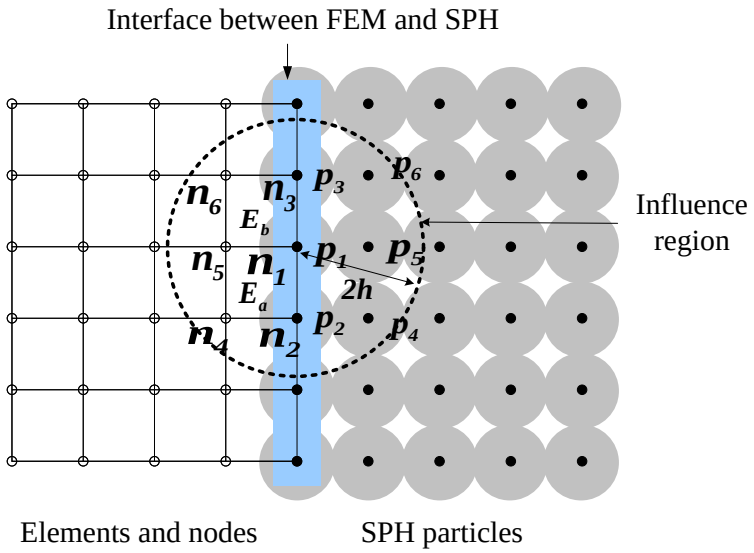

Figure 2.4 SFM: linking between the finite elements and SPH particles.

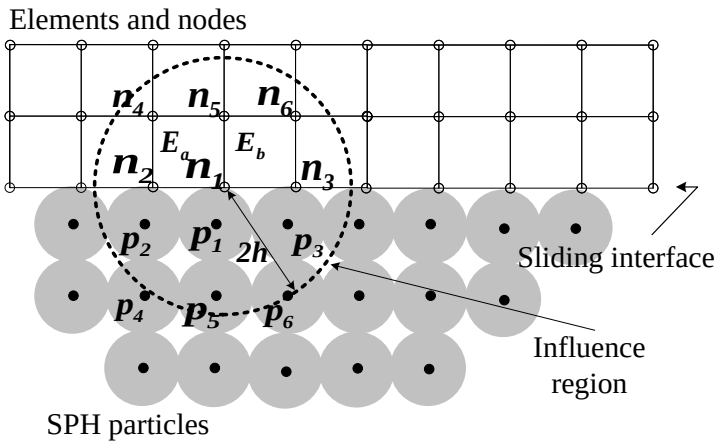

Figure 2.5 SFM: sliding contact between the finite elements and SPH particles.

2.3 Numerical Simulation

LS-DYNA is a general purpose FE software used for solving static and dynamic structural response with large deformation. The program allows the use of either finite element or meshfree methods (both SPH and EFG) individually or in combination. It contains about two hundred constitutive material models and ten equations of states (EOS) to allow the application of a wide range of materials. User defined material models can also be adopted in LS-DYNA that are chosen for numerical simulations conducted in this study. A detailed explanation can be found in Hallquist (2006).

2.3.1 Material Models

Development of material models for metals was the primary choice among the researchers in the past. However, recent interest in concrete, geological and porous materials motivates researchers to work on crushable material models. Constitutive relation in a material model relates the flow variables with the internal energy (Hallquist, 1998). Material stress tensor is divided into hydrostatic pressure and deviatoric stress tensor where hydrostatic pressure defines change in material volume under deformation. The complexity level of a constitutive material model depends on the application and the required degree of precision to describe the material behavior.

The constitutive material model for high velocity impact problem generally uses von Mises yield criteria with strain rate, thermal softening and strain hardening effects. Furthermore, equation of state (EOS) is used to consider the hydrostatic pressure component. Mie-Gruneisen EOS is normally used for impact velocity less than the sonic velocity,.

Several material models are available for metals. Among these models, both Johnson-Cook (Johnson and Cook, 1983, 1985) and Zerilli-Armstrong (Zerilli and Armstrong, 1990; Zerilli and Armstrong, 1997) models are widely used for high velocity impact problems. Both models incorporate high strain rates, large strains and thermal softening effects which are expected in high velocity impact cases. The Johnson-Cook (JC) material model is an empirical model, whereas, the Zerilli-Armstrong (ZA) material model is developed from the dislocation theory. However, the ZA constitutive relation is much more complex than the JC and material constants are much more difficult to obtain. Therefore, for simplicity and practical reasons, the JC model is used for this study.

There are several material models are available for concrete subjected to dynamic loading conditions such as, soil and foam, pseudo tensor, isotropic elastic plastic with oriented crack, geological cap, concrete damage, Holmquist-Johnson-Cook (HJC), concrete EC2 and concrete beam models (Hallquist, 2006). Among these models, the HJC model is an appropriate choice for the projectile impact study since it includes strain rate effect, high pressure and strain, damage and permanent crushing behavior of material which are a common occurrence for such study.

2.3.1.1 Johnson-Cook (JC) Model

The Johnson-Cook (JC) model considers the effect of extremely large strain, high strain rate, high temperature and severe damage in metals. It is proposed by

Johnson and Cook (1983, 1985). The JC material model, damage parameter and fracture strain are expressed respectively as,

$$\sigma = \left[A + B\left(\varepsilon_p\right)^a \right]\left[1 + C\ln\left(\dot{\varepsilon}_p/\dot{\varepsilon}_0\right)\right]\left[1 - \left(\left(T - T_r\right)/\left(T_m - T_r\right)\right)^b \right] \tag{2.41}$$

$$D = \sum_{t=0}^{t_{cur}} \frac{\Delta\varepsilon_p}{\varepsilon^f} \tag{2.42}$$

$$\varepsilon^f = \left(D_1 + D_2 \exp D_3\left(\sigma_{ave}/\sigma_e\right)\right)\left(1 + D_4 \ln\left(\dot{\varepsilon}_p/\dot{\varepsilon}_0\right)\right)\left(1 + D_5\left(\left(T - T_r\right)/\left(T_m - T_r\right)\right)\right) \tag{2.43}$$

where, ε_p is the equivalent plastic strain, $\dot{\varepsilon}_0$ (= 1 s^{-1}) and $\dot{\varepsilon}_p$ are the reference and plastic strain rates respectively, ($\dot{}$) implies differentiation with respect to time, T_m and T_r are the melting and room temperatures respectively, t_{cur} is the time at the current step, σ_{ave} and σ_e are the average normal stresses and von-Mises stress respectively, *A, B, a, C* and *b* are the material constants. The three brackets in Eq. (2.41) take into account the effects of plastic strains, the strain rates and the temperature respectively. Fracture in material occurs by element erosion when *D* reaches unity. D_1 to D_5 in Eq. (2.43) are the five damage parameters.

2.3.1.2 Elastic/Plastic Material Model

The elastic/plastic material model with isotropic/kinematic hardening is a cost effective simple material model which is adopted in LS-DYNA. This method is developed by Krieg and Key (1976). Isotropic, kinematic or combination of both hardening can be included into the model by varying parameter ψ between 0 and 1.

The current radius of yield surface, σ_y is defined as,

$$\sigma_y = \sigma_0 + \psi E_p \varepsilon_{eff}^p \tag{2.44}$$

where, ε_{eff}^p is the effective plastic strain, $E_p\left(= E_t E/\left(E - E_t\right)\right)$ is the plastic hardening modulus and E_t is the tangent modulus. Strain rate effect can be included

into the model by including Cowper-Symonds (Jones, 1983) model as scale factor into the formulation of yield stress as,

$$\sigma_y = \left[1 + \left(\dot{\varepsilon}/\mathfrak{R}\right)^{\left(1/\wp\right)}\right]\left(\sigma_0 + \psi E_p \varepsilon_{eff}^{p}\right) \tag{2.45}$$

where, $\mathfrak{R}$ and $\wp$ are user defined constants.

2.3.1.3 Holmquist-Johnson-Cook (HJC) Model

When concrete is subjected to high velocity impact it undergoes high pressures, large strains, high strain rates and damage. Therefore, it is necessary to use a material model which includes these effects in constitutive conditions. The Holmquist-Johnson-Cook (HJC) material model for concrete was developed by Holmquist et al. (1993). It is an elastic-plastic damage model which considers high strain, strain rate effect and damage.

In the HJC (Holmquist et al., 1993) model, the normalized equivalent stress is defined as,

$$\sigma_{eq}^{*} = \frac{\sigma_{eq}}{f_c'} = \left[\mathcal{A}\left(1-D\right) + \mathcal{B}P^{*\mathcal{N}}\right]\left[1 + C\ln\left(\frac{\dot{\varepsilon}}{\dot{\varepsilon}_0}\right)\right] \le \sigma_{\max}^{*} \tag{2.46}$$

where, σ_{eq} is the equivalent stress, f_c' is the unconfined compressive strength of concrete, $P^{*} = P/f_c'$ is the normalized pressure, P is the current pressure, $\dot{\varepsilon}$ and $\dot{\varepsilon}_0$ are the current and reference strain rates. In Eq. (2.46), normalized cohesive strength parameter $\mathcal{A}$, normalized pressure hardening coefficient $\mathcal{B}$, strain rate coefficient C, pressure hardening exponent $\mathcal{N}$, and normalized maximum strength $\sigma_{\max}^{*}$ are all material constants. Material damage has also been incorporated using a damage variable D. Stress-pressure relationship of the material model is presented in Figure 2.6.

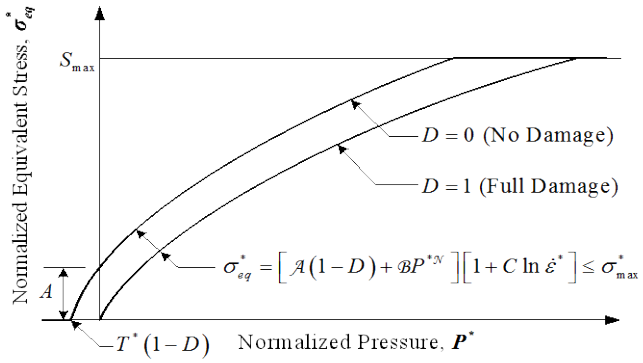

Figure 2.6 Normalized stress-pressure response of the HJC concrete model.

The HJC model uses a strain based damage model, where damage D ($0 \le D \le 1$) is calculated from both the incremental equivalent plastic strain ($\Delta\varepsilon_p$) and incremental equivalent plastic volumetric strain ($\Delta\mu_p$) and expressed as,

$$D = \sum \frac{\Delta\varepsilon_p + \Delta\mu_p}{\varepsilon_p^f + \mu_p^f} \tag{2.47}$$

where, the plastic strain to fracture $\varepsilon_p^f + \mu_p^f$ can be defined as,

$$\varepsilon_p^f + \mu_p^f = D_l\left(P^* + \overline{f}_t'\right)^{D_m} \ge \varepsilon_{\min}^f \tag{2.48}$$

D_l and D_m are the damage constants and $\overline{f}' = f_t'/f_c'$ is the normalized maximum tensile strength. The plastic strain to fracture value is limited by an additional damage constant $\varepsilon_{\min}^f$ in order to limit the plastic strain for material fracture. Damage response of the material model is plotted in Figure 2.7(a).

The pressure-volume behavior of the HJC concrete model can be expressed in three regions (Figure 2.7(b)). The linear elastic part is limited by the pressure and volumetric strain values of P_{crush} and μ_{crush}, respectively. In between the elastic and total damaged concrete, the material undergoes damage with the presence of plastic volumetric strain. The region ranges from the pressure values P_{crush} to P_{lock}. At the end of this region, it is assumed that the material is totally damaged and compacted with

no tensile strength. The third region defines the fully dense material without any air voids and the pressure-volume responses at this region is expressed as,

$$P = K_1\bar{\mu} + K_2\bar{\mu}^2 + K_3\bar{\mu}^3 \tag{2.49}$$

where, K_1, K_2 and K_3 are the material constants, $\bar{\mu} = \left(\mu - \mu_{lock}\right)/\left(1+\mu_{lock}\right)$ is the modified volumetric strain, $\mu = \rho/\rho_0 - 1$ is the standard volumetric strain, ρ is the current density, ρ_0 is the initial density, and $\mu_{lock} = \rho_{grain}/\rho_0 - 1$ is the locking volumetric strain and ρ_{grain} is the grain density.

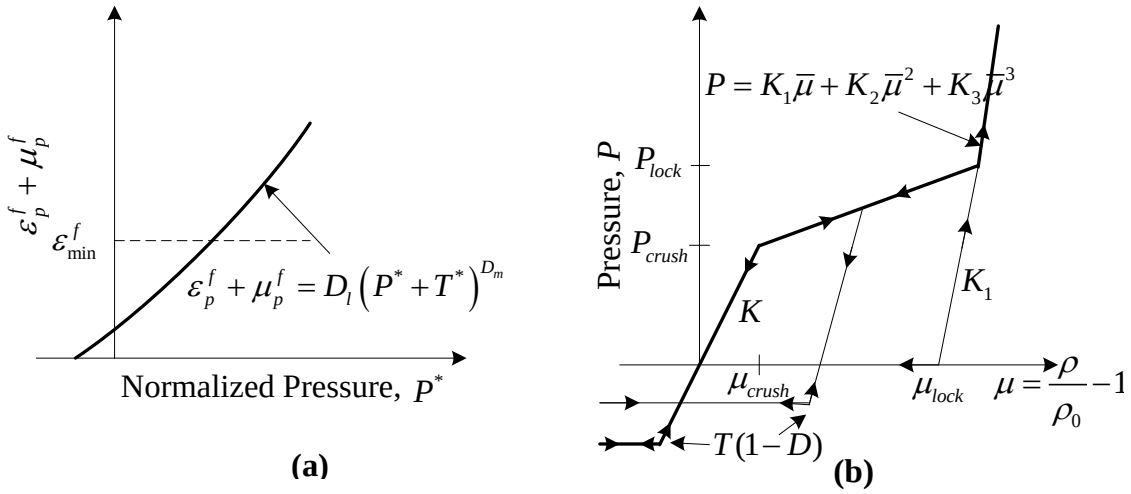

Figure 2.7 Damage and pressure-volume responses of the HJC concrete model.

2.3.2 Equation of State (EOS)

The volumetric response (hydrostatic pressure term) of material is often defined by an equation of state (EOS) which relates pressure, volume and thermal properties like internal energy or temperature. Depending on the pressure, the pressure and volumetric strain relationship can be either linear or non-linear for small and high pressure respectively. An artificial viscosity parameter is also used to allow the discontinuous shock wave propagation.

It is difficult to evaluate the requirement and significance of EOS in projectile impact events. However, a simple categorization can be achieved based on the

projectile striking velocity. For instance, in the sub-ordnance velocity regime, pressure is comparatively small and material strength components are dominating. Therefore, only a linear EOS is enough. For ordnance and ultra-ordnance velocity regime, where pressure effect is much higher, the effect of EOS becomes more significant.

In this study, Gruneisen EOS is used for metals with the JC material model and it can be described as (Hallquist, 2006),

$$\mathrm{P}=\frac{\rho_0 C_k^2 \mu\left[1+\left(1-\frac{\gamma_0}{2}\right)\mu-\frac{\overline{a}}{2}\mu^2\right]}{1-\left(s_1-1\right)\mu-s_2\frac{\mu^2}{\mu+1}-s_3\frac{\mu^3}{\left(\mu+1\right)^2}}+\left(\gamma_0+\alpha\mu\right)I \tag{2.50}$$

where, C_k is the intercept of shock wave velocity (u_s) versus particle velocity (u_p) curve, s_1, s_2 and s_3 are the coefficients from u_s-u_p curve, γ_0 is the Gruneisen constant, $\overline{a}$ is the first order volume correction to γ_0, and I is the internal energy per initial volume.

2.3.3 Element Erosion

Element erosion technique is implemented to eliminate the highly distorted elements which exist in front of and around the projectile nose during penetration/perforation of the projectile. This method is also known as the ‘eroding slidelines’ in the literature (Camacho and Ortiz, 1997; Zukas, 1990) where redefinition of the master-slave interfaces occurs with highly distorted element erosion. It should be noted that the element erosion is a numerical consideration and not the material failure. In this method, the elimination process is performed by the use of element removal criteria usually related to pressure, stress or strain of elements. When the conditions satisfy the erosion criteria, element stress states become void/zero and the element removed from subsequent analysis. Although this method

provides a successful solution to severe mesh distortion problem, it also suffers from shortcomings like loss of mass and energy due to element erosion. Therefore, this method may not provide sufficiently accurate results for situations where large numbers of elements are deleted.

Element erosion approach can be either applied with the material constitutive model or as a separate option. Since most of the constitutive models do not contain erosion, a separate option where erosion criteria can be set independently is the preferred alternative. Some of the most familiar failure criteria for element erosion are shown as follows,

$$P \geq P_{\max} \tag{2.51}$$

$$P \leq P_{\min} \tag{2.52}$$

$$\sigma_1 \geq \sigma_{\max} \tag{2.53}$$

$$\sqrt{\frac{3}{2} S_{ij} S_{ij}} \geq \sigma_{eq}^{f} \tag{2.54}$$

$$\varepsilon \geq \varepsilon_{\max} \tag{2.55}$$

$$\varepsilon \leq \varepsilon_{\min} \tag{2.56}$$

$$D \leq D_c \tag{2.57}$$

Eqs. (2.51) and (2.52) are pressure erosion criteria. In which, P is the pressure; $P_{\max}$ and $P_{\min}$ are the maximum and minimum pressures at failure. For stress erosion criteria, the failure stress can be either the maximum principal stress or the equivalent stress as shown in Eqs. (2.53) and (2.54); where, σ_1 is the maximum principal stress, $\sigma_{\max}$ is the maximum principal stress at failure, S_{ij} is the deviatoric stress and σ_{eq}^{f} is the equivalent stress at failure. Eqs. (2.55) and (2.56) give the strain (ε) erosion criteria where, $\varepsilon_{\max}$ and $\varepsilon_{\min}$ are the maximum and minimum principal strains at

failure. Damage (D) can be also used as erosion criteria as shown in Eqs. (2.57), where D_c is the critical damage. Among all these criteria, strain based element erosion criteria is the most popular.

2.3.4 Contact Algorithm

Contact definition of colliding bodies at the interfaces has always been important consideration. From the literature review, it can be stated that the penalty method with explicit time integration method is well suited for finite element simulations of high velocity impact problems, and hence, it is adopted in the present study. For colliding bodies, one of the interfaces is considered as the master interface and other is regarded as the slave interface. Nodes in these interfaces are termed as master and slave nodes, respectively.

2.4 Conclusions

Various numerical methods for high velocity impact simulations are reviewed in this chapter. It is observed that both Lagrangian finite element method with certain remedial measures against severe element distortion and coupled SPH-FEM (SFM) have the potential for a robust and efficient numerical tool for high velocity impact simulations depending on various conditions. SFM has one disadvantage over Lagrangian FEM. It requires more computational resources which makes it difficult to use in large domain size problems. Therefore, in the present study, perforation and penetration studies of metal plates with relatively smaller thickness are performed using the SFM and perforation and penetration of concrete slabs with thicker thickness are simulated using Lagrangian FE formulations with element erosion. For simulation purpose a FE platform LS-DYNA has been chosen. LS-DYNA has varieties of material models to choose from, for both metals and concrete materials. Two material models for metals (Johnson-Cook and elastic/plastic models) and one material model for concrete (Holmquist-Johnson-Cook model) have been discussed

briefly and will be used in the impact simulations. LS-DYNA supports user defined material models which allow application of new material models.

Chapter 3 Material Constitutive Equations

3.1 Introduction

To be able to simulate the complex phenomenon involving high velocity projectile impact on a target, it is essential to have a robust material model which includes the stress state, strain rate, temperature and damage. However, a balance between a complex model requiring a large numbers of material constants and extensive test data to determine these parameters should be sought and the simplest model yet able to describe reasonably accurately the essential material behavior required in the analysis is established.

For a long time, collision between bodies has been studied analytically in order to understand the structural response under impact loading. In such problems, major concerns are the effects of loading rate, temperature and damage. Indeed, employing these in the material model is a great challenge. Although a significant improvement has been achieved on large scale finite element software packages in various engineering applications, lack of a robust and efficient material models is one of the prime factors in restraining numerical structural analysis in handling this class of problems.

The subject matter in this chapter is divided into two major sections. Firstly, a modified version of the Johnson-Cook (JC) model is proposed along with the procedure for determining the material parameters of the new model. Secondly, a concrete material model is developed and material constant obtaining procedure is discussed.

3.2 Constitutive Models

3.2.1 Modified Johnson-Cook (MJC) Model for Metals

Low strain rate is often considered as the isothermal process and high strain rate as the adiabatic process. Figure 3.1(a) demonstrates a stress-strain curve for metal where work hardening rate is observed under isothermal conditions. Because work done in plastic flow is converted to heat, in an adiabatic condition material temperature will increase, and gradually reduces the work hardening rate leading to material softening shown as the dashed line in Figure 3.1(a). Not all the generated heat remains within the specimen. A small portion of it is lost due to radiation and heat conduction. Since adiabatic shear failure is prominent to high velocity impact problems for metals it is necessary to include temperature effect due to adiabatic condition.

The temperature increment due to adiabatic condition can be derived using the following equation (Khan and Liang, 1999),

$$\Delta T = \frac{\beta}{\rho C_p} \int \sigma\left(\varepsilon_p\right) d\varepsilon_p \tag{3.1}$$

where, C_p is the specific heat, ρ is the density of the material and ε_p is the equivalent plastic strain. The value of β describes the percentage of heat remains within the material and varies from 0 (isothermal) to 1 (adiabatic). Mason et al. (1994) measured β value for 2024 aluminum, 4340 steel and Ti-6Al-4V at 3000 s^{-1}, 2500 s^{-1} and 1500 s^{-1} respectively using the infrared radiometer, and found that the β value varies between 0.5 to 0.95. Macdougall and Harding (1999) monitored the variation in β value (from 0.2 to 0.7) with increasing plastic strain from the torsion test of Ti-6Al-4V at 700 s^{-1}. Kapoor and Netmat-Nasser (1998) and Nemat-Nasser et al. (2001) conducted tests on several materials namely, Ta-2.5% W, titanium, 1018 steel, 6061-

T6 aluminum, OFHC copper, and Ti-6Al-4V at high strain rates (2000 – 3000 s^{-1}) and concluded that within test error, all the work done was converted to heat, i.e. $\beta = 1.0$. Taylor and Quinney (1934) observed β value around 0.9 from the rapid torsion and compression tests on mild steel and copper. Considering these, a rational value of $\beta = 0.9$ is proposed in the modified Johnson-Cook (MJC) model for all the metals under high velocity impact adopted herein.

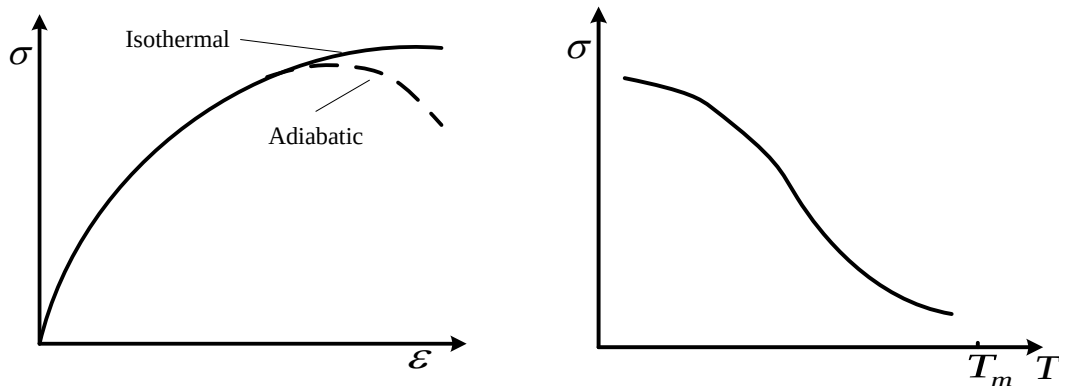

(a) (b)

Figure 3.1 (a) Isothermal stress-strain plot showing thermal softening (dashed line) due to adiabatic conditions. (b) Thermal softening rate and temperature effect on strength.

The strain rate constant, *C* in the JC model (Eq. 2.41 and Eq. 2.43) varies with the reference strain rate, $\dot{\varepsilon}_0$. The strain rate expression can also cause mathematical error for $\dot{\varepsilon}_p = 0$ (Børvik et al., 2001a). To resolve the problem, a new model namely modified Johnson-Cook (MJC) model is proposed by the author. It contains a simple but elegant strain rate effect expression without considering a reference strain rate parameters, which is a modification of the strain rate expression proposed by Farrokh and Khan (2009). The equivalent stress, damage and fracture strain of the proposed MJC model are expressed as,

$$\sigma = \left[A + B\left(\varepsilon_p\right)^a \right] \left[\dot{\varepsilon}_p \right]^C \left[1 - \left(\left(T - T_r\right) / \left(T_m - T_r\right) \right)^b \right] \tag{3.2}$$

$$D = \sum_{t=0}^{t_{cur}} \frac{\Delta \varepsilon_p}{\varepsilon^f} \tag{3.3}$$

$$\varepsilon^f = \left(D_1 + D_2 \exp D_3 \left(\sigma_{ave}/\sigma_e\right)\right)\left(\dot{\varepsilon}_p\right)^{D_4}\left(1 + D_5\left(\left(T - T_r\right)/\left(T_m - T_r\right)\right)\right) \quad (3.4)$$

3.2.2 Procedure for Obtaining MJC Material Model Parameters

Determining the material model parameters for the modified Johnson-Cook (MJC) requires careful consideration and well defined procedures. There are five material parameters required to determine the equivalent stress for the MJC model. The first three parameters (A, B and a) describe plastic deformation of the material, the fourth parameter C contributes to the strain rate effect, and the last parameter b reflects the temperature effect. Three steps are proposed by the author to obtain all the parameters for any material. Damage of metallic plates is ignored in the present study, and hence, damage parameters are not used in the present work. Because of that determination procedures for damage parameters D_1 to D_5 are not mentioned in this section.

3.2.2.1 Titanium Alloy Ti-6Al-4V

In this section, the procedure of calculating material parameters is described using the results from various tests of titanium alloy Ti-6Al-4V conducted by Khan et al. (2004), such as (1) quasi-static compression test at room temperature and strain rate of 1 s^{-1}, (2) compression tests at strain rates of 10^{-5} s^{-1}, 10^{-3} s^{-1}, 1 s^{-1} and 3378 s^{-1}, and (3) quasi-static tests at strain rate of 0.01 s^{-1} and temperatures 149˚C, 315˚C and 482˚C.

Step 1: The flow stress of the MJC model is shown in Eq. (3.2). At room temperature (for example, 25˚C) and unit strain rate, Eq. (3.2) can be expressed as,

$$\sigma = \left[A + B\left(\varepsilon_p\right)^a\right] \quad (3.5)$$

A Fortran program is used to determine the material parameter A, B and a using the least square method from the experimental stress-strain data at room

temperature and unit strain rate, which is found to be 1112.0 MPa, 1082 MPa and 0.686, respectively. Comparison of the experimental and predicted stress-strain plot is illustrated in Figure 3.2.

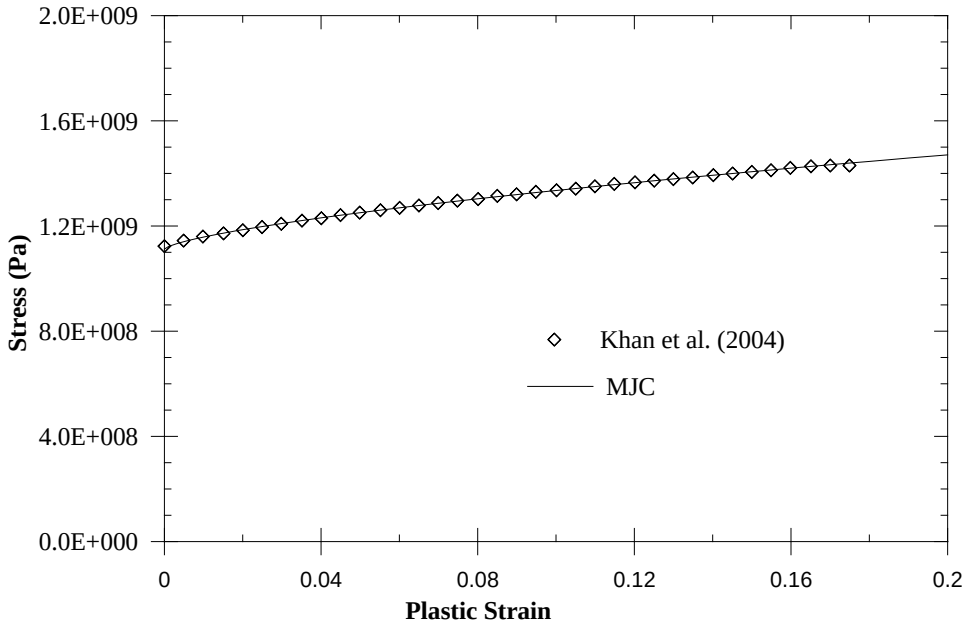

Figure 3.2 σ vs ε_p for the Ti-6Al-4V at a strain rate of 1 s^{-1}.

Step 2: The strain rate effect parameter *C* is determined from the $\sigma - \dot{\varepsilon}_p$ plot. At room temperature, Eq. (3.2) can be expressed as,

$$\sigma = \sigma_A \left[\dot{\varepsilon}_p \right]^C \tag{3.6}$$

$$\log_{10}(\sigma) = \log_{10}(\sigma_A) + C \log_{10}\left[\dot{\varepsilon}_p \right] \tag{3.7}$$

where, $\sigma_A = \left[A + B(\varepsilon_p)^a \right]$. A Fortran program with the least square method is applied to determine the strain rate parameter *C*. Figure 3.3 shows the calculated *C* values at various plastic strains that reach the approximate uniform value of 0.0133 at plastic strain of about 0.06 and greater. Because of the uncertainties of the strains values at low strain levels for high strain rates, *C* values at low strains are not considered while calculating *C* value.

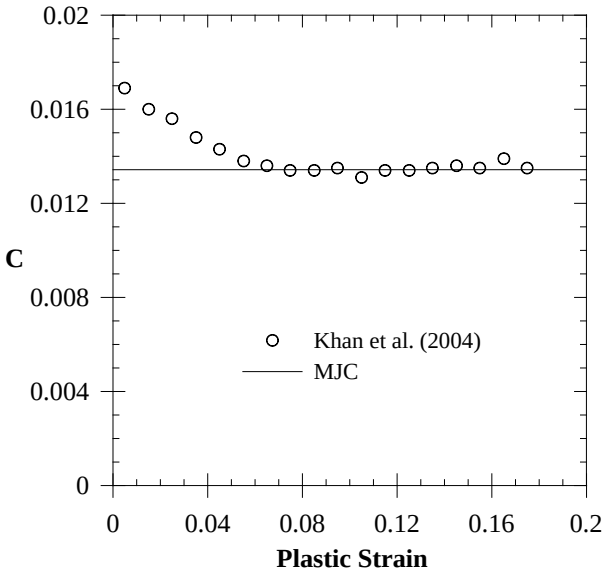

Figure 3.3 Variation of C value for the Ti-6Al-4V at various plastic strains.

Step 3: The temperature effect parameter b is obtained using the $\sigma - T$ plot. For the same set of materials at similar ranges of strain rate value, Eq. (3.2) can be written as,

$$\sigma = \sigma_B \left[1 - \overline{T}^b\right] \tag{3.8}$$

$$\log_{10}\left(1 - \frac{\sigma}{\sigma_B}\right) = b \log_{10}\left(\overline{T}\right) \tag{3.9}$$

$$b = \log_{10}\left(1 - \frac{\sigma}{\sigma_B}\right) \Big/ \log_{10}\left(\overline{T}\right) \tag{3.10}$$

where, $\sigma_B = \left[A + B\left(\varepsilon_p\right)^a\right]\left[\dot{\varepsilon}_p\right]^C$ which can be calculated for various plastic strains using the previously determined parameters, and $\overline{T} = \left(T - T_r\right)/\left(T_m - T_r\right)$ is the homogenous temperature. Figure 3.4 illustrates the variation of parameter b for strain ranging from 0.01 to 0.18, at temperatures 149°C, 315°C and 482°C and strain rate of 0.01 s^{-1}. Isothermal condition is assumed at this low strain rate. As shown in Figure 3.4, b reaches a constant value of about 0.8 when the plastic strain exceeds about 0.04. Ti-6Al-4V alloy has two phases namely, alpha and beta phases and it transforms from alpha phase to beta phase at temperature of 996°C (beta transus temperature).

The effects of temperature on material properties change abruptly at the phase transition. The proposed MJC model material parameters are thus applicable only for Ti-6Al-4V at or below beta transus temperature.

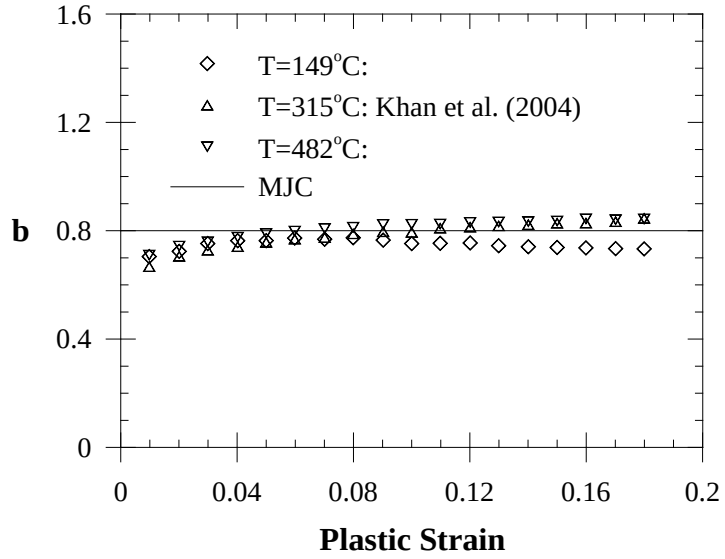

Figure 3.4 Variation of b value for the Ti-6Al-4V at various strains.

Values of the five parameters for Ti-6Al-4V are summarized in Table 3.1 along with other material properties. Experimental stress-strain plots at various strain rates and temperatures (Khan et al., 2004) are compared with the MJC predicted data in Figure 3.5, and indeed, they show reasonably good agreement. The material parameters are validated against two other different material test data of commercial Ti-6Al-4V conducted by Nemat-Nasser et al. (2001) and Seo et al. (2005). Figure 3.6 and 3.7 demonstrate the experimental and predicted stress-strain plots. The MJC model exhibits a good correlation with most experimental results.

Table 3.1 Ti-6Al-4V material parameters for MJC model

ρ_0 (kg/m^3)	E (GPa)	ν	G (GPa)	A (MPa)	B (MPa)
4450	110	0.33	42.5	1112	1082
A	C	b	C_p (J/kgK)	T_m (˚K)	T_r (˚K)
0.686	0.0133	0.80	560	1877	298

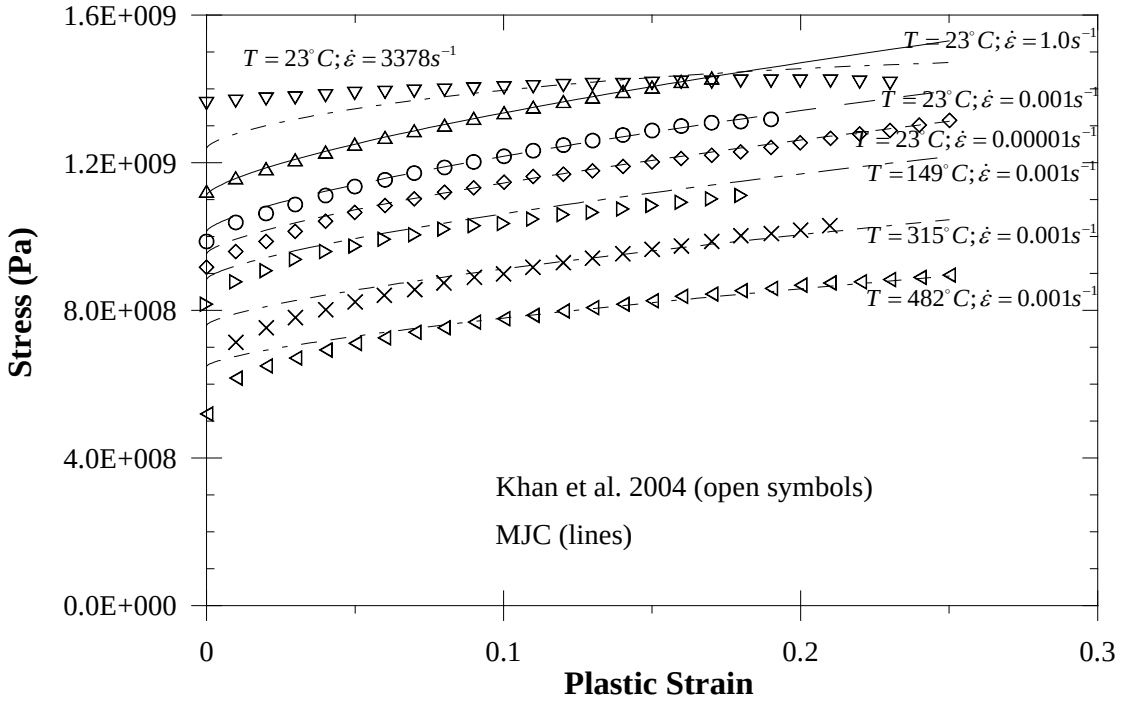

Figure 3.5 Comparison of the MJC model with the experimental data for the Ti-6Al-4V.

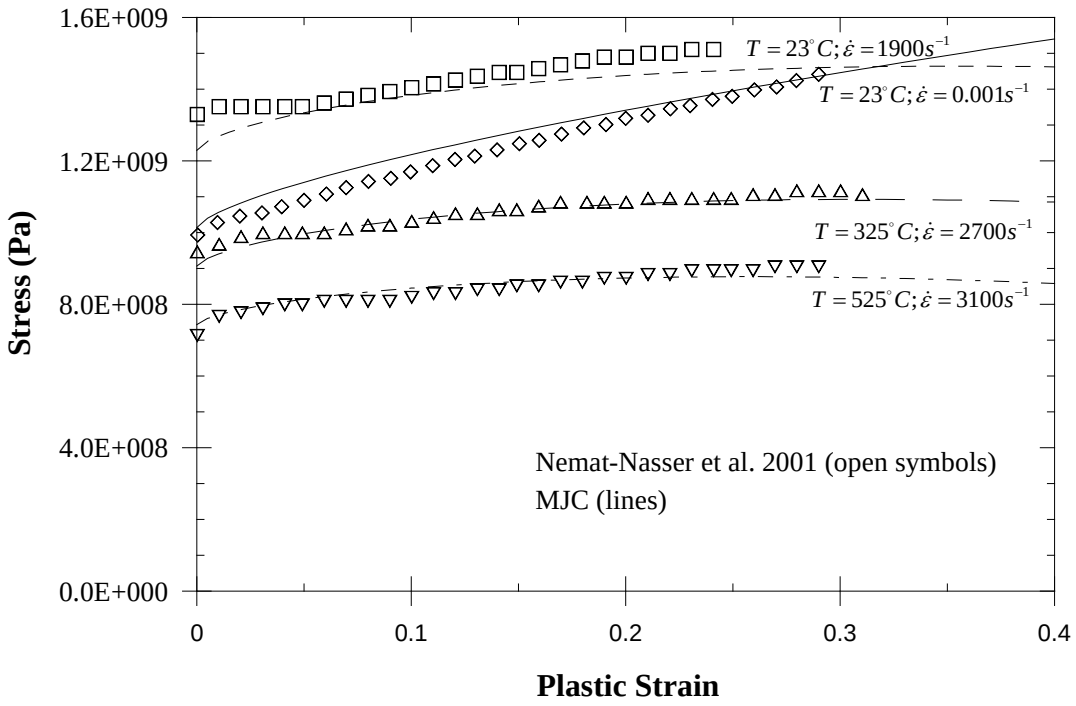

Figure 3.6 Comparison of the MJC model and the test data for the Ti-6Al-4V.

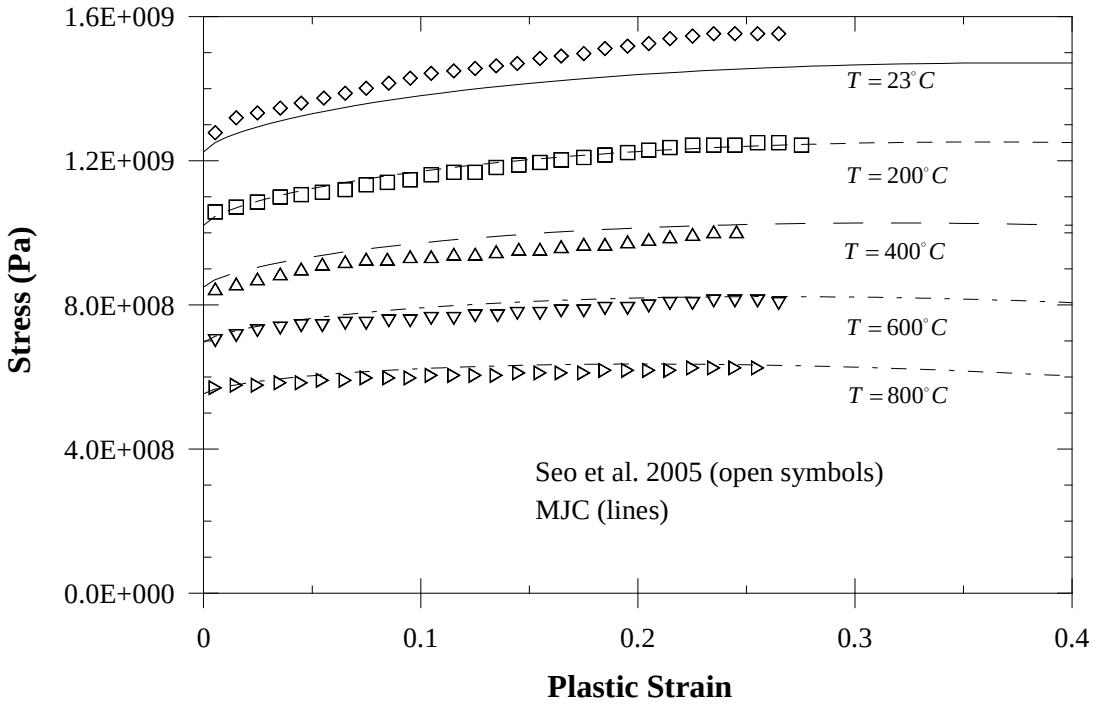

Figure 3.7 Comparison of the MJC model and the experimental results at strain rate of 1400 s^{-1} for the Ti-6Al-4V.

3.2.2.2 Weldox 460 E Steel

This section describes identification procedure of the MJC model parameters for Weldox 460 E steel plate. All the parameters are calculated from the tests performed by Børvik, et al. (2001a). The strength parameters (*A*, *B* and *a*) are determined first from the quasi-static tensile test of smooth specimen at room temperature through least square method. Figure 3.8(a) demonstrates the comparison of the test and MJC model stress versus plastic strain plot. Secondly, the strain rate parameter, *C* is established from the stress-strain plots at room temperature and various strain rates, such as 0.00074, 2.16 and 1522 s^{-1}. By adopting the least square method *C* value is evaluated for each plastic strain. As illustrated in Figure 3.8(b), *C* shows a steady value of about 0.01 when the plastic strain is larger than 0.05. Third step is to determine the temperature effect parameter, *b* from the stress-strain curves at high temperatures. In general for steel, thermal softening occurs at high temperatures. However, Børvik, et al. (2001a) observed a certain increase in tensile strength at

temperatures between 200 – 400°C due to blue brittle phenomenon. In blue brittle region, the ductility of carbon steel is decreased, but the strength is increased with increase in temperature. Since the MJC model is not sensitive to this behavior, only stress-strain curves at 100°C and 500°C temperatures are considered for calculation of *b* value. Figure 3.8(c) shows *b* versus plastic strain plots. As the *b* value is considered constant in this work, an average value of 0.94 is calculated for plastic strains varying between 0.03 – 0.15. All the material properties for MJC model of Weldox 460 E steel are summarized in Table 3.2. A comparison of the MJC and JC computational data with the test results for strain rates of 0.0015 s^{-1}, 4.44 s^{-1}, 21.6 s^{-1} and 577 s^{-1} are given in Figure 3.9. The agreement between the test and MJC model data are reasonably good compare to the JC model data except at high level of plastic strain (greater than 0.20). Both the JC and MJC models are incapable of handling material softening at high plastic strain, and thus, the agreement is not good beyond plastic strain of 0.2. However, for the high velocity impact problems within the ordnance range, maximum plastic strain value of 0.2 is observed for the most cases. Therefore, material properties obtained herein is reasonable for the present study.

Table 3.2 MJC Material properties for Weldox 460 E steel

ρ_0 (kg/m^3)	*E* (GPa)	*v*	*G* (GPa)	*A* (MPa)	*B* (MPa)
7850	200	0.33	75.2	503	581
a	*C*	*b*	C_p (J/kgK)	T_m (K)	T_r (K)
0.481	0.01	0.94	452	1800	293

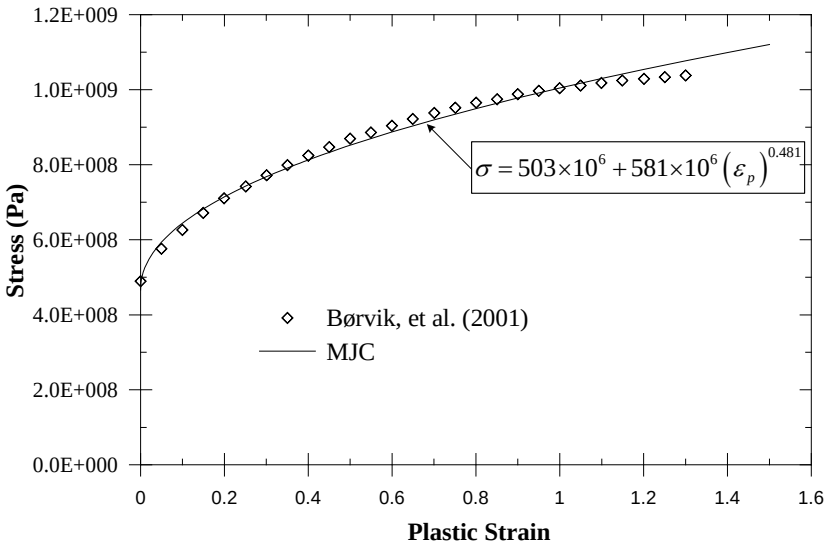

(a)

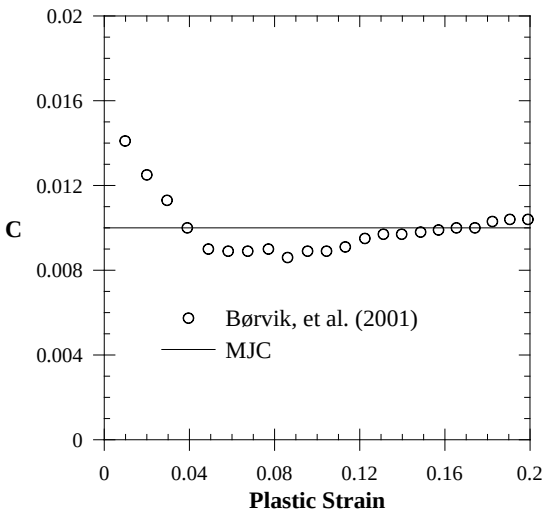

(b)

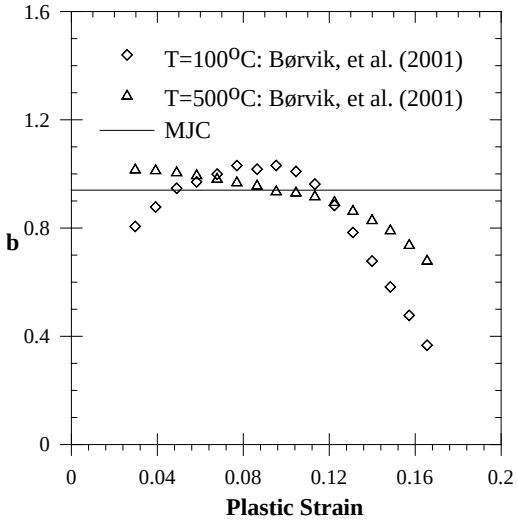

(c)

Figure 3.8 MJC material properties for Weldox 460 E steel.

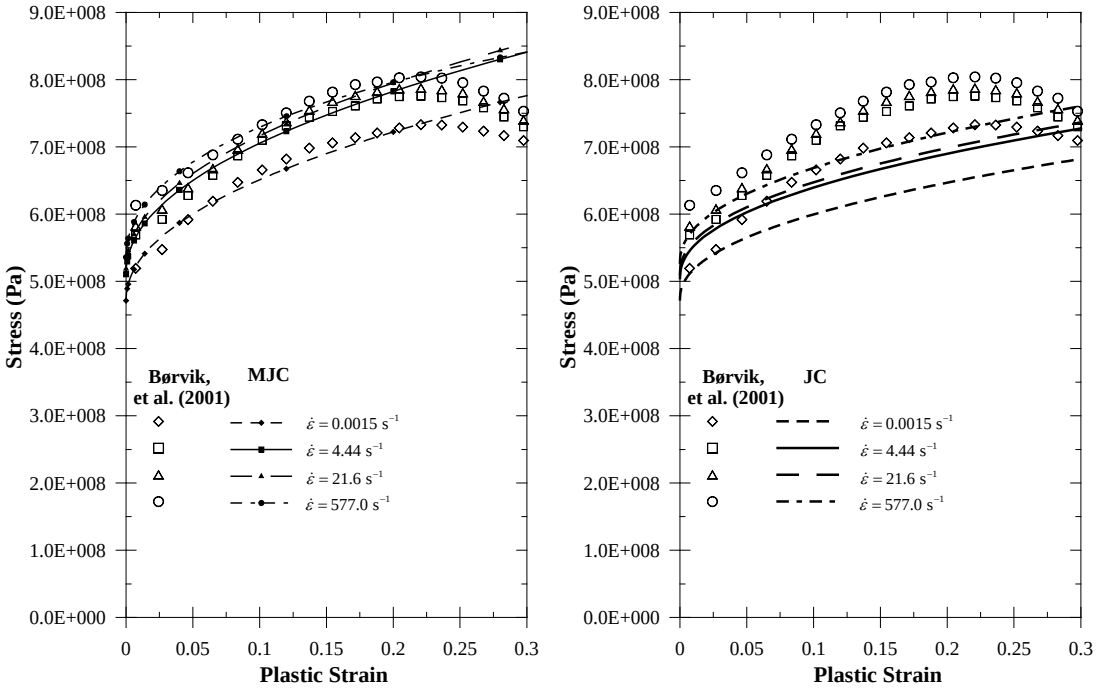

Figure 3.9 Comparison of the experimental and (a) MJC, and (b) JC model prediction at various strain rates.

3.2.3 Modified Holmquist-Johnson-Cook (MHJC) Model for Concrete

Defining the material model for heterogeneous concrete is difficult and complex, and normally is considered homogeneous for simplification. Several macro-scale concrete models for dynamic loading cases are available. They consider extreme pressure, strain hardening, strain rate and damage (Gebbeken and Ruppert, 2000; Holmquist et al., 1993; Malvar et al., 1997; Polanco-Loria et al., 2008; Riedel et al., 1999). Some of these models are sophisticated and require a good number of material parameters. The determination of these material parameters is substantially involved and demanding. Among these models, the Holmquist-Johnson-Cook (HJC) model is widely used for high velocity impact problems because of its smaller number of material constants requirements. However, single strain rate expression in the HJC is inadequate since concrete exhibits two distinct behaviors above and below a critical strain rate. Furthermore, pressure-volume description of the HJC model involves a large number of material constants (Section 2.3.1.3) and needs a triaxial test data to

identify the material constants which is very hard to achieve. Therefore, the modified Holmquist-Johnson-Cook (MHJC) model is proposed with an improved and simplified strain rate and pressure-volume expressions. As concrete properties are less affected by temperature effect, it is not included in the MHJC model. The constitutive equations of the MHJC model are discussed herein.

3.2.3.1 Yield Surface

Yield surface of the proposed MHJC model is described as,

$$f\left(I_1, J_2, \dot{\varepsilon}\right) = \sigma_{eq} - \sigma_C F_{DIF} \tag{3.11}$$

where, $I_1 = \sigma_{ii}$ is the first invariant of the stress tensor, $J_2 = \frac{1}{2} S_{ij} S_{ij}$ is the second invariant of the deviatoric stress tensor, $\dot{\varepsilon}$ is the strain rate and F_{DIF} is the dynamic strength increase factor. In Eq. (3.11), $f < 0$ indicates elastic stress state and $f = 0$ specify stress state on failure surface. Normalized stress state $\sigma_C^* = \sigma_C / f_c'$ is described by the curved meridian of the triaxial compression (Holmquist et al., 1993) and expressed as

$$\sigma_C^* = \frac{\sigma_C}{f_c'} = \left[\mathcal{A}\left(1 - D\right) + \mathcal{B}\left(P^*\right)^{\mathcal{N}} \right] \tag{3.12}$$

$\mathcal{A}$, $\mathcal{B}$ and $\mathcal{N}$ are the material constants, D is the damage and $P^* = P / f_c'$ is the normalized pressure. Figure 3.10 demonstrates the upper (undamaged) and lower (damaged) bounds of the normalized stress-pressure curves.

3.2.3.2 Strain Rate Effect

Like most materials, concrete exhibits considerable sensitivity to strain rate. Reasons behind such behavior are the limiting crack velocities (Tedesco et al., 1997) and the viscoelastic characteristics of the cement paste (Li and Meng, 2003). Figure 3.11 depicts the collaboration of various test results showing the strain rate sensitivity

of the concrete for compression and tension in terms of dynamic increase factor (F_{DIF}), which is the ratio of the dynamic compressive or tensile strength to the static compressive or tensile strength. Therefore, it is necessary to consider the strain rate effect into the constitutive equation of concrete.

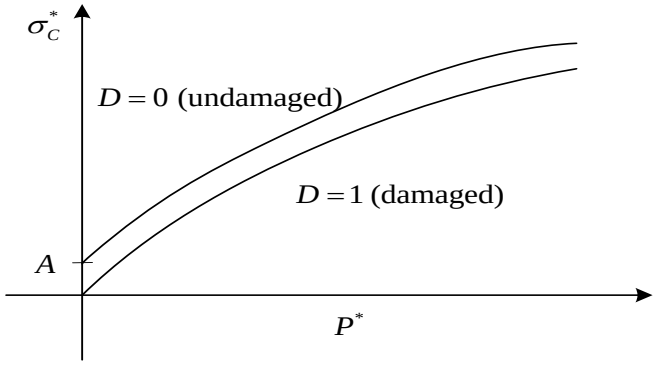

Figure 3.10 Normalized stress-pressure relationships for the MHJC model.

At high strain rates, change in concrete strength is different from that at the low to moderate strain rates. Kipp et al. (1980) proposed a strain rate dependent critical crack stress for rocks using linear elastic dynamic fracture mechanics. Dynamic stress intensity factor (K_I) decreases almost linearly from the static stress intensity factor with the increasing crack velocity (Freund, 1972). This implies that a dynamic crack causes less stress intensity than the static crack at the same displacement. If fracture in material is defined by the expression $K_I = K_{IC}$ (where, K_{IC} is the critical stress intensity factor), it can be concluded that the loading capacity of the material is comparatively superior at high crack velocity.

Kipp et al. (1980) developed a relationship between the stress intensity factor and constant stress rate $\dot{\sigma}_0$ for a penny shaped crack,

$$K_I(t) = \chi \frac{4}{3\sqrt{\pi}} \sqrt{c_s} \dot{\sigma}_0 t^{3/2} \tag{3.13}$$

where, χ is the geometric constant (1.12 for penny shaped crack), c_s is the shear wave velocity and t is the loading time.

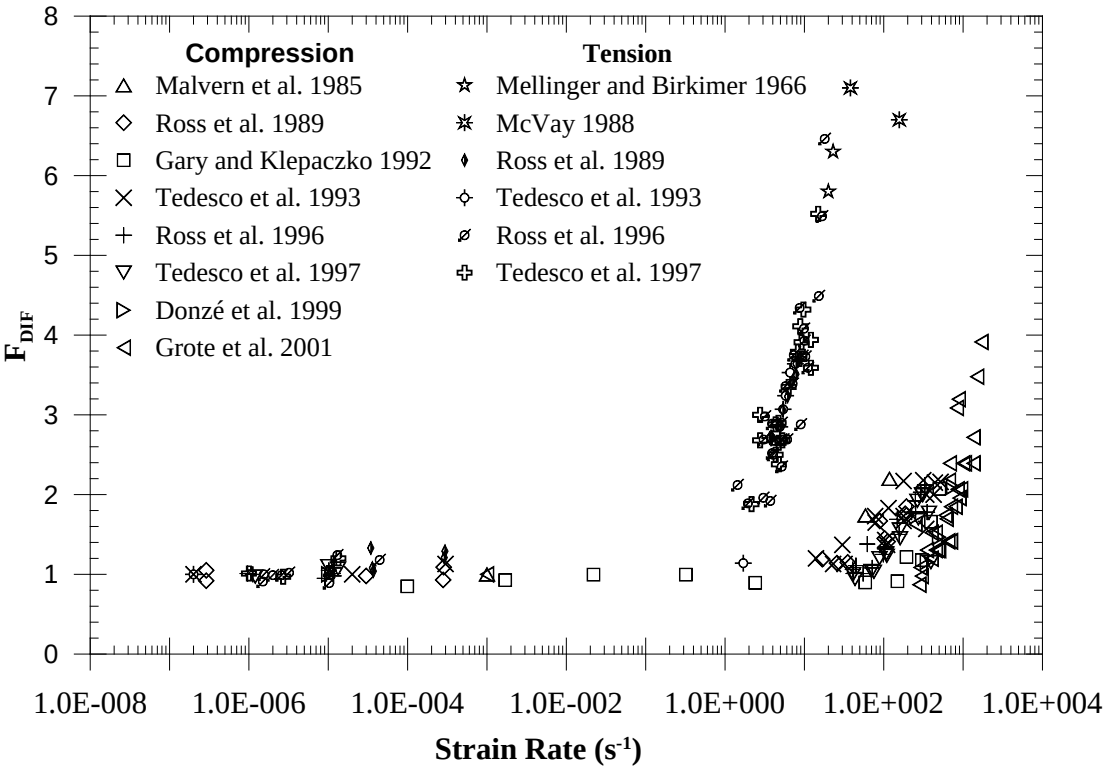

Figure 3.11 Strain rate effect on compressive and tensile strength of concrete.

Based on Eq. (3.13), the critical stress intensity factor can be expressed as

$$K_{IC} = \chi \frac{4}{3\sqrt{\pi}} \frac{\sqrt{c_s}}{\sqrt{\dot{\sigma}_0}} \sigma_C^{3/2} \tag{3.14}$$

where, σ_C is the critical stress.

For the material fracture ($K_I = K_{IC}$), the fracture or critical stress can be written in terms of strain rate $\dot{\varepsilon}_0$

$$\sigma_C = O\dot{\sigma}_0^{1/3} \tag{3.15}$$

$$\sigma_C = Q\dot{\varepsilon}_0^{1/3} \tag{3.16}$$

where,

$$O = \left(\frac{9\pi K_{IC}^2}{16\chi^2 c_s} \right)^{1/3} \tag{3.17}$$

$$Q = \left(\frac{9\pi E K_{IC}^2}{16\chi^2 c_s} \right)^{1/3} \tag{3.18}$$

From Eq. 3.16, it is evident that the critical stress is proportional to the cubic root of the strain rate. Based on this cubic root law, the dynamic strength increase factor is written as,

$$F_{DIF} = C_2 \left(\frac{\dot{\varepsilon}}{\dot{\varepsilon}_0} \right)^{1/3} \tag{3.19}$$

where, C_2 is the material parameter and $\dot{\varepsilon}_0$ is the reference strain rate.

Strain rate effect on concrete is different for compressive and tensile loading (Figure 3.11). Tensile dynamic Increase Factor (F_{DIF}) is higher than that of the compressive loading. Unlike metals, concrete exhibits different strain rate effects at low to moderate and high strain rates. Strain rate effect is comparatively larger at a high strain rate. Figure 3.11 illustrates the significant increase in the strength at a critical strain rate value for both compression and tension, especially at a high strain rate. The critical strain rates for compression and tension are different. The values range between $60 \sim 80\ \text{s}^{-1}$ and $1 \sim 10\ \text{s}^{-1}$ for compression and tension, respectively (Ross et al., 1996; Tedesco et al., 1997; Tedesco and Ross, 1998). Below the critical strain rate, the rate effect is rather small and can be ignored. Therefore, only a single equation (Eq. 3.19) is adopted to attain the strain rate effect. The reference strain rate ($\dot{\varepsilon}_0$) usually 1 s^{-1}, and hence, Eq. (3.19) can be further simplified by removing $\dot{\varepsilon}_0$. Since concrete behaves differently in compression and tension two sets of equations one for compression and one for tension are proposed.

$$F_{DIF}^{C} = C_C \left(\dot{\varepsilon}\right)^{1/3} \qquad for\ \dot{\varepsilon} > \dot{\varepsilon}_{\text{limit}}^{C} \tag{3.20}$$

$$F_{DIF}^{T} = C_T \left(\dot{\varepsilon}\right)^{1/3} \qquad for\ \dot{\varepsilon} > \dot{\varepsilon}_{\text{limit}}^{T} \tag{3.21}$$

where, C_C and C_T are the strain rate constants for compression and tension, respectively, $\dot{\varepsilon}_{\text{limit}}^{C}$ and $\dot{\varepsilon}_{\text{limit}}^{T}$ are the limiting critical strain rates for compression and tension, respectively.

3.2.3.3 Pressure-Volume Relation

Dynamic loadings like high velocity impact and explosion causes high pressures in concrete material. These short term dynamic loadings introduce shock waves propagating through the concrete body. Concrete is a heterogeneous material consists of aggregate and mortar which makes it difficult to define shock wave propagation through the concrete body. An effective concrete material model should adopt this complex behavior of heterogeneous materials while using for simulations of dynamic loading cases.

In the MHJC model a multi-linear pressure – volume relationship is adopted. The model contains an elastic compression path from the negative pressure cutoff to the point of elastic limit P_{crush} and given as,

$$P = K\mu \tag{3.22}$$

where, K, $\mu\left(=\rho/\rho_0 - 1\right)$ and ρ_0 are the bulk modulus, volumetric strain and initial density. Negative pressure is limited by $f_t^{'}\left(1 - D_c\right)$ where, $f_t^{'}$ is the tensile strength and D_c is the damage.

Beyond the elastic limit, compaction of concrete takes place through failure and collapse of pores, and indeed, concrete gradually turns into a compact material. Pressure and volumetric strain at fully compacted concrete are referred to as P_{comp} and

μ_{comp} respectively. Unloading occurs along the modified bulk modulus which is defined as,

$$K_a = K\left(1 - D_c\right) + K_m\left(D_c\right) \tag{3.23}$$

$$D_c = \sum \frac{\Delta\mu^p}{\mu_m} \tag{3.24}$$

where, K_m is a material constant, $\mu_m \left(= \rho_m / \rho_0 - 1\right)$ and ρ_m are the volumetric strain and density of the fully compacted concrete respectively, and $\Delta\mu^p$ is the plastic volumetric strain increment. Density of the compacted concrete can be determined through weight proportion of dry concrete ingredients (Gebbeken et al., 2006) as follows,

$$\rho_m = \sum \frac{m_i\left(\%\right) \cdot \rho_i}{100} \tag{3.25}$$

where, m_i and ρ_i are mass and density of concrete ingredients. Reloading path follows the unloading path until it reaches the unloading beginning point, and continues following the loading path.

The pressure-volume relationship for fully compacted concrete ($P > P_{comp}$) follows a non-linear elastic behavior where loading and unloading follow the same path. Johnson and Holmquist (1994) proposed a third order polynomial equation to describe the pressure – volume relationship for brittle materials which is given as,

$$P = K_m\mu + K_l\mu^2 + K_n\mu^3 \tag{3.26}$$

where, K_m, K_l and K_n are material constants. Eq. (3.26) can be further simplified or linearized by ignoring the higher order terms,

$$P = K_m\mu \tag{3.27}$$

Shang et al. (2000) conducted high velocity impact test of Bukit Timah granite and reported the pressure – volume relationship shown in Figure 3.12. The figure includes Eq. (3.26) where material constants are determined using a regression analysis. Correlation coefficient for Eq. (3.26) is 0.993. Figure 3.12 also incorporates Eq. (3.27) for which the correlation coefficient is 0.986. Considering close relationship between two equations, the latter equation is adopted for fully compacted concrete in the proposed model. However, Eq. (3.27) only works for relative low pressure values (less than 8 GPa) which is well within the scope of this study. The pressure – volume behavior for fully compacted concrete is given as follows,

$$P = K_m \left(\mu - \mu_m \right) \tag{3.28}$$

Figure 3.13 describes the three regions of the pressure-volumetric relationship. First region depicts the elastic characteristics; whereas, the second region illustrates the pore compaction and concrete failure stage. The third region expresses behavior of fully compacted concrete. The relationship is incorporated in the MHJC model.

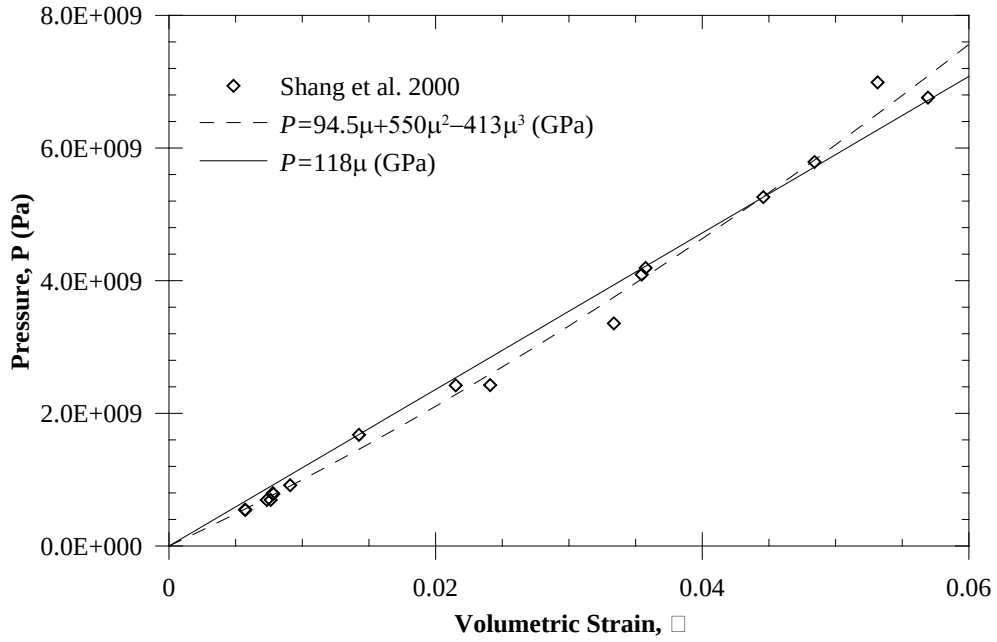

Figure 3.12 Pressure – volumetric strain plot for the Bukit Timah granite.

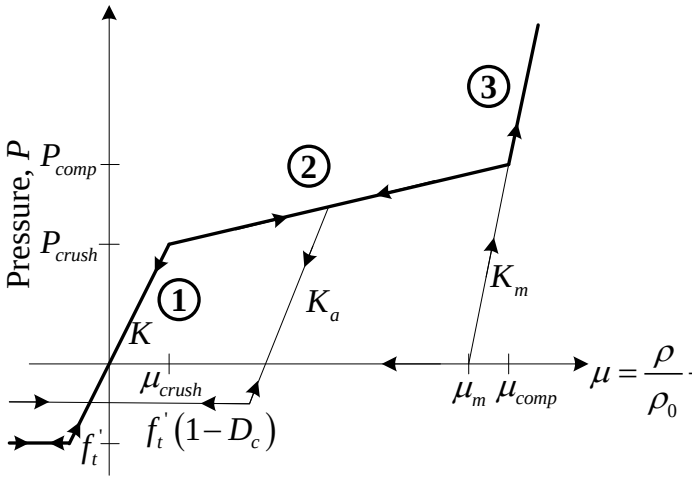

Figure 3.13 Relationship between pressure and volumetric strain.

3.2.3.4 Damage Model

The damage in concrete is defined in terms of effective plastic strain (Johnson and Holmquist, 1994) and expressed as,

$$D = \sum_{\Delta t} \frac{\Delta \varepsilon_{eff}^{p}}{\varepsilon_{f}^{p}} \tag{3.29}$$

where, the plastic strain to fracture is given as,

$$\varepsilon_{f}^{p} = d_g (P^* + \overline{f}_t')^{d_h} \geq \left(\varepsilon_{f}^{p}\right)_{\min} \tag{3.30}$$

in which, d_g and d_h are the damage constants and $\overline{f}_t' = f_t' / f_c'$ is the normalized tensile strength. The limiting value of $\left(\varepsilon_{f}^{p}\right)_{\min}$ is used to ensure reasonable plastic strain to fracture (Figure 3.14).

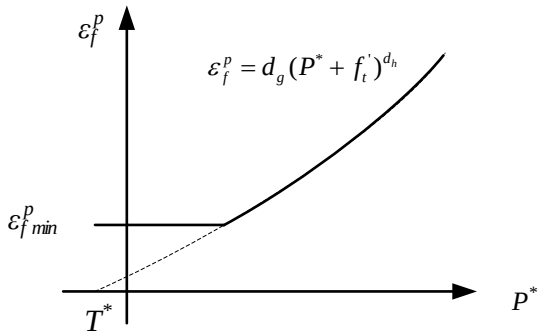

Figure 3.14 Damage model due to effective plastic strain.

3.2.4 Determination of MHJC Model Parameters

In establishing material parameters for the proposed MHJC model, several sets of test data are considered, where concrete strength and density vary between 25 to 75 MPa and 2200 to 2450 kg/m^3. The first step is to attain the strength parameters $\mathcal{A}$, $\mathcal{B}$ and $\mathcal{N}$ using the test data given by Hanchak et al. (1992), Imran and Pantazopoulou (1996) and Candappa et al. (1999). The parameter, $\mathcal{A}$ defines the strength between undamaged (D = 0) and totally damaged (D = 1) concrete at a given pressure. Cracks form in concrete at the interface of mortar and aggregate even before loading starts (Hsu et al., 1963). These bond cracks start to grow around 30% of the compressive strength of concrete (Buyukozturk et al., 1971). At about 70% of the compressive strength of concrete, mortar cracks form, and indeed, connect the bond cracks to form continuous cracks (ACI Committee, 2001). Based on the formation of continuous cracks, $\mathcal{A}$ is assumed to be 0.7. Parameters $\mathcal{B}$ = 1.8 and $\mathcal{N}$ = 0.54 can be attained using the best fit method as shown in Figure 3.15.

The strain rate parameters are determined next. As illustrated in Figure 3.11, strain rate effects in compression are different from those in tension, and hence, require two sets of parameters (Eqs. 3.20-3.21). After observing the test data, limit strain rates are considered to be 40 s^{-1} and 1 s^{-1} for compression and tension respectively. Least square method is adopted to calculate the strain rate constants, C_C and C_T, from the test data of F_{DIF} at various strain rates larger than the limit strain rates (Donzé et al., 1999; Gary and Klepaczko, 1992; Malvern et al., 1985; McVay, 1988; Mellinger and Birkimer, 1966; Ross et al., 1996; Ross et al., 1989; Tedesco et al., 1997; Tedesco et al., 1993). Test data showed the compressive strength of concrete in the range of 40 – 65 MPa. It is assumed in this study that strain rate effect is independent of compressive strength within this range. The limit strain rates are

measured based on the C_C and C_T and given in Table 3.3. Comparison of the MHJC model equations with the experimental data show good agreement as demonstrated in Figure 3.16.

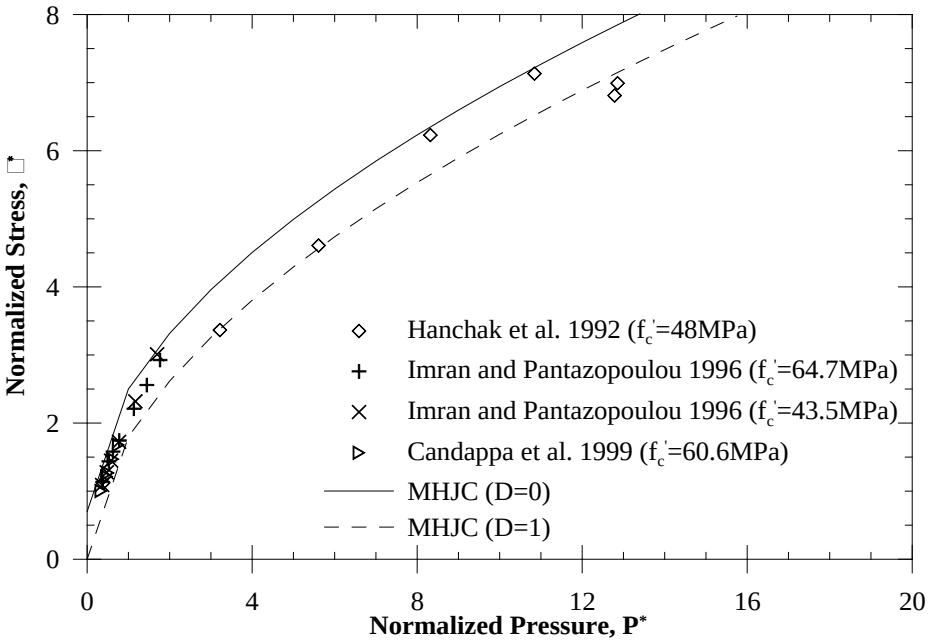

Figure 3.15 Comparison of the experimental and MHJC model on normalized stress-pressure relationship.

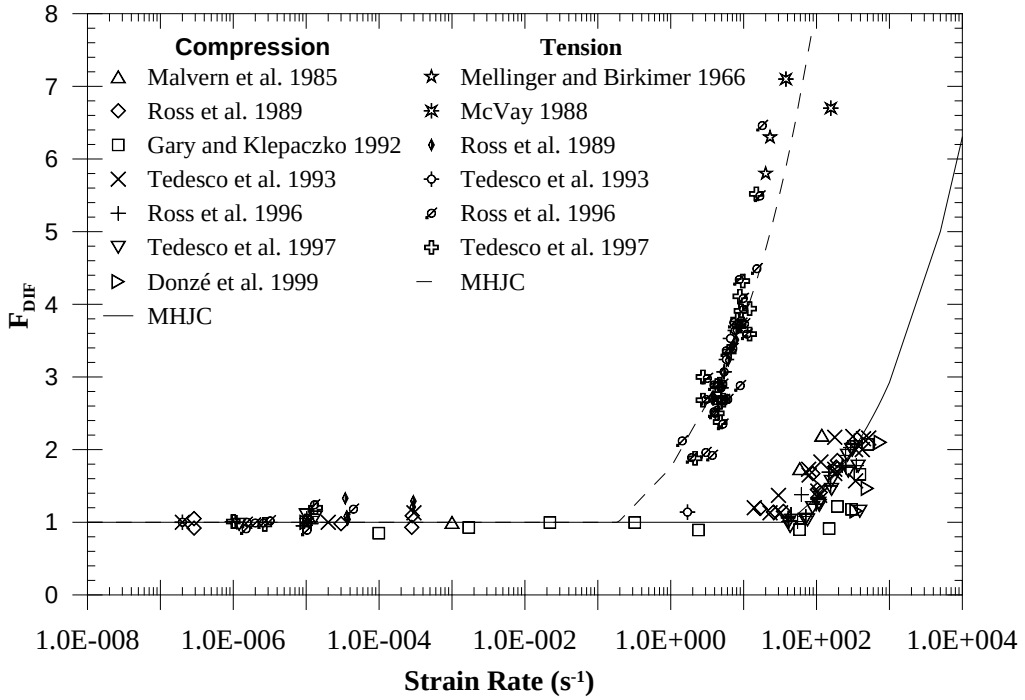

Figure 3.16 MHJC model strain rate effects expression against the experimental data.

Table 3.3 MHJC model strain rate parameters

C_C	$\dot{\varepsilon}^C_{\text{limit}}$	C_T	$\dot{\varepsilon}^T_{\text{limit}}$
0.29	40.0	1.75	0.2

Calculation of the material constants for the pressure – volume relationship is straight forward. Determination procedure is described herein using the test data from Hanchak et al. (1992) for a concrete specimen with compressive strength of 48 MPa. The elastic limit pressure constants $P_{crush}\left(=f_c'/3\right)$ and $\mu_{crush}\left(=P_{crush}/K\right)$ are determined first. For concrete with f_c' = 48 MPa, P_{crush} is 16 MPa and μ_{crush} is 8x10^{-5} for bulk modulus of 19.83 GPa. Density of the fully compacted concrete is obtained next using Eq. (3.25). However, lack of adequate information makes it difficult to identify ρ_m for this case and a value of 2767 kg/m^3 is chosen based on the results from Gebbeken et al. (2006). Volumetric strain of the compacted concrete $\mu_m\left(=\rho_m/\rho_0-1\right)$ is determined using ρ_m=2767 kg/m^3 and ρ_m=2440 kg/m^3. Parameter K_m for fully compacted concrete is acquired from Shang et al. (2000) through the least square method. Finally, parameters P_{comp} and μ_{comp} are calculated from the intersection of the second and third region expressions. Damage parameters d_g, d_h and $\left(\varepsilon_p^f\right)_{\min}$ are selected from literature (Holmquist et al., 1993). Table 3.4 summarizes all the material properties required for the proposed MHJC model and adopted herein. Pressure – volumetric relationships of concrete are determined and compared with the experimental results in Figure 3.17. Predicted data shows a good correlation with the experimental observations.

Table 3.4 MHJC model parameters for 48 MPa concrete

K (GPa)	f_c' (MPa)	f_t' (MPa)	ρ_0	$\mathcal{A}$	$\mathcal{B}$	$\mathcal{N}$
19.83	48	4	2440	0.7	1.8	0.54
P_{crush} (MPa)	μ_{crush}	μ_m	P_{comp} (GPa)	μ_{comp}	K_m (GPa)	
16	0.0008	0.134	1.025	0.1427	118.0	
d_g	d_h	$\left(\varepsilon_p^f\right)_{\min}$				
0.04	1.0	0.01				

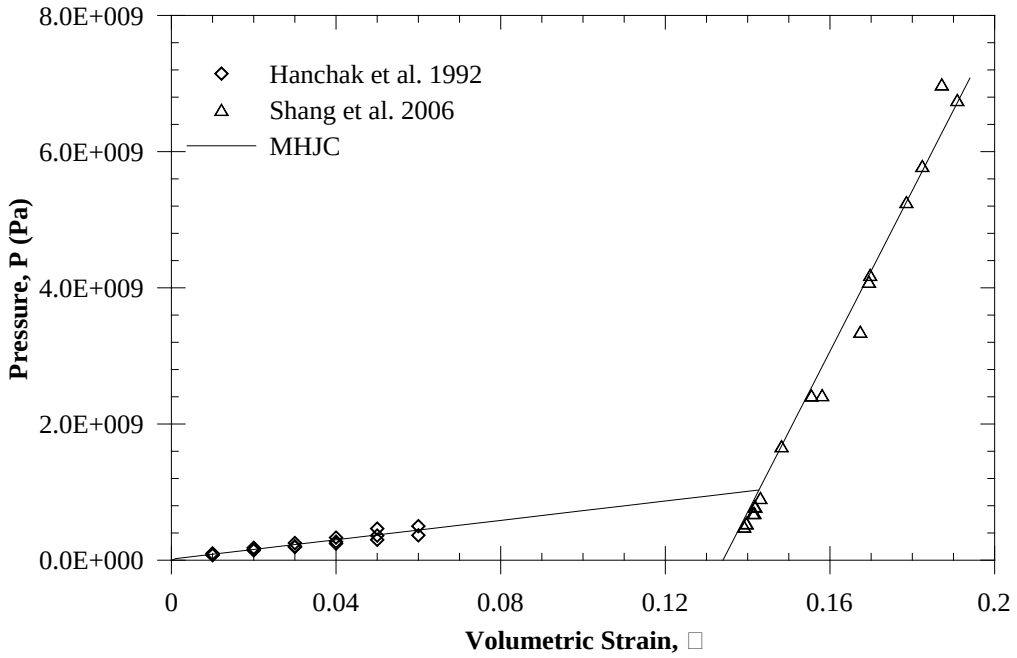

Figure 3.17 Comparison of the experimental and model pressure and volumetric strain relationships.

3.3 Conclusions

Two new models for metals and concrete are discussed in this chapter. The MJC model for metals includes strain rate and temperature effects especially at adiabatic conditions. Determinations of material properties are straight forward and applicable for most metals. The MJC material model parameters for titanium alloy Ti-

6Al-4V and Weldox 460 E steel are obtained, and it shows good agreement with the test data compare to the JC model results. The proposed MJC model is adopted through user defined material model in the software package LS-DYNA. The MHJC model for concrete consists of a simple strength, strain rate and pressure-volume relationship. Material properties are determined for concrete with compressive strength ranging from 40 - 60 MPa and density varying between 2200 - 2400 kg/m^3. The model is implemented as a user defined material model in the software package LS-DYNA.

Chapter 4 Impact Simulations Using Coupled SPH-FE Method (SFM)

4.1 Introduction

In the latest half century, numerical methods become the alternative to the analytical methods and even emerge as the sole approach for comparison with the experimental data when the analytical representations become inadequate or unable to attain. Numerical simulation of impacting objects must account for the thickness of the target, nose geometry of the projectile, effect of the high strain rate, frictional and thermal effects, and damage. Failure patterns of the target depend on the relative thickness of the target plate and the projectile nose shape. Failure patterns determine the ballistic performance of the colliding bodies, and hence, it is imperative to study the effect of target thickness and projectile nose geometry. High strain rates in the range of $10^2 – 10^4$ s^{-1} are detected at the target during the high velocity impact events. Since, high strain rate has a positive effect on material strength of most materials, it is necessary to include it in the material constitutive model. Effects of friction between the projectile and target, and adiabatic thermal condition during the high velocity penetration/perforation need significant study. Material damage occurs at the various stages of penetration and requires considerable contemplation.

Finite element method is currently the most popular numerical method for high velocity impact simulations, but it has a major drawback (as mentioned in Chapter 2), like severe element distortion problem. In order to avoid this problem, coupled smooth particle hydrodynamics – finite element method (SFM) has been introduced for the high velocity impact problems. Dynamic response of the structures

under high velocity impact simulations using SFM are presented in this chapter. Numerical simulations are performed using hydrocode LS-DYNA (Hallquist, 2006). In order to examine the performance of the SFM, three examples including perforation of steel plate of various thicknesses by blunt projectile, steel plate perforation by projectiles with various nose geometries (blunt, conical and ogival), and perforation of aluminum plate of various thicknesses by conical nose projectile. The results from the SFM are compared with experimental data. These examples demonstrate that the SFM is a robust and reliable method for studying high velocity impact studies for metals. It also provides a basic understanding for other high velocity impact problems.

4.2 Steel Plate Perforation Using SFM

Perforation simulation of Weldox 460 E steel plates of varying thicknesses impacted by projectiles of various nose shapes are performed in this section. Geometries of the three different nose shaped projectiles are depicted in Figure 4.1 (Dey, 2004). The modeling of each target plate comprises two regions. The SPH particles are adopted in the impact vicinity where damages and large deformation are expected while the rest of the target domain and the projectile are modeled using the FE 8-node solid elements with coarser mesh towards the outer boundary of the plate as illustrated in Figure 4.2. Only a quarter of the problem is modeled using symmetry in *xz* and *yz* planes where symmetry boundary conditions are imposed for FEM mesh and a set of ghost particles are defined to enable the symmetry conditions for the SPH region. The SPH particles and the finite elements surfaces are inter connected using a tied-nodes-to-surface contact feature. Contact between the projectile and the target plate is defined using an automatic-nodes-to-surface contact option.

Johnson-Cook (JC) material model is adopted for the target plates while each projectile is modeled as a simple elastic-plastic material with isotropic hardening.

Though certain fragmentation and shattering of projectiles for thick steel plates at high initial projectile velocities were observed during the penetration test, damages in the projectiles are not considered in the present study. The relevant material parameters for steel target plates and hardened steel projectile are listed in Tables 4.1-4.2 respectively.

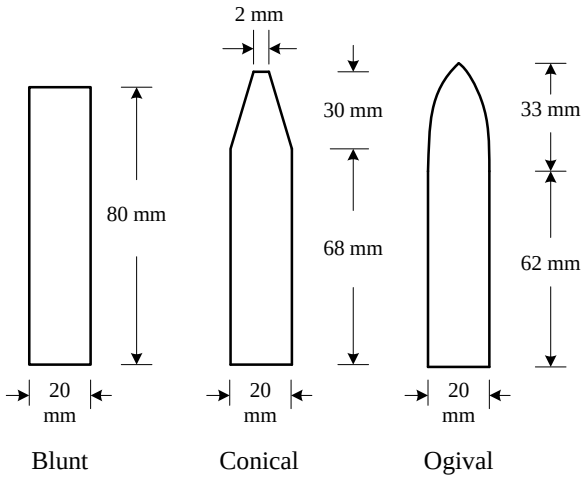

Figure 4.1 Geometry and dimension of the various nose shaped projectiles.

Table 4.1 JC Material properties for Weldox 460 E steel plate (Dey, 2004)

ρ_0 (kg/m^3)	E (GPa)	v	G (GPa)	A (MPa)	B (MPa)
7850	210	0.33	75	499	382
A	C	b	C_p (J/kgK)	T_m (K)	T_r (K)
0.458	0.0079	0.893	452	1800	293
D_1	D_2	D_3	D_4	D_5	
0.636	1.936	-2.969	-0.014	1.014	

Table 4.2 Material properties for hardened Arne tool-steel (Dey, 2004)

σ_Y (GPa)	ρ_0 (kg/m^3)	E (GPa)	v	E_t (GPa)	$\left(\varepsilon_f\right)_{mean}$ (%)
1.9	7850	204	.33	15	2.15

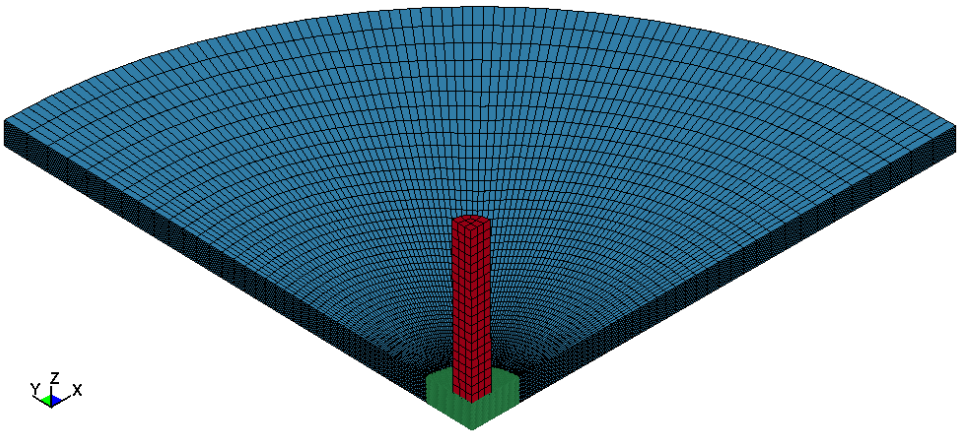

Figure 4.2 Mesh of the target and projectile numerical model.

4.2.1 Domain Size Sensitivity Study

The choice of proper SPH domain size is studied to balance the adequate requirement of the SPH region and the economy of computational resources. Deformation region governs the SPH domain size. Zukas (1995) reported a severe deformation zone of 3-6 times the projectile diameter for ballistic impact cases. Three SPH domain radii of 24, 30 and 36 mm are adopted in this study expecting a severe deformation zone of 2.4-3.6 times the projectile diameter. Domain size sensitivity studies are performed on blunt projectile perforation of two Weldox 460 E steel plates of thicknesses 8 and 16 mm. Numerical residual velocities of the projectiles are compared with the experimental results as shown in Figure 4.3. Numerical residual velocities for the 8 mm thick plate deviate from the experimental results for strike velocity less than 170 m/s. This inconsistency is due to the fact that the SFM is unable to consider the change in failure pattern from shear failure for thick plates to global dishing failure for thin plates.

As all three sets of results show good convergence for both cases, the SPH domain radius (r) of 24 mm is used in subsequent analyses. Normally, the SPH domain radius size of about two to three times the projectile diameter is adequate for the SFM.

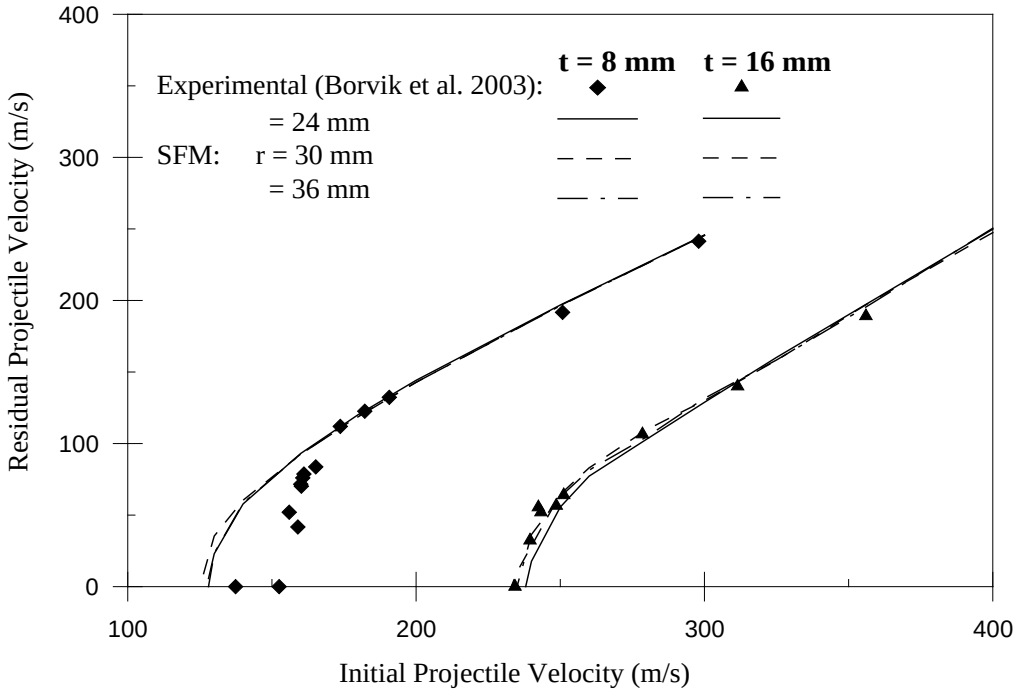

Figure 4.3 Domain size sensitivity study for steel plates perforated by blunt projectile.

4.2.2 Effect of SPH Particle Distance

Initial numerical results of blunt projectile perforation of steel plate using SFM showed that the residual velocities are sensitive to the SPH particle distance. The phenomenon of mesh sensitivity is also observed for FE simulation by Dey (2004) who stipulated that it is due to the localized adiabatic shear failure around the periphery of the projectile. Therefore, the study is conducted to study the effects of the SPH particle distance for two sampled plate thicknesses of 8 and 16 mm. The results from the SPH convergence study of the two cases as shown in Figure 4.4.

As observed in the figure, at relatively low initial projectile velocity, the particle distance plays a stronger effect. For high initial projectile velocity, failure pattern is mostly localized shear failure. However, at relatively low velocity, failure pattern of the target metallic plate consists of shear failure around the edge of the projectile and tensile failure at rare surface of the plate, where the tensile failure is most prominent with low initial velocity. The SPH method suffers from the tensile instability problem which can be reduced by using more particles with less particle

distance size. Considering these factors, it is safe to conclude that the particle distance demonstrate a stronger effect at low initial velocity due to change in failure pattern of the target plate.

As shown in Figure 4.4, a reasonable convergent result can be achieved using the SPH particle distance of 0.6 mm and the value is adopted in subsequent computations. The effects of the SPH particle distance are also studied for sharp nose projectiles and the results indicate the same particle distance of 0.6 mm to be adopted.

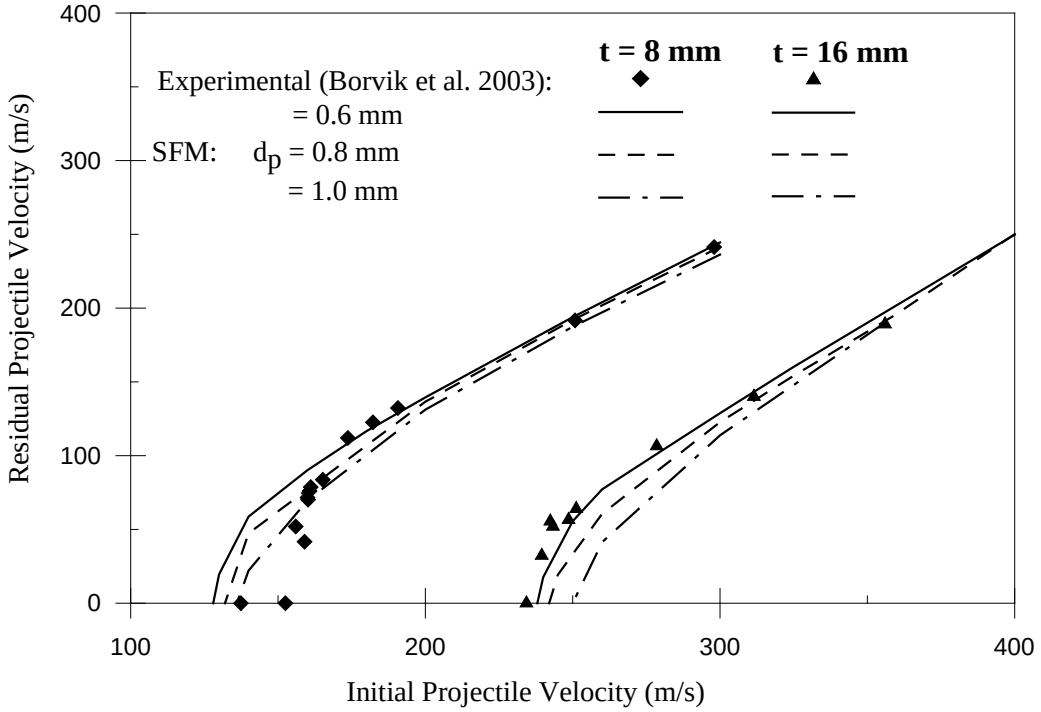

Figure 4.4 SPH particle distances (d_p) sensitivity study for steel plate perforation by blunt projectile.

4.2.3 Effect of Friction

The melting temperature and the strength of the target material affect the values of the friction coefficient to be used in the study. The lower melting temperature tends to induce a thin layer between the target and projectile that acts as a lubricant. The photomicrograph of the penetration of target plates by a spherical nose projectile at 1120 m/s initial velocity showed significant micro-structural changes in a thin layer of 5-15 μm in the target around the projectile (Forrestal et al., 1988).

Similar behavior was also observed for other sharp (such as conical and ogival) nose projectiles. At the contact surface between the target and the projectile, the target materials flow both up and down. The phenomenon suggests that sliding friction between the projectile and the target exists and has to be considered. No such layer was observed for blunt projectile perforation as the target plate failed by localized adiabatic shear failure (Dey, 2004) inducing negligible contact friction between the projectile and the target. This is confirmed by the observed constant residual velocity after the failure of the target by adiabatic shear and plugging of blunt projectile as reported earlier by Børvik et al. (2003).

Selecting a proper value of the friction coefficient, μ_f, is not easy as no direct experimental data are readily available for high velocity impact. Ravid and Bodner (1983) assumed the values of μ_f = 0.1 and μ_f = 0.05 in high velocity rigid projectile perforation of steel plates for frontal and lateral projectile surfaces respectively. Lower value for the lateral projectile surface was expected due to the effect of high velocity and the presence of thin viscous film as material temperature rises beyond the melting point at contact surfaces. Three different values of friction coefficients of 0.05, 0.08 and 0.1 are used to study the perforation of the conical nose steel projectile into the steel target plate. The residual versus the initial projectile velocity plots adopting the above three μ_f values as shown in Figure 4.5 illustrate a significant effect of friction on the residual velocity. The in-between value of 0.08 for μ_f seems to provide reasonably accurate results simulated via SFM and is adopted in subsequent simulations of conical and ogival nose projectile perforations.

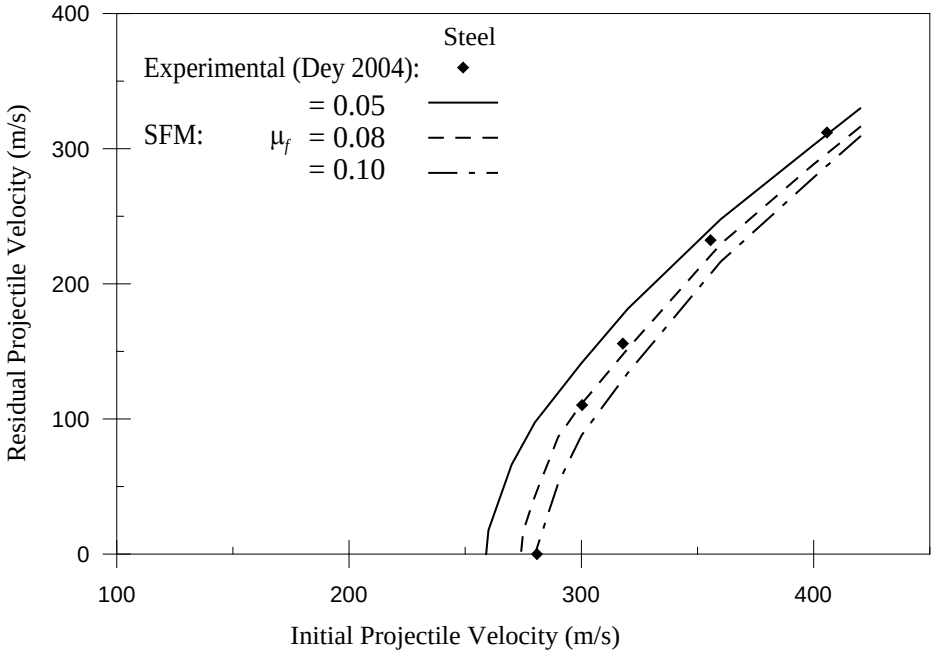

Figure 4.5 Effect of friction in conical projectile perforation of steel plates.

4.2.4 Blunt Projectile Perforation

Perforations of steel plates with thickness ranging from 6 to 20 mm by blunt projectile using the 3D SFM have been carried out. Numerical residual and ballistic limit velocities are compared with the experimental data from Børvik et al. (2003). Figure 4.6 shows the residual velocity versus the initial velocity plots for various plate thicknesses. Except for thin plates at relatively low initial projectile velocities of about 170 m/s and less, the SFM results agree well with experimental values. During the experiment, Børvik et al. (2003) observed a sudden drop in the projectile residual velocities for perforation of 6 and 8 mm thickness target plates. However, this is not apparent in numerical solutions and the residual velocities for various plate thicknesses are well distributed.

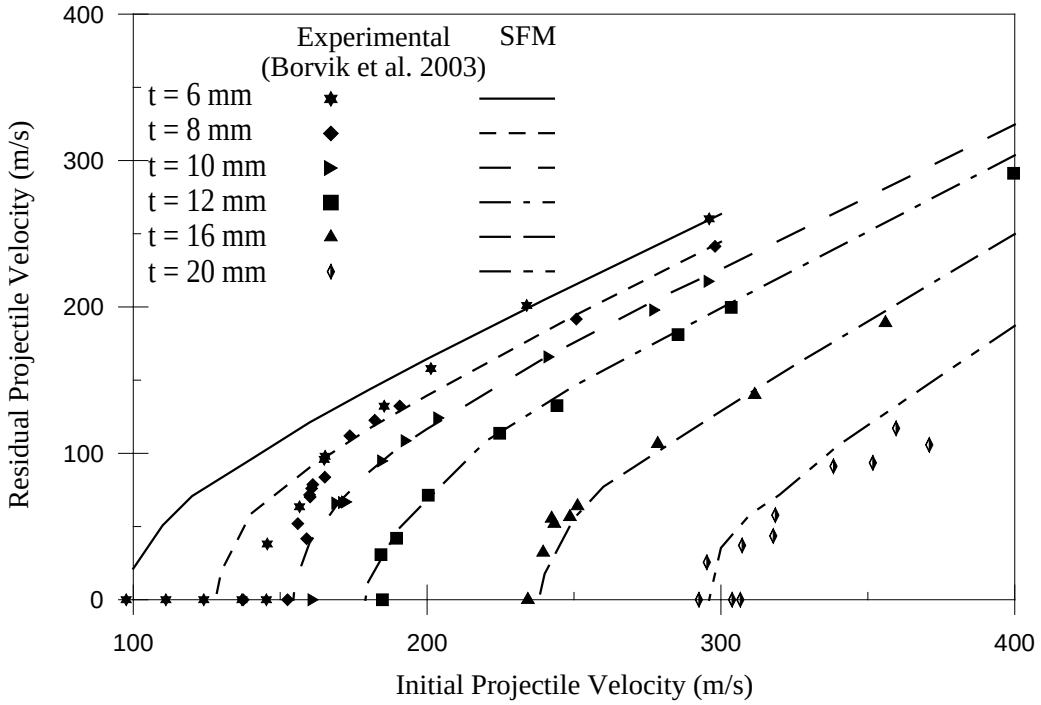

Figure 4.6 Numerical and experimental residual velocities for blunt projectile perforating steel plates.

The deviation of the SFM simulation for an impact velocity that is less than 170 m/s is mostly due to the change in failure pattern of the relatively thin target plate from the failure mode for the thick plate. For relatively thin plate and/or low initial projectile velocity, failure of the plate consists of localized shear, bending and large global deformation, where the global deformation absorbs a considerable portion of the kinetic energy of the projectile. With increasing plate thickness and/or striking velocity, failure pattern changes into localized shear failure along the edge of the projectile. Because of the inherent tensile instability problem of the SPH method, premature tensile failure of the target plate occurs for relatively thin plate and/or low initial projectile velocity which results in an over estimation of the residual projectile velocity. However, for relatively thicker plate and/or high initial velocity, failure is more likely shear failure rather than tensile failure, and thus, tensile instability problem is significantly small.

Ballistic limit velocity is defined as the minimum projectile velocity needed to penetrate the whole target plate. In the simulation, the ballistic limit velocity is considered as the minimum initial velocity that perforates the target completely and emerges with a residual velocity around zero. Ballistic limit velocities for various plate thicknesses of 6 mm to 20 mm are illustrated in Figure 4.7. The SFM provides a good representation of the experimental results for plate thickness of 10 mm and above but seems to underestimate the experimental ballistic limit velocities for those of 8 mm and below. A certain change in the slope of the curve is evident for the experimental results at a plate thickness of 10 mm. This difference in slope was explained by Børvik et al. (2003) as the change in failure mode from adiabatic shear and plugging failure for thick plates to global dishing and plugging failure for thin plates.

Similar study is performed using 3D finite element method (FEM). To avoid the severe element distortion problem in FEM, damage based element erosion method is used for the target plates. Based on the convergence study, the element size of 0.25 x 0.25 x 0.25 mm^3 is adopted to model the target plate in the impact vicinity and a gradually coarser mesh is used towards the outer edge. The FEM results, along with the SFM values as displayed in Figure 4.7, predicts a change in slope similar to those observed in the experiments. The SFM residual velocity versus the initial velocity plots for 6 and 8 mm thick plates are shown in Figure 4.8. The FEM results for 6 and 8 mm thick plates are also included for comparison. It is apparent from the figure that the FEM provides better comparison at relatively low initial velocities.

The perforation by blunt projectiles at lower initial projectile velocity (170 m/s or less) seems to be better simulated via FEM, while the SFM simulation performs better at higher initial velocities. Because of the severe element distortion and target damages in FE model, the FEM requires four to five times more computational time

than those of the SFM for these cases. Appropriate numerical approach for relatively thin plates, depending on the level of impact velocities, should be judiciously selected.

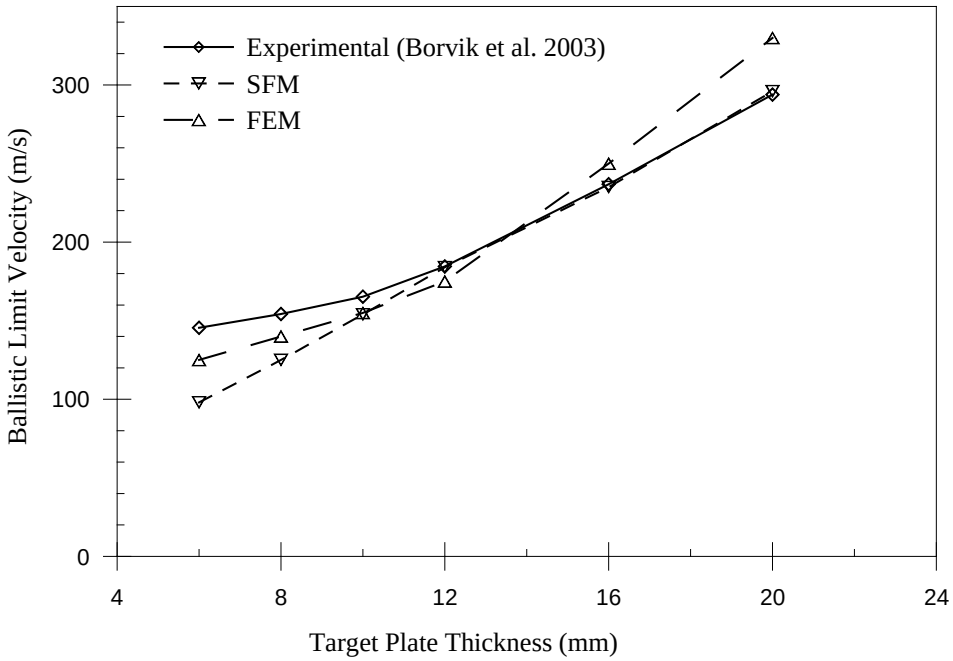

Figure 4.7 Numerical and experimental ballistic limit velocities for blunt projectile perforating steel plates.

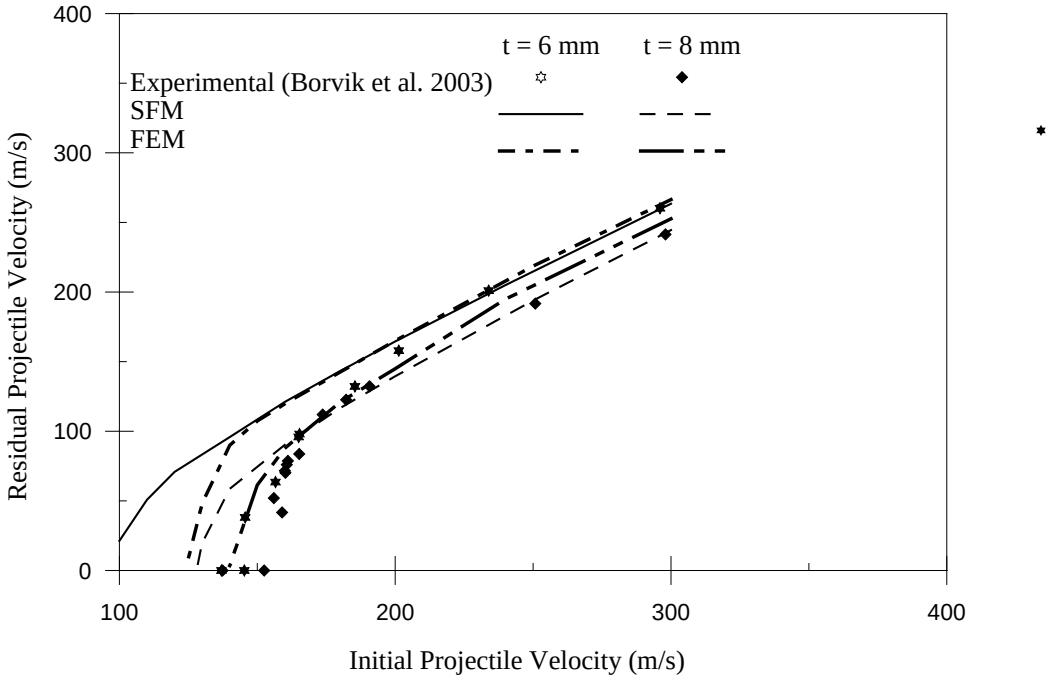

Figure 4.8 Better performance of FEM as compared to SFM at low initial velocity perforation.

Numerical study is carried out for 12 mm thick plate perforation using only smooth particle hydrodynamics (SPH) method in the target domain. Projectile is modeled as usual with the FEM. Because of the large target domain size, the system restricts the use of more particles at 0.6 mm particle distance for the SPH part. There remain two options, either use a smaller target domain size or adopt a larger particle distance. Since smaller domain size may cause boundary effects, the latter option is selected for the current study. A particle distance of 2.0 mm is chosen for the SPH target part. Comparison of the SPH and SFM results is shown in Figure 4.9. As observed in the figure, both SFM and SPH simulation results agree quite well with each other and show similar trend with some deviation compare to the experimental observations. A smaller particle distance would provide a closer agreement with the experimental results. However, computational resource requirements for the SPH method analysis are substantially higher than those of the SFM which make it ineffective for these cases.

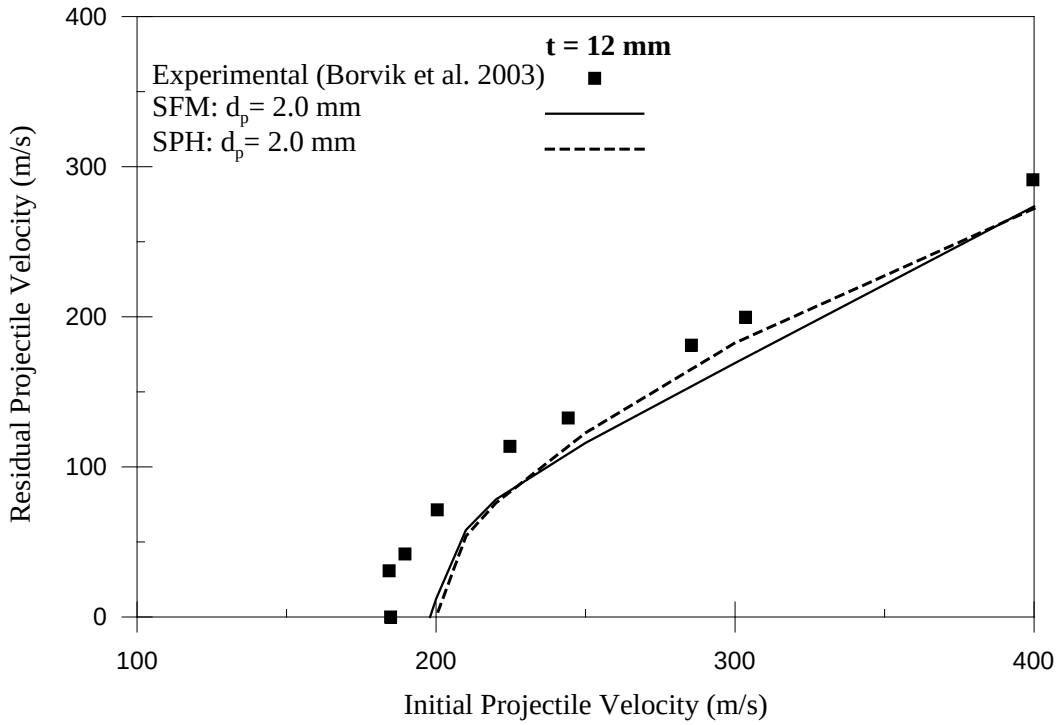

Figure 4.9 Performance study of SFM and SPH method for steel plate perforation by blunt projectile.

4.2.5 Perforation by Projectiles of Various Nose Geometries

Perforations of 12 mm thick Weldox 460 E steel plates by blunt, conical and ogival nose shaped projectiles are carried out. Numerical residual and ballistic limit velocities are compared with the experimental data from Dey (2004). The numerical results agree well with the experimental data as shown in Figure 4.10. Table 4.3 shows that the SFM ballistic limit velocities for these cases deviate less than 6% from the experimental values. Failure patterns of the target plates due to perforation of the three different projectile nose geometries, as illustrated in Figure 4.11, are similar to the experimental observations reported by Dey (2004). For blunt projectile, the failure of the plate is via adiabatic shear and plugging modes with a plug thickness close to that of the plate. The spherical and conical projectiles are observed to progress through each target by moving material in the radial direction and ductile hole enlargement with petal pattern detected at the rear surface.

Table 4.3 Ballistic limit velocity (v_{bl}) for three different projectiles

	Ballistic limit velocity, v_{bl} (m/s)		
	Blunt	Conical	Ogival
Experimental (Dey, 2004)	184.5	290.6	295.9
SFM	184.0	275.0	284.0

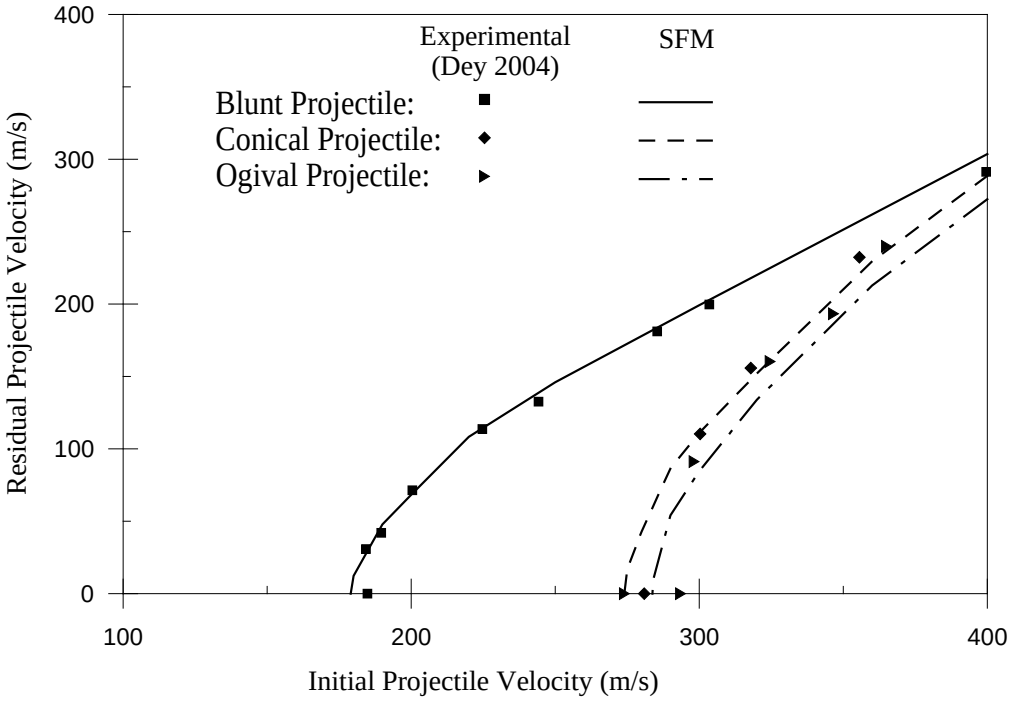

Figure 4.10 Comparison of numerical and experimental (Dey, 2004) residual velocities.

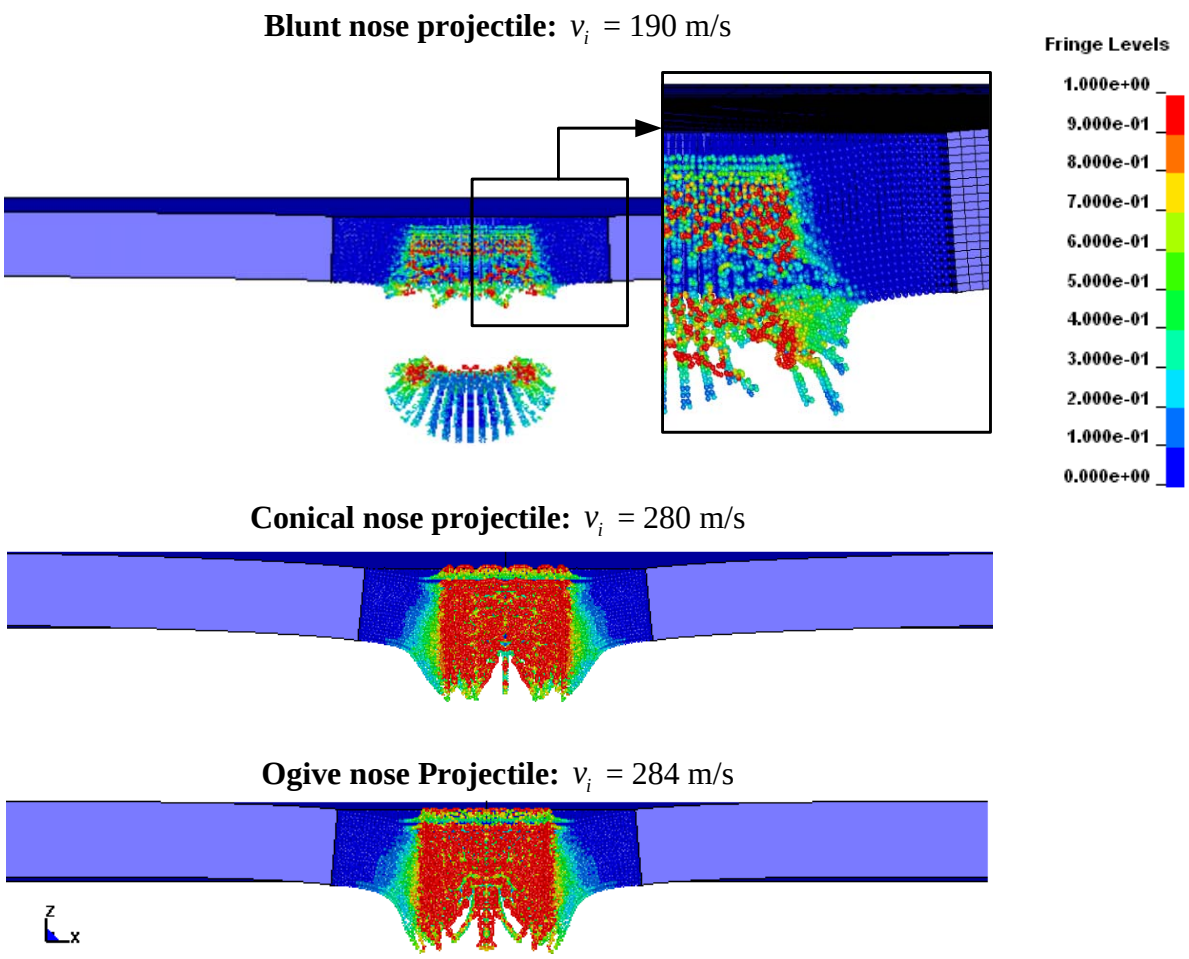

Figure 4.11 Steel plates after perforation showing effective plastic strain fringe contour.

4.3 Perforation of Aluminum Plate

Perforations of AA5083-H116 aluminum plates with thickness ranging from 15 mm to 30 mm by conical nose projectile using the SFM have been performed. The SPH domain radius (r) of 24 mm is used for aluminum plates as the projectile diameter is similar to the earlier study (Section 4.2.1). As discussed in Section 4.2.2, the SPH particle distance of 0.6 mm for sharp nose projectile is also adopted in this case. Numerical model of the target and projectile is illustrated in Figure 4.12. Johnson-Cook (JC) material model is used for aluminum plate. Strength material properties (A, B and a) of the aluminum plates vary with plate thicknesses. The variations in the strength parameters are due to different manufacturing process. Generally, thick plates are only hot rolled during tempering; whereas, thin plates are hot rolled before cold rolling. Because of this variation in tempering process, microstructure might change a little which explains the variation in strength parameters (Børvik et al., 2009). However, it is assumed that strain rate and temperature parameters do not effect by this and remain the same for all plate thicknesses. JC material properties of various thickness of aluminum plate are shown in Tables 4.4 – 4.5.

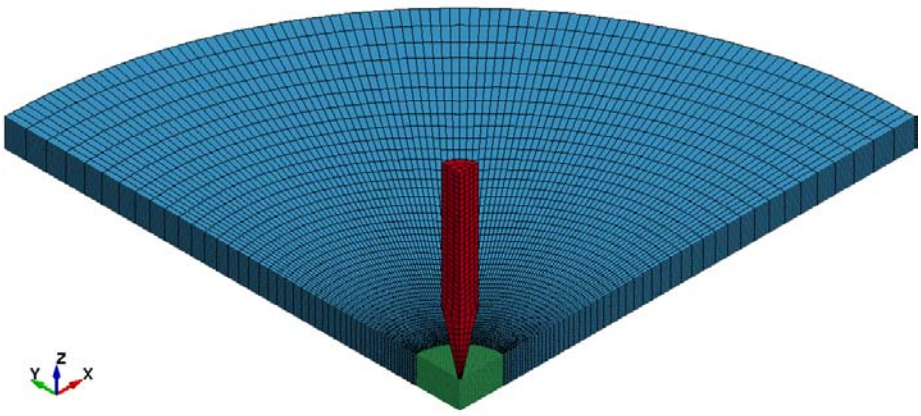

Figure 4.12 Target and conical projectile numerical model for aluminum plate perforation.

Table 4.4 JC Material properties for AA5083-H116 aluminum plate (Børvik et al., 2009)

ρ_0 (kg/m^3)	E (GPa)	v	G (GPa)	C	b	C_p (J/kgK)	T_m (K)	T_r (K)
2700	70.0	0.3	27.0	0.008	0.859	910	893	293

Table 4.5 JC Material properties for various thickness of AA5083-H116 aluminum plate (Børvik et al., 2009)

Plate thickness (mm)	A (MPa)	B (MPa)	a
15	143.0	462.0	0.216
20	124.0	456.0	0.252
25	59.0	511.0	0.285
30	119.0	475.0	0.256

4.3.1 Effect of Friction

Effect of sliding friction between the conical nose projectile and target is significant and cannot be ignored. Forrestal et al. (1988) suggested the values of friction coefficients of 0.02 to 0.20 for sharp nose steel projectile penetration into 6061-T651 aluminum targets. Figure 4.13 compares the experimental data with those obtained based on the μ_f values of 0.0, 0.02 and 0.05 for 15 mm thick AA5083-H116 aluminum plate perforation by conical nose steel projectile. For this case the JC material model is used for the aluminum plate. The numerical results using the value of 0.02 as suggested by Montgomery (1976) are observed to agree well with those from the impact tests. This value is adopted for subsequent aluminum plate perforation studies.

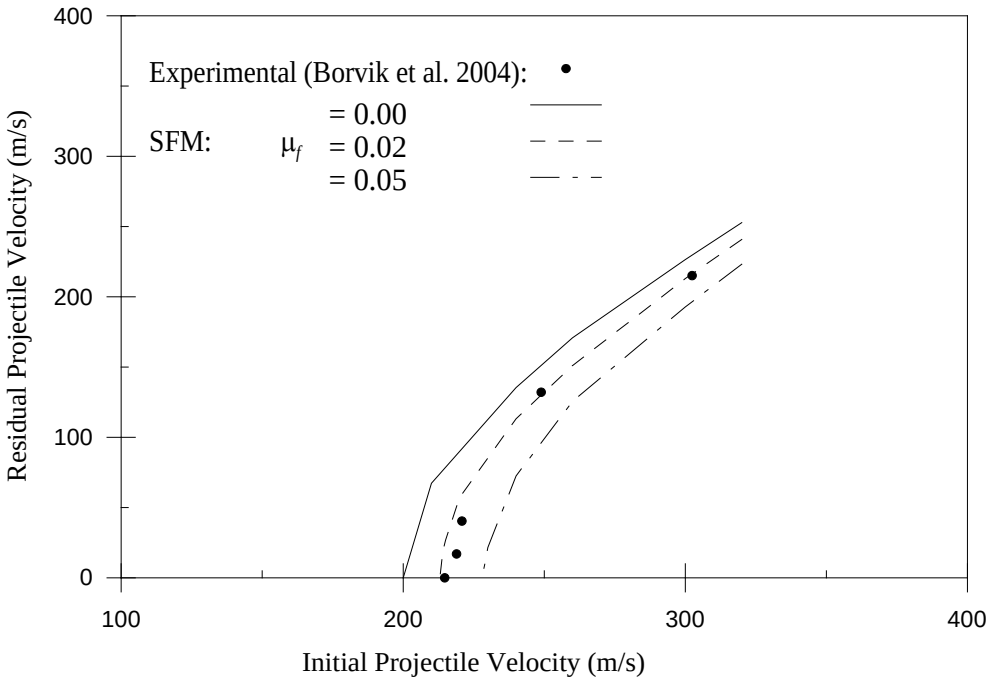

Figure 4.13 Effect of friction in conical projectile perforation of aluminum.

4.3.2 Perforation by Conical Nose Projectile

Numerical residual projectile velocities and ballistic limit velocities are compared with the experimental data reported earlier by Børvik et al. (2004). Variation of the residual velocities with the initial velocities for different plate thicknesses of 15, 20, 25 and 30 mm are presented in Figure 4.14. Ballistic limit velocities increase linearly with increasing plate thicknesses as shown in Figure 4.15 indicating a similar failure pattern for all plate thicknesses. The SFM results show a good agreement with those observed in the experiments. The plate fails due to ductile hole enlargement, forming petals at the rear surface of the target plates. Figure 4.16 illustrates the target plates after perforation of the projectiles at or near the ballistic limit velocities. Petals are observed and the failure patterns are consistent with the experimental observation (Børvik et al., 2004). The fringe contour of the effective plastic strain confirming the confinement of plastic deformation within the SPH portion is also demonstrated in Figure 4.16.

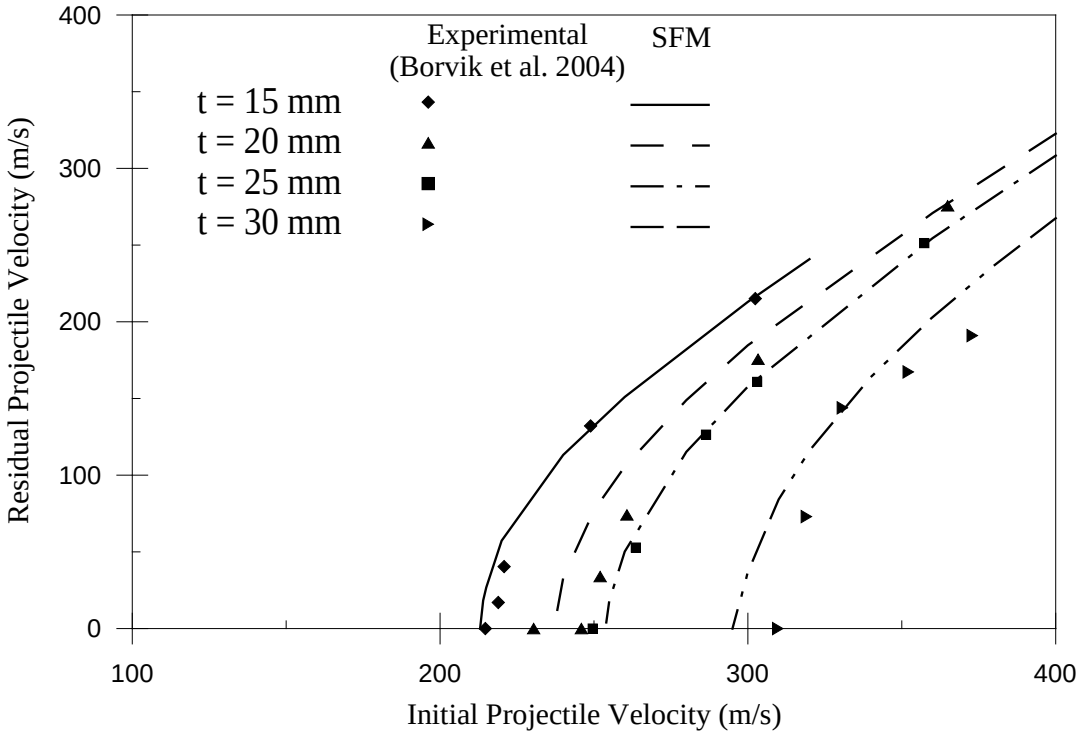

Figure 4.14 Numerical and experimental residual velocities of conical projectiles perforating aluminum plates.

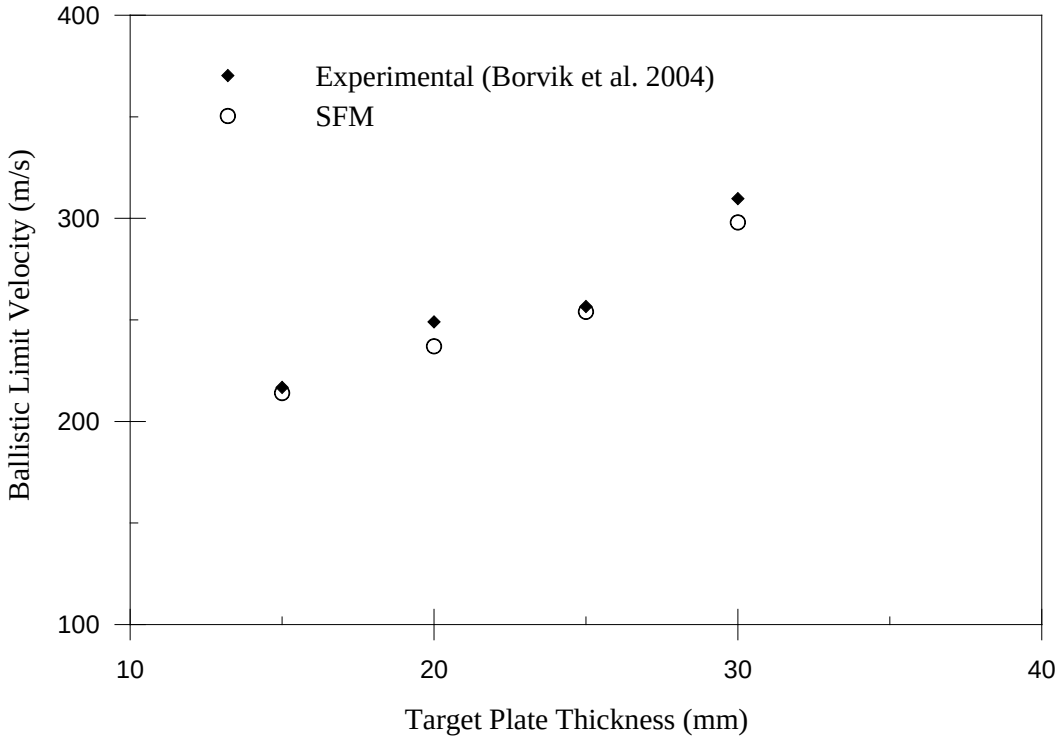

Figure 4.15 Numerical and experimental ballistic limit velocities for aluminum plate perforation.

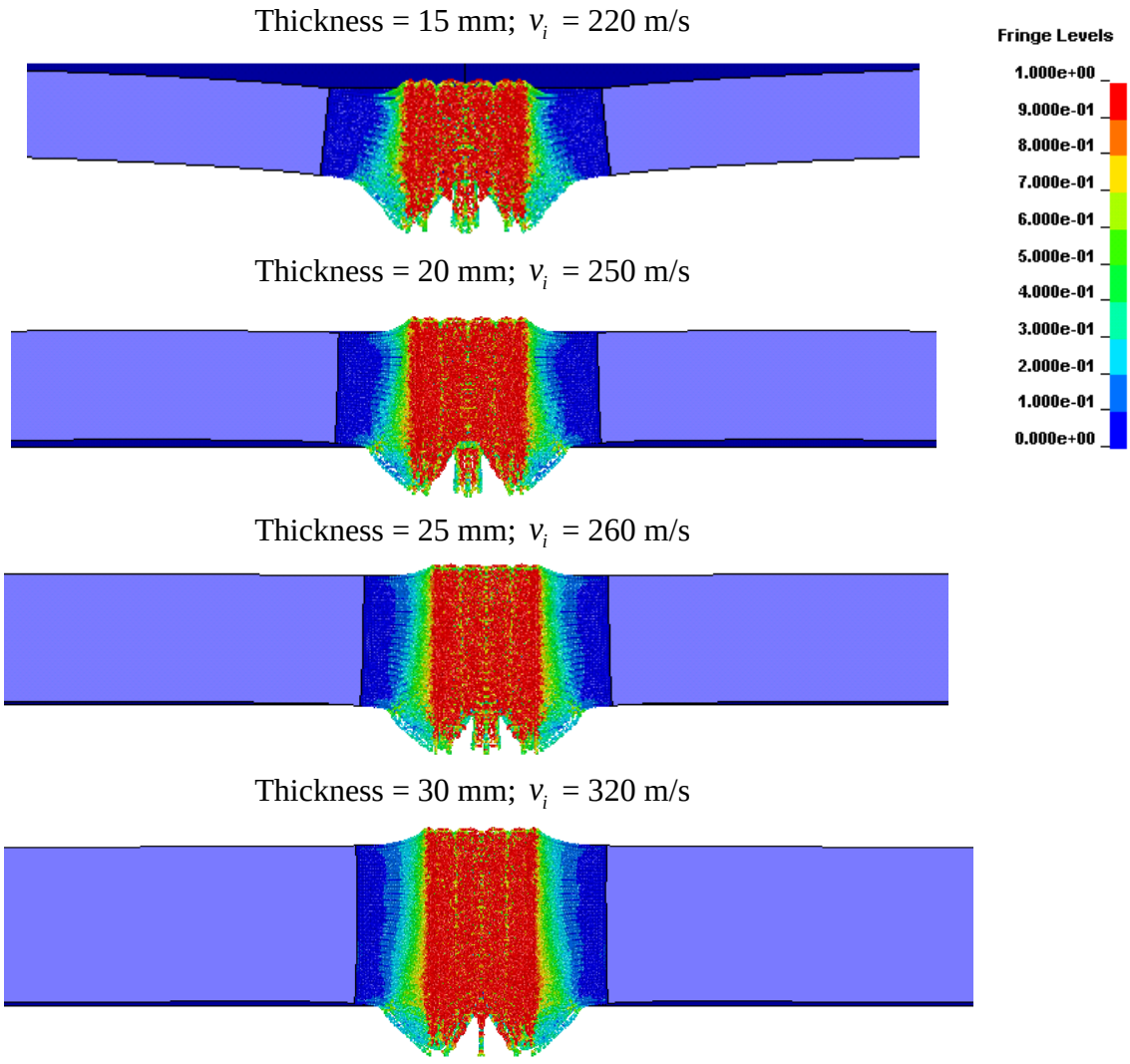

Figure 4.16 Aluminum plates after perforation by projectile at/near ballistic limit velocities with effective plastic strain fringe contour.

4.4 Conclusions

The coupled SPH-FEM (SFM) is adopted to simulate high velocity perforation of steel and aluminum plates of different thicknesses perforated by steel projectiles with various nose geometries. The method is able to predict rather accurately the modes of failure, the projectile residual velocities and ballistic limit velocities as compared with those observed in the test reported earlier except for those due to blunt projectile impact at low velocity of 170 m/s or less. This deviation in results is observed for the perforation of thin plates as the change in failure pattern is not reflected in the solution obtained from the adopted method at low impact velocity on

thin plates due to the tensile instability problem inherent in the SPH method. At lower range of impact velocities, FE solutions are in better agreement and may be adopted for this range of impact velocities. The SFM combines the strength of SPH and FEM methods while addresses their short falls of computational demand and early program termination due to severe element distortion, respectively. Though the SFM is less accurate at low velocity impact of 170 m/s and lower, the method is robust and efficient for high velocity impact penetration and/or perforation of both steel and aluminum target plates.

Chapter 5 Numerical Impact Simulations Using Modified Johnson-Cook (MJC) Model

5.1 Introduction

High velocity impact problems involve two basic phenomena – wave propagation and high strain rate. Upon collision between the projectile and target, a compression wave with intensity of $\rho c_s u_p$ (where, ρ is the density, c and u_p are the sound speed and particle velocity respectively) propagating into both projectile and target. Multiple reflections of waves at material interfaces and free surfaces create compressive and tensile stresses and eventually reach a steady state. Because of these, an intense region with extensive deformations exist within 3-6 characteristic projectile dimensions (3-6 projectile diameter for regular shape projectile) (Zukas, 1995). Within this domain, high pressure, large strain and high strain rates are observed. Depending on the loading rate and stress wave intensity, material failure occurs by various mechanisms (Backman and Goldsmith, 1978; Corbett et al., 1996; Zukas, 1990).

Any successful numerical simulation depends on two major factors: the computational method, and an appropriate material constitutive model and reasonable value of material parameters among other factors. Chapter 4 demonstrates effectiveness of the coupled SPH-FEM (SFM) when uses with the Johnson-Cook (JC) material model. However, temperature effect due to adiabatic condition is significant for high velocity perforation analysis of metal target materials and the JC model does not consider it. Moreover, the strain rate expression of the JC model can be further improved and simplified. Considering these factors, a modified Johnson-Cook (MJC)

model (Chapter 3) is adopted herein. Applications of the material model in numerical simulations are verified using two impact examples (2D axi-symmetric and 3D solid elements). Afterwards, several high velocity impact penetration/perforation simulations are performed using the MJC model as the target material model, and the residual and ballistic limit velocities are compared with the experimental results.

5.2 Verification of MJC Model

5.2.1 Split Hopkinson Pressure Bar (SHPB) Test of Titanium Alloy Ti-6Al-4V

In general the compression SHPB test system consists of an incident bar (IB), transmitter bar (TB), striker bar (SB) and the specimen (S) sandwiched between the IB and TB (Figure 5.1). After the SB impacts the IB, a compressive stress wave generates and propagates through the IB towards the IB and specimen interface. This incident compressive pulse is measured by the strain gauge 'A' positioned at the middle length of the incident bar. When this incident stress wave reaches the IB-S interface, a portion of the stress wave propagates through the specimen while the remaining portion of the compressive stress wave reflects at the interface and transmits through the incident bar as a tensile stress wave to be measured by the strain gauge 'A'. Strain gauge 'B' measures the part of compressive pulse that travels through the transmitter bar after propagating through the specimen. Reflecting waves in the specimen from the IB-S and S-TB interfaces propagate through the specimen for a few number of times and generates an approximate uniform stress condition (Davies and Hunter, 1963).

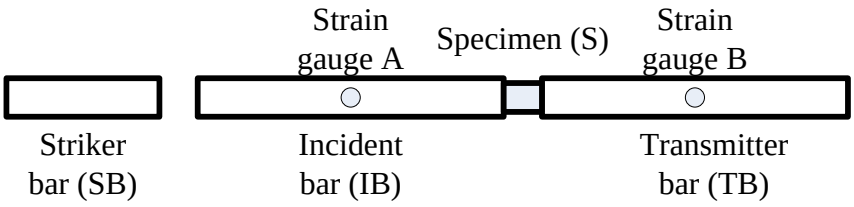

Figure 5.1 Schematic diagram of the SHPB test system.

The SHPB test theory is based on the 1-D longitudinal wave transmission along the pressure bars (Follansbee and Frantz, 1983). Figure 5.2 shows the wave propagation direction in the pressure bar, where subscripts *i*, *r* and *t* represent incident, reflected and transmitted waves. Assuming longitudinal wave propagation and uniform stress in the specimen, the displacements at the two interfaces, incident bar-specimen (*is*) and transmitter bar- specimen (*ts*) can be expressed as,

$$u_{is} = \frac{C_0}{h_s}\int \left(\varepsilon_i - \varepsilon_r\right)dt \tag{5.1}$$

$$u_{ts} = \frac{C_0}{h_s}\int \varepsilon_t dt \tag{5.2}$$

where, compression is considered as positive, C_0 is the pressure bar longitudinal wave speed, h_s is the specimen thickness, $\varepsilon_i, \varepsilon_t$ and ε_r are the incident, reflected and transmitted strains. The velocity at the two interfaces can be expressed as,

$$v_{is} = \frac{C_0}{h_s}\left(\varepsilon_i - \varepsilon_r\right) \tag{5.3}$$

$$v_{ts} = \frac{C_0}{h_s}\varepsilon_t \tag{5.4}$$

The forces at the interfaces (Figure 5.2) are written as,

$$F_{is} = A_b E_b \left(\varepsilon_i + \varepsilon_r\right) \tag{5.5}$$

$$F_{ts} = A_b E_b \varepsilon_t \tag{5.6}$$

where, A_b and E_b are the cross-sectional area and Young's modulus of the pressure bars.

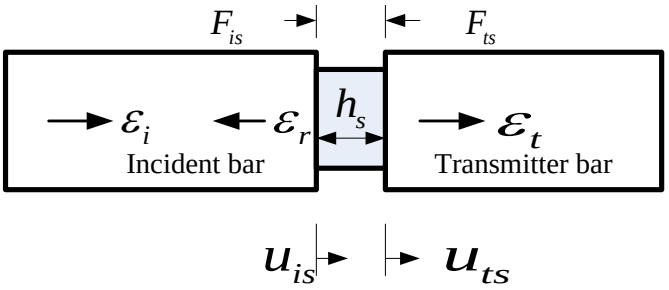

Figure 5.2 1D split-Hopkinson pressure bar analysis.

The average strain, strain rate and stress in the specimen are given as,

$$\varepsilon_s = \frac{u_{is} - u_{ts}}{h_s} = \frac{C_0}{h_s}\int \left(\varepsilon_i - \varepsilon_r - \varepsilon_t\right) dt \tag{5.7}$$

$$\dot{\varepsilon}_s = \frac{v_{is} - v_{ts}}{h_s} = \frac{C_0}{h_s}\left(\varepsilon_i - \varepsilon_r - \varepsilon_t\right) \tag{5.8}$$

$$\sigma_s = \frac{F_{is} + F_{ts}}{2A_s} = \frac{A_b E_b}{2A_s}\left(\varepsilon_i + \varepsilon_r + \varepsilon_t\right) \tag{5.9}$$

where, A_s is the cross-sectional area of the specimen. Assuming uniform deformation and force equilibrium condition in the specimen, it can be observed that force in the two interfaces are equal i.e., $F_{is} = F_{ts}$. Comparing Eqs. (5.7) and (5.8), a relationship between the strains is achieved.

$$\varepsilon_i + \varepsilon_r = \varepsilon_t \tag{5.10}$$

Substituting Eq. (5.10) into Eqs. (5.7-5.9),

$$\varepsilon_s = -\frac{2C_0}{h_s}\int \varepsilon_r dt \tag{5.11}$$

$$\dot{\varepsilon}_s = -\frac{2C_0}{h_s}\varepsilon_r \tag{5.12}$$

$$\sigma_s = \frac{A_b}{A_s} E_b \varepsilon_t \tag{5.13}$$

Stress-strain relationship of a material can be attained using the above mentioned equations. However, these expressions are not corrected for dispersion effects that may give some error and oscillation in the stress-strain curve and correction for dispersion effects should be carried out.

To verify the MJC model, in this section numerical simulations of the titanium alloy Ti-6Al-4V SHPB test (Seo et al., 2005) are performed. Specimen temperature varied from room temperature to 1000ºC. To keep the specimen strain rate constant (1400 s^{-1}), strike bar velocity (v_{sb}) varied along with the specimen temperature. The incident, transmitter and strike bars were made of 20.6 mm diameter Inconel 718. The incident and transmitter bars were 1500 mm long and the strike bar was 500 mm in length. The titanium alloy Ti-6Al-4V was cylindrical in shape with 8 mm diameter and 8 mm length.

Numerical simulations are performed using the LS-DYNA (Hallquist, 2006). The complete SHPB test with 1500 mm long incident and transmitter bars, and 500 mm long strike bar are modeled using the 2D axi-symmetric FE model as depicted in Figure 5.3. Strike bar velocities varied between 16 m/s to 21 m/s to keep the strain rate value constant at various temperatures. The specimen is placed in between the incident and transmitter bars. The mesh convergence study indicates a mesh size of 0.2 x 0.2 mm^2, for the specimen. However, at the interface between the specimen and the pressure bars, it is essential to adopt a similar element size. Because of this and to reduce the number of elements in the model a mesh size of 0.4 x 0.4 mm^2 is implemented for the 8 mm long specimen. An automatic surface to surface contact is used between the different surfaces (e.g. strike bar - incident bar, incident/transmitter bar - specimen).

The incident, transmitter and strike bar are assumed to behave like elastic material. Therefore, a simple elastic-plastic material model is adopted for the pressure

bars. Material properties of the pressure bars are given in Table 5.1. The MJC model is used for the titanium alloy Ti-6Al-4V as a user defined material model and the material properties for the model is obtained in Section 3.2.2 and shown in Table 3.1. The MJC model is unable to predict the behavior of titanium with temperature greater than beta transus temperature (996ºC). Therefore, in this study numerical simulation of SHPB test is considered only for initial specimen temperatures ranging from room temperature (25ºC) to 800ºC.

Table 5.1 Material properties for Inconel 718

σ_Y (GPa)	ρ_0 (kg/m^3)	E (GPa)	ν	E_t (GPa)
1.100	8190	204.9	0.284	1.124

Figure 5.4 illustrates the deformation of the specimen during the SHPB simulation at various time steps. As shown in the figure, the specimen is subjected to high compressive stress and the final specimen length is around 60% of the original length. Final deformed shapes of the specimen at various temperatures are shown in Figure 5.5. Simulated deformed shapes agree well with experimental results reported earlier by Seo et al. (2005). They also measured incident, reflected and transmitted strain voltages at midpoints of the incident and transmitted bars. A conversion factor is used to convert strain voltages to strain (1 volt = 500 micro-strain) in this study. Figure 5.6 compares the experimental and numerical incident, reflected and transmitted strain-time history plots of the SHPB tests at various temperatures. Simulation results show similar pattern observed in the test. Although magnitude of the strains slightly differs from the test data, it is within the acceptable range.

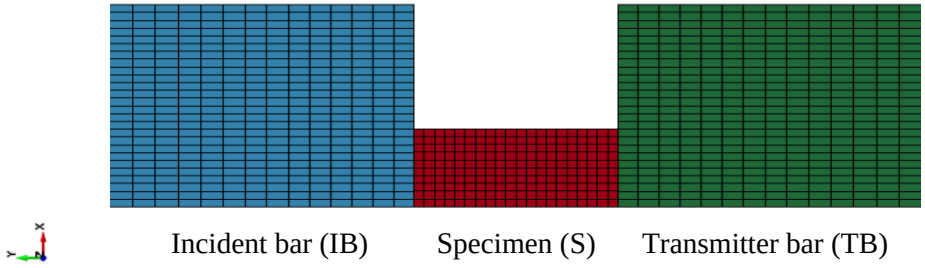

Figure 5.3 Numerical model of the Ti-6Al-4V SHPB test.

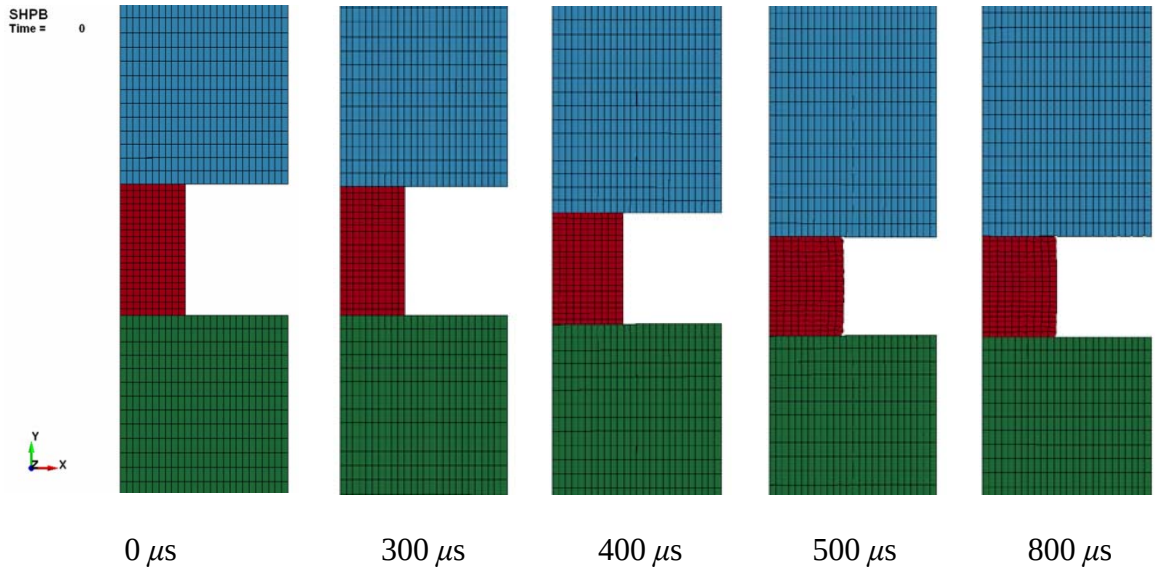

Figure 5.4 Time history plot of the SHPB test of the Ti-6Al-4V specimen at 25˚C.

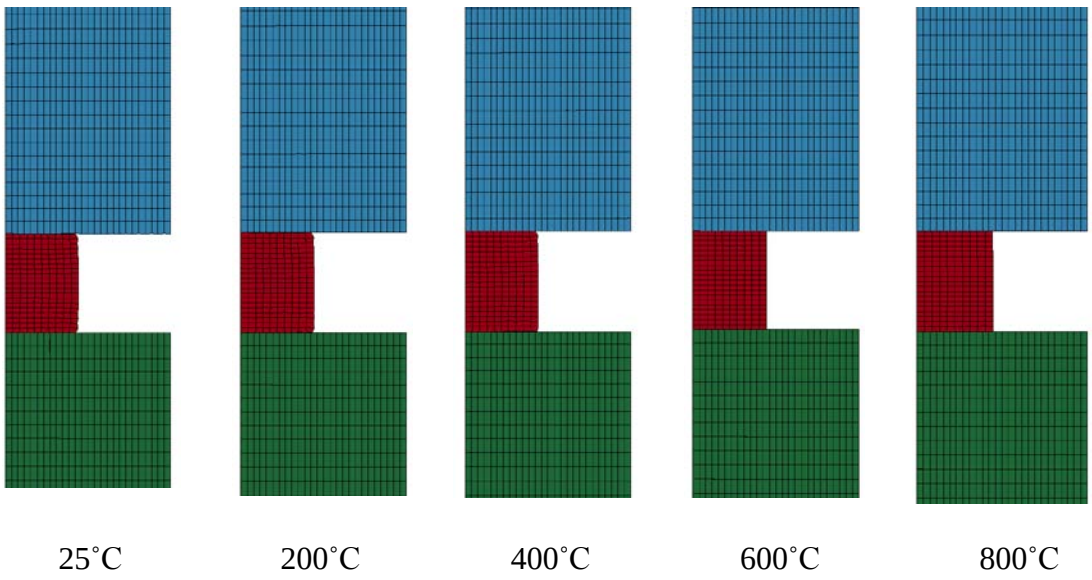

Figure 5.5 Deformed specimens at various temperatures varying from 25˚C - 800˚C.

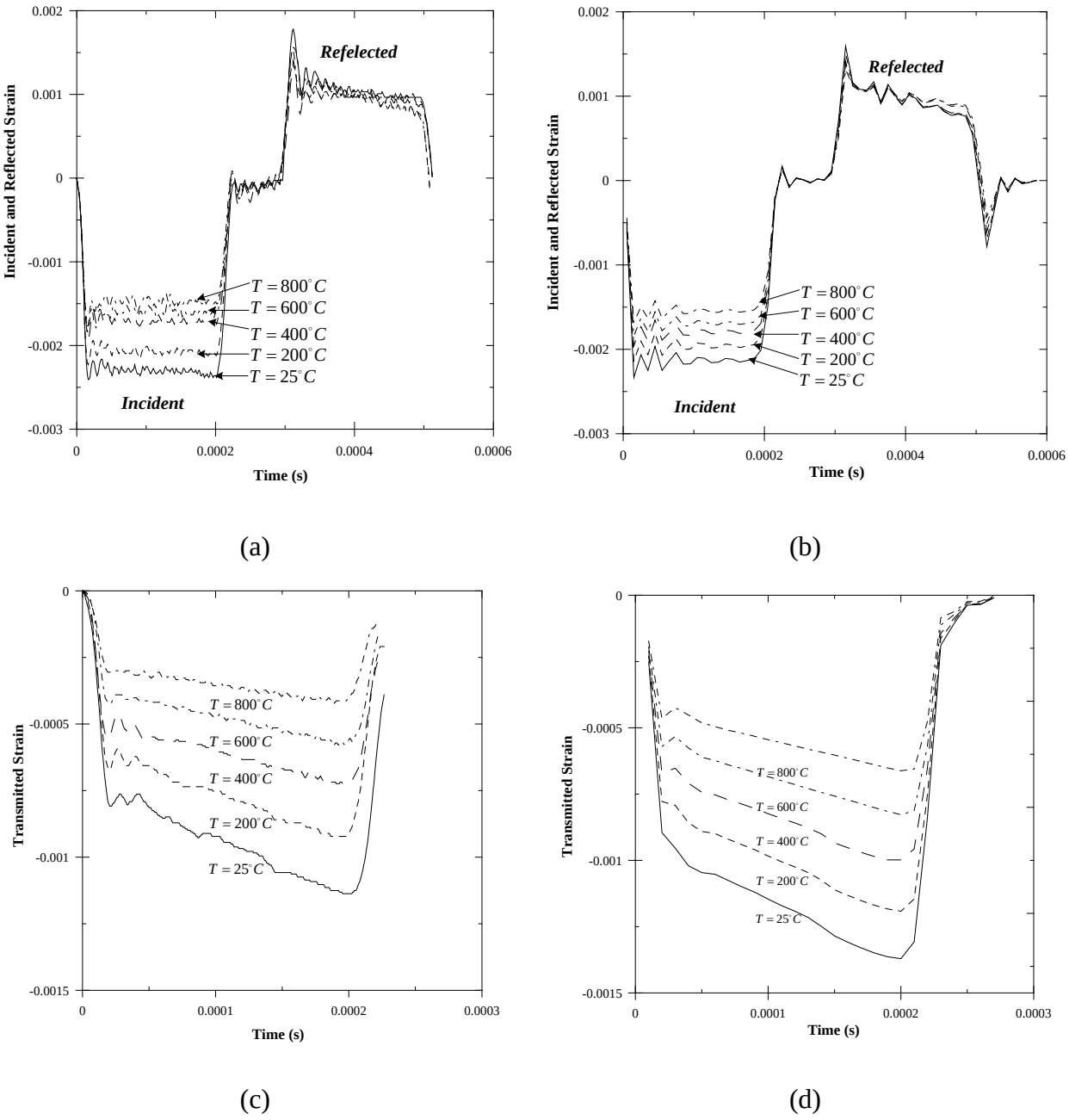

Figure 5.6 Incident, reflected and transmitted strain wave-time histories of the experimental (a, c) and numerical (b, d) SHPB tests of the titanium alloy Ti-6Al-4V.

5.2.2 Perforation of Weldox 460 E Steel Plate

To verify further the model performance, steel plate impact simulation is conducted and compared with the test results. Børvik et al. (2003) performed the perforation test of 6 mm thick Weldox 460 E steel plate by Arne tool steel blunt projectile. Blunt projectile has length and diameter of 80 mm and 20 mm respectively. Steel target plate has a clear span diameter of 500 mm. During the penetration,

damages in the projectile were not significant, and hence, a simple elastic/plastic material model is used for the projectile. The material properties of the hardened Arne tool steel projectile are listed in Table 5.2.

Table 5.2 Material properties for hardened Arne tool-steel (Dey, 2004)

σ_Y (GPa)	ρ_0 (kg/m^3)	E (GPa)	v	E_t (GPa)	$\left(\varepsilon_f\right)_{mean}$ (%)
1.9	7850	204	.33	15	2.15

Finite element method (FEM) is used for the impact simulation. Both target and projectile are modeled using the 3D solid 8 nodes elements. Based on the mesh sensitivity study, element size of 0.2 x 0.2 x 0.2 mm^3 is chosen for the target plane in the impact vicinity and the mesh is gradually coarser towards the outer edge. Only 1/24 of the problem is modeled using two planes of symmetry. Target plate is fixed at the outer boundary. Surface to surface contact is used in between the projectile and the target plate. To avoid the severe element distortion problem in FEM, the damage based element erosion method is used for the target plates.

The proposed MJC model is used for the Weldox 460 E steel target plate and adopted as a user-defined material model in LS-DYNA. The identification procedure of the MJC model parameters is described in Section 3.2.2.2. All the material properties for Weldox 460 E steel are summarized in Table 5.3.

Table 5.3 MJC Material properties for Weldox 460 E steel

ρ_0 (kg/m^3)	E (GPa)	v	G (GPa)	A (MPa)	B (MPa)
7850	200	0.33	75.2	503	581
A	C	b	C_p (J/kgK)	T_m (K)	T_r (K)
0.481	0.01	0.94	452	1800	293

The projectile hits the target at the tested initial velocity of 296 m/s. The residual projectile velocity in the numerical simulation is found to be 271.2 m/s which is close to the test data of 260.2 m/s. Figure 5.7, demonstrates the perforation of 6 mm thick plate by a blunt projectile. In the experiment, the target failed by adiabatic shear failure around the periphery of the projectile. As observed from the figure, the proposed model is able to produce similar behavior of the perforation process. Figure 5.8 describes the numerical adiabatic shear failure more closely.

Because of the element erosion option, highly deformed elements are removed, and hence, a crack develops and propagates towards the rear surface. Once the crack reaches the rear surface, a plug is formed and the projectile progress without any significant resistance. Although the numerical simulation shows a good agreement with the experimental observation, the element erosion method should be used carefully. The loss of energy and mass due to element erosion is negligible in this case. However, for thicker plate with high initial projectile velocity it would be significant. Therefore, the FEM may not be a better option for thick plate penetration/perforation.

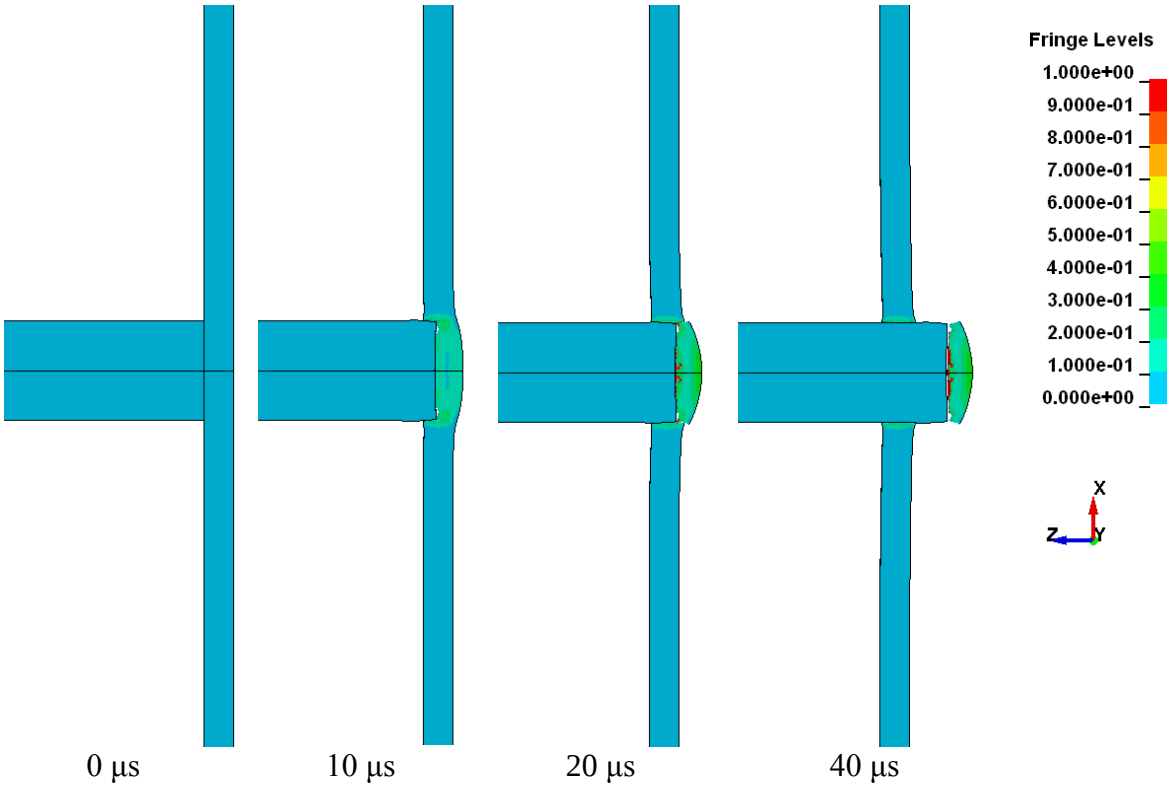

Figure 5.7 Time history plot of the perforation process of 6 mm thick Weldox 460 E steel plate with effective plastic strain contour.

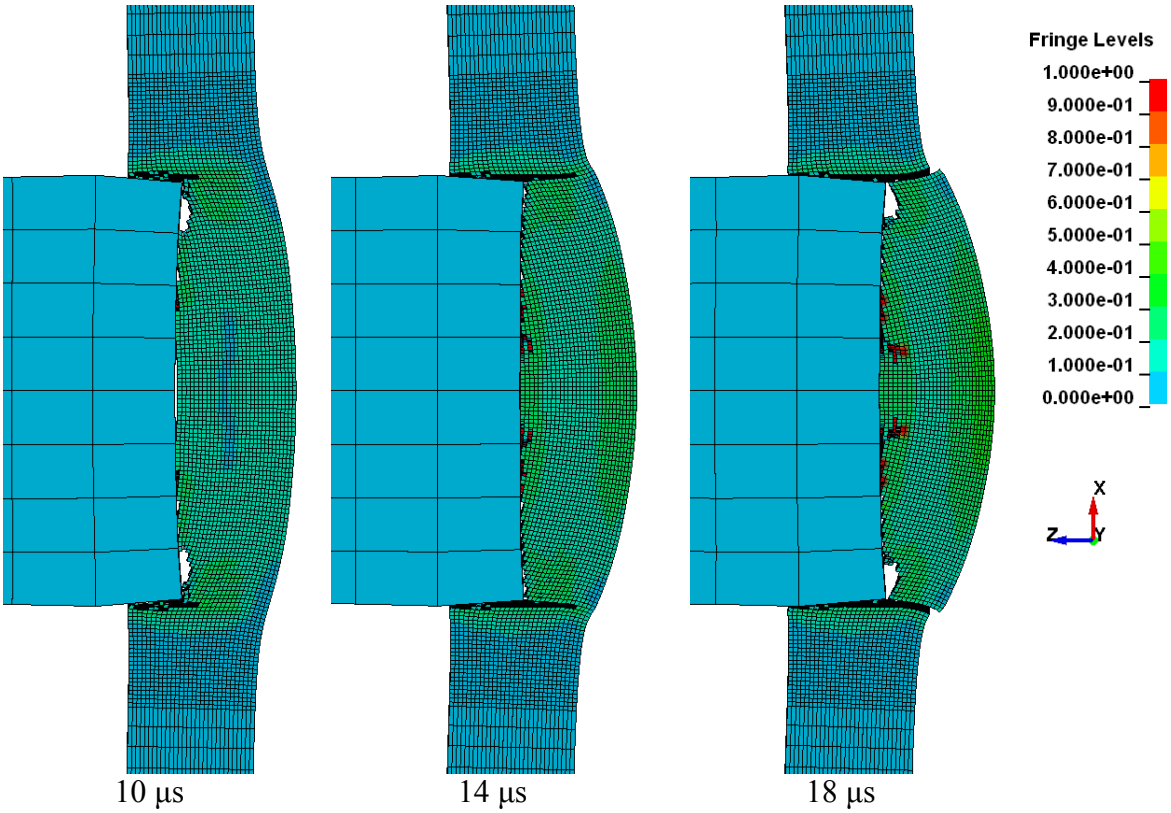

Figure 5.8 Adiabatic shear failure of 6 mm thick Weldox 460 E steel plate.

5.3 Perforation of Ti-6Al-4V Alloy Plate Using MJC Model

Burkins et al. (2001) published ballistic test results of 26.7 mm thick titanium alloy Ti-6Al-4V target plate. The fragment-simulating projectile (FSP) with 20 mm diameter was used as the projectile. Geometry and dimensions of the FSP are demonstrated in Figure 5.9. Several penetration and/or perforation studies were conducted with impact velocities ranging between 950 – 1060 m/s. The experimental ballistic limit velocity of the 26.7 mm plate is 1023 m/s with a standard deviation of 13 m/s. The present study involves the SFM simulation of the perforation of Ti-6Al-4V plate using the MJC model for the target material.

5.3.1 Material Properties of Titanium Alloy Ti-6Al-4V

Target plates are made of titanium alloy Ti-6Al-4V with aerospace specification MIL-T-9046J, and have yield and ultimate tensile strengths of 875.6 MPa and 972.2 MPa respectively with 15% of elongation (Burkins et al., 2001). Based on these mechanical properties, strength material parameters (*A*, *B* and *a*) for the MJC model are determined first. Material strength parameters depend on the loading rate of the tensile test. However, lack of strain rate information from the tensile tests makes it difficult to predict strength parameters accurately. Therefore, it is necessary to establish a strain rate value using a calibration approach. Quasi-static tensile tests of specimens can be performed using a MTS servo hydraulic testing machine at strain rates between $10^{-5} - 10^{2}\ \mathrm{s}^{-1}$. Therefore, three strain rate cases, such as low, moderate and high strain rates (AL = $10^{-4}\ \mathrm{s}^{-1}$, AM = $1\ \mathrm{s}^{-1}$ and AU = $10^{2}\ \mathrm{s}^{-1}$) are considered to determine the strength parameters. Least square method is applied to determine the parameters, and indeed, Table 5.4 gives all the parameters for various cases. As observed in the Table 5.4, strength parameters vary with the choice of strain rate case. For the same material strength, material tested at low strain rate will give

higher strength parameters and vice versa. This is due to the fact that strength parameters are determined for strain rate value of $1\,s^{-1}$, and will give higher values if yield strength in the experiment is determined for strain rate value less than $1\,s^{-1}$ and vice versa. Other material parameters are believed to be similar to the commercial Ti-6Al-4V and are already determined in Section 3.2.2. Table 5.5 summarizes other material properties for the MJC model.

Table 5.4 MJC Strength material parameters for titanium alloy Ti-6Al-4V plate

Case	AL	AM	AU
A (MPa)	976.0	863.0	811.0
B (MPa)	447.0	396.0	376.0
a	0.686	0.686	0.686

Table 5.5 MJC Material properties for titanium alloy Ti-6Al-4V plate

ρ_0 (kg/m^3)	*E* (GPa)	*v*	*G* (GPa)	*C*	*b*	C_p (J/kgK)	T_{melt} (K)	T_{room} (K)
4430	99.2	0.33	37.3	0.0133	0.80	560	1877	296

5.3.2 Ballistic Numerical Simulation Using Coupled SPH-FEM (SFM)

In the experiment, multiple perforation tests were performed with a single 305 x 457 x 26.7 mm^3 target plate. However, in the simulation only one impact test is conducted at the middle of the target plate. The target plates and projectiles are modeled using the SFM and FEM respectively. Figure 5.10 describes the numerical model of the projectile and target plate. Selection of SPH domain size is important for the SFM. Earlier studies has showed the effect of SPH domain radius (Section 4.2.1) and an optimum SPH domain radius of two to three times the projectile radius has been decided upon. However, in this case because of the high impact velocity and non-regular projectile shape, the area of the exit surface bulge is larger than those of

the earlier studies. Therefore, SPH particles are utilized at the middle of the target plate with a larger SPH domain radius of 30 mm in order to limit the exit surface bulge within the SPH domain. Earlier studies (Section 4.2.2) also included initial SPH particle distance effect study for steel and aluminum plates and a particle distance of 0.6 mm has been selected. The initial SPH particle distance of 0.8 mm is used for Ti-6Al-4V plate perforation since the particle distance of 0.6 mm has shown some unexplained instability during the simulations. For the FEM, 8 node solid elements are adopted. Only a quarter of the problem is modeled using symmetry in *xz* and *yz* planes. The projectile is made of 4340H steel and the material properties are given in Table 5.6. The projectile is modeled using an elastic/plastic material model with isotropic hardening. In the simulation, the projectile impact velocities varied between 1000 – 1300 m/s. Ti-6Al-4V titanium alloy has high strength but relatively low thermal conductivity. Because of these characteristics, during the high velocity penetration event target material melt (Woodward, 1979) at the projectile-target interface, which significantly reduces the frictional effect between the projectile and target. Therefore, no friction is included for Ti-6Al-4V perforation.

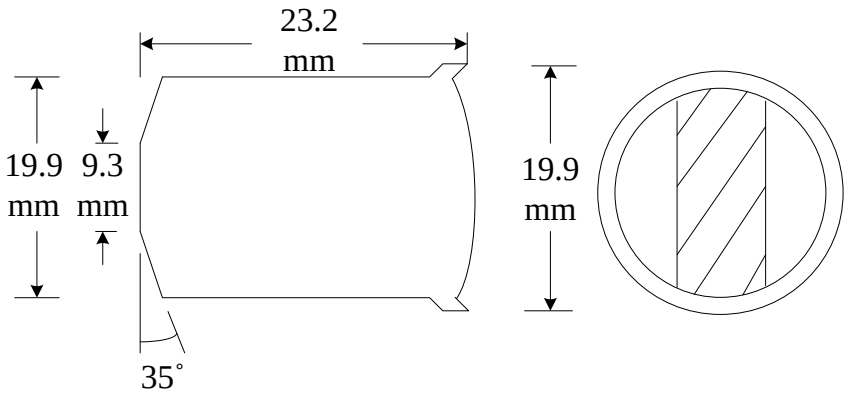

Figure 5.9 Geometry and dimension of the 20 mm fragment-simulating projectile (FSP).

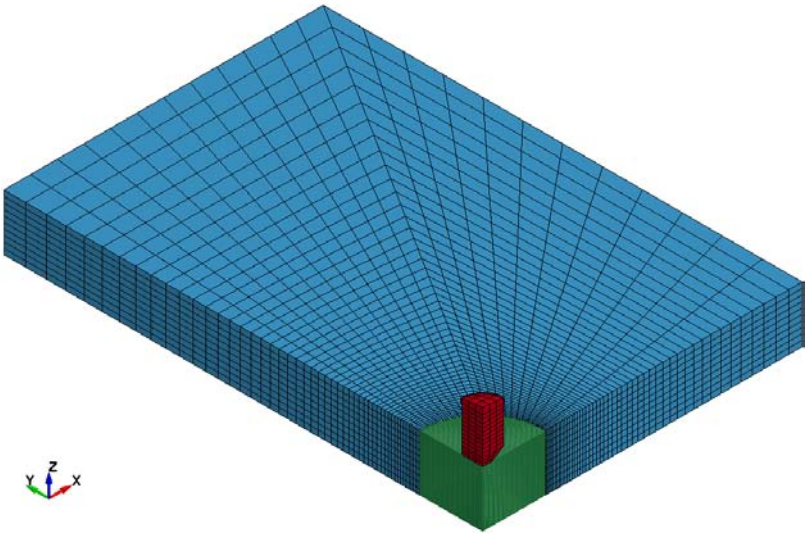

Figure 5.10 Target and FSP projectile numerical model for Ti-6Al-4V titanium alloy plate perforation.

Table 5.6 Material properties for 4340H steel

σ_Y (MPa)	ρ_0 (kg/m^3)	E (GPa)	N
435	7850	205	.29

5.3.3 Residual Velocity Comparison

Residual velocities for three cases are measured from the numerical simulation and plotted in Figure 5.11 along with the experimental data. The numerical initial and residual velocities are plotted using an analytical model originally developed by Recht and Ipson (1963).

$$v_r = o\left(v_i^q - v_{bl}^q\right)^{1/q} \qquad 5.14$$

where, v_i, v_r and v_{bl} are initial, residual and ballistic limit velocities respectively, o and q are the model constants which can be determined using the least square method. The numerical ballistic limit velocities for AL, AM and AU cases are 1124.0, 1053.5 and 1018.5 m/s respectively. The model constants o and q are calculated with v_i, v_r and v_{bl}, and are found to be 0.5 and 2 respectively for all three cases.

Low strain rate case, AL underestimates the residual velocities and overestimates the ballistic limit velocity compared to the experimental results. Although AU case seems to show better agreement with the experimental observation, it is difficult to achieve strain rate of $10^2\ s^{-1}$ in a MTS servo hydraulic machine. On the other hand, moderate strain rate case, AM provides most rational material properties, and the ballistic limit velocity of 1053.5 m/s correlates well with the experimental ballistic limit velocity of 1023 m/s.

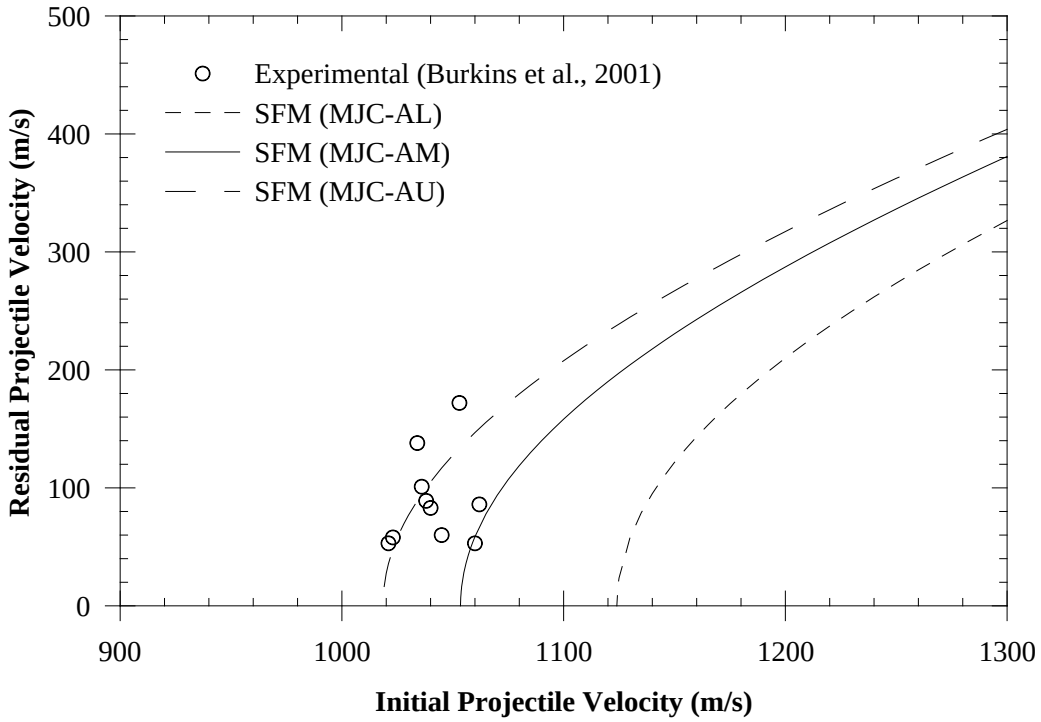

Figure 5.11 Numerical and experimental residual velocities of the FSP perforating Ti-6Al-4V plates.

The FSP geometry is different from those of other projectiles discussed earlier including projectiles with blunt, ogival and conical noses. Therefore, failure patterns of the target plates due to the former are different, as expected from those of the latter. A combination of failure patterns such as, ductile hole enlargement, adiabatic shear band and fractures due to bending is observed in Ti-6Al-4V perforation simulations. Figure 5.12 demonstrates the perforation process of the FSP with 1060 m/s initial impact velocity. Due to the blunt tip of the projectile, a sharp indentation is observed

initially with significant projectile deformation. At this stage, failure occurs within a narrow localized zone due to shear bands around the projectile periphery. The next step shows a change in the projectile nose to that of a hemispherical shape and the projectile progresses through the target plate by moving the materials in radial direction. The target plate is subjected to bulging and thinning at the rear surface which causes intensive tensile strain zone. Fracture appears when tensile strain exceeds material capacity and petals are formed. Separation of petals is also observed and because of that a larger exit crater than the entry crater is detected.

5.4 Steel Plate Perforation Simulation

Steel plate impact simulations are conducted using the SFM and MJC model for target plates. Two cases are chosen for steel plate perforation, one to perforate steel plates of varying thicknesses (6 – 20 mm) by steel blunt projectiles, and one to perforate 12 mm thick steel plates by steel projectiles with various nose shapes (blunt, conical and ogival). Cylindrical projectiles have a diameter and mass of 20 mm and 197 gm respectively, and are made from Arne tool steel (Børvik et al., 2003). Blunt projectile has a length of 80 mm, however, the length of conical and ogival nose projectiles vary slightly to keep the projectile mass a constant (Dey, 2004). Details of the projectiles are shown in Figure 4.1 in Chapter 4. Steel target plates with clear span diameter of 500 mm are prepared from Weldox 460 E steel plates. Impact velocities of the projectile varied between 100 – 400 m/s.

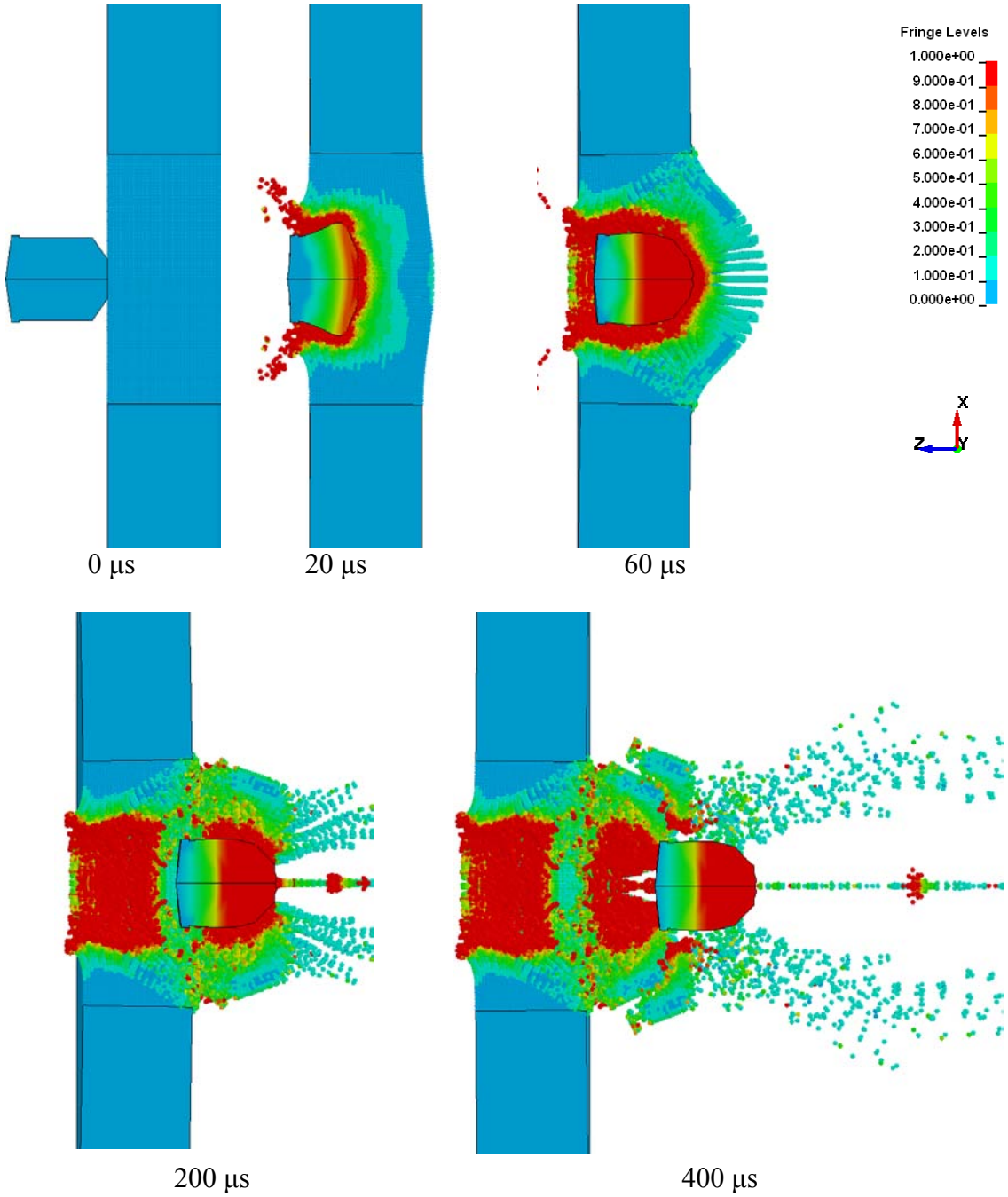

Figure 5.12 Time history of 26.7 mm thick Ti-6Al-4V plate perforated by FSP at v_i = 1060 m/s with effective plastic strain fringe contour.

The SFM is used for modeling the target plate with the SPH particles at the highly distorted area and the FEM at the relatively unaffected area. The projectile is modeled using the FE – 8 node solid element. The choice of the SPH domain size for steel target plate is studied in Section 4.2.1 and the SPH domain radius of 24 mm is adopted in subsequent study for 20 mm diameter projectile. The effect of SPH particle

distance is important for impact simulation, especially for target plates with adiabatic shear failures (Dey, 2004). The effect of particle distance is performed in Section 4.2.2 and the SPH particle distance of 0.6 mm is selected for the following simulations. Blunt projectile penetrates the target plate through adiabatic shear failure with minimum surface contact between the projectile and the target. Therefore, no friction is considered for the blunt projectile perforation. However, sharp projectiles like conical and ogival nose projectiles, penetrate the target by pushing the materials in front of the projectile inducing significant contact between the projectile and the target, and hence a friction coefficient value of $\mu_f = 0.08$ (Section 4.2.3) is adopted for conical and ogival nose projectile perforations. Details of the numerical simulation procedures are given in Section 4.2. A simple elastic-plastic material model with isotropic hardening is adopted for the projectile and the material properties are listed in Table 5.2.

The MJC model is used for the Weldox 460 E steel target plates. The identification procedure of the MJC material parameters for the target plates is described in Section 3.2.2.2. All the material properties are summarized in Table 5.3.

5.4.1 Comparison of Residual and Ballistic Limit Velocities

Impact simulations of blunt projectile against steel plates with thicknesses between 6 – 20 mm are conducted using the SFM for the target. The MJC model for the target material is used through the user defined material model. Residual velocity of the projectile is measured when it reaches a steady state after perforating the target. Figure 5.13 exhibits the relationship between the residual and initial velocities for various plate thicknesses. Numerical results using the MJC model are designated as SFM (MJC). For comparison purpose, numerical results using the JC model for the target material are designated as SFM (JC), are also included in Figure 5.13. SFM

(MJC) results show a better agreement with the experimental observations, especially for thin plates as compared to SFM (JC).

In perforation study of steel plate by blunt projectile, plugging failure due to adiabatic shear appears to be most significant failure mode for the target plate. After initial impact, the target undergoes localized deformation in a narrow zone around the periphery of the projectile under adiabatic condition. Shear bands develop in this zone because of the coalescence of damage and heat generation. Cracks develop at critical strain and progress towards the other side of the target plate. Finally, separation of plug from the target plate occurs by combination of shear and fracture stresses (Børvik et al., 2003) and the plug moves in the direction of projectile. Figure 5.14 illustrates the failure patterns of the 10 mm target plate when impacted by a blunt projectile at 180 m/s. Formation and growth of shear bands and cracks, development of plug and eventual separation of plug due to shear and fracture stresses at the rear surface are perfectly described by the numerical simulation. All the target plates fail by plugging failure. Figure 5.15 shows the progress of the projectile when perforating 6 and 10 mm thick target plates with impact velocities of 160 and 180 m/s respectively. Following Figure 5.15, it is noted that the thin plates of 6 mm thick show much more global deformation as compared to the thick plates of 10 mm thickness with more local deformation in the latter. The same trend is also observed in the experimental investigation reported by Børvik, et al. (2003).

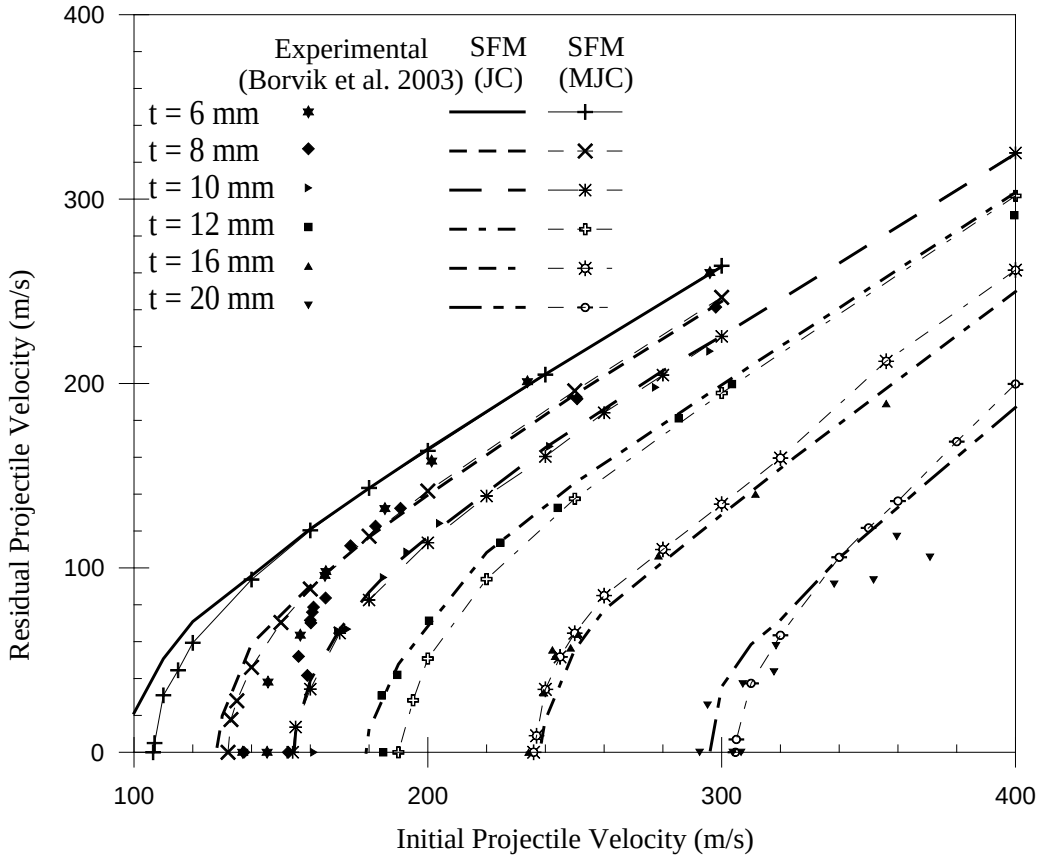

Figure 5.13 Experimental and SFM residual velocities for blunt projectile perforating steel plates.

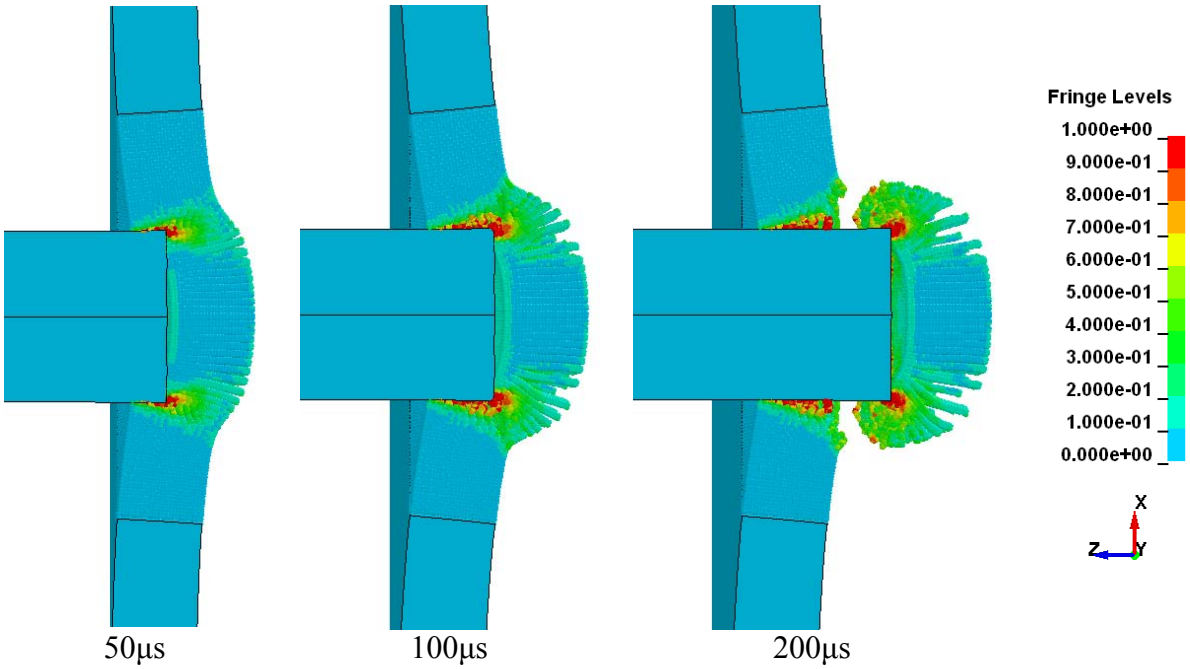

Figure 5.14 Adiabatic shear failure process in a 10 mm thick plate with v_i = 180 m/s.

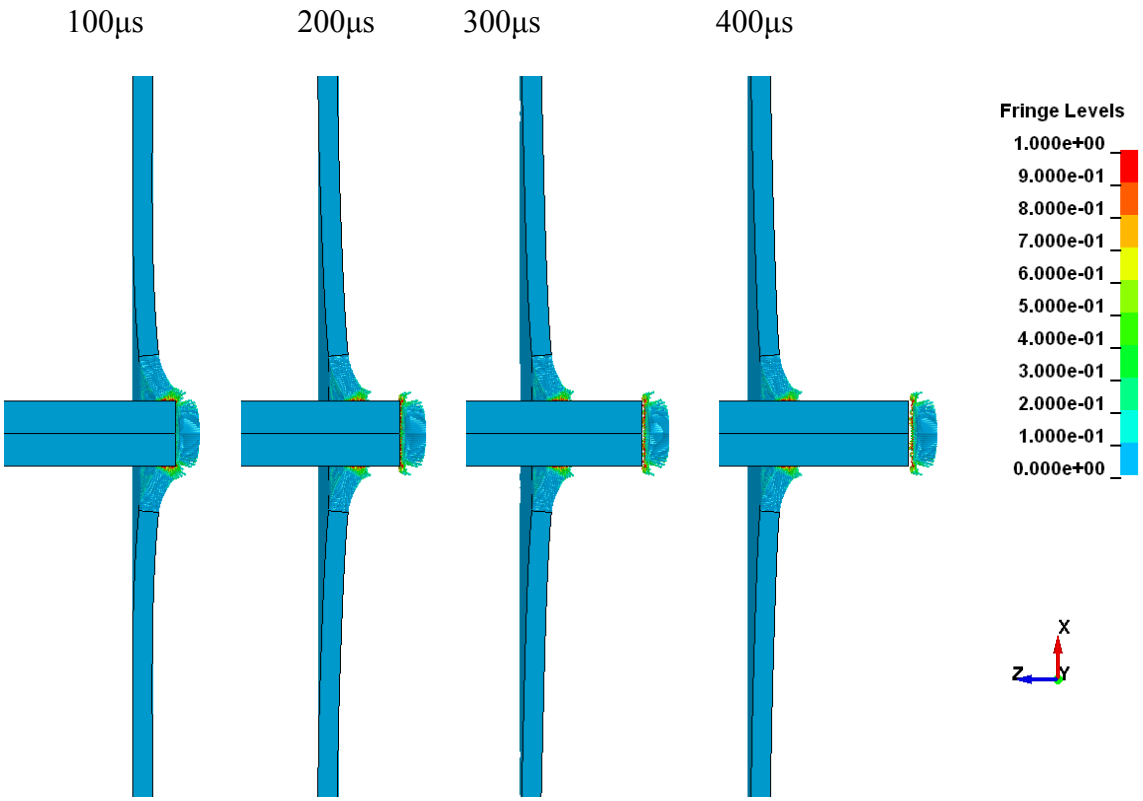

(a)

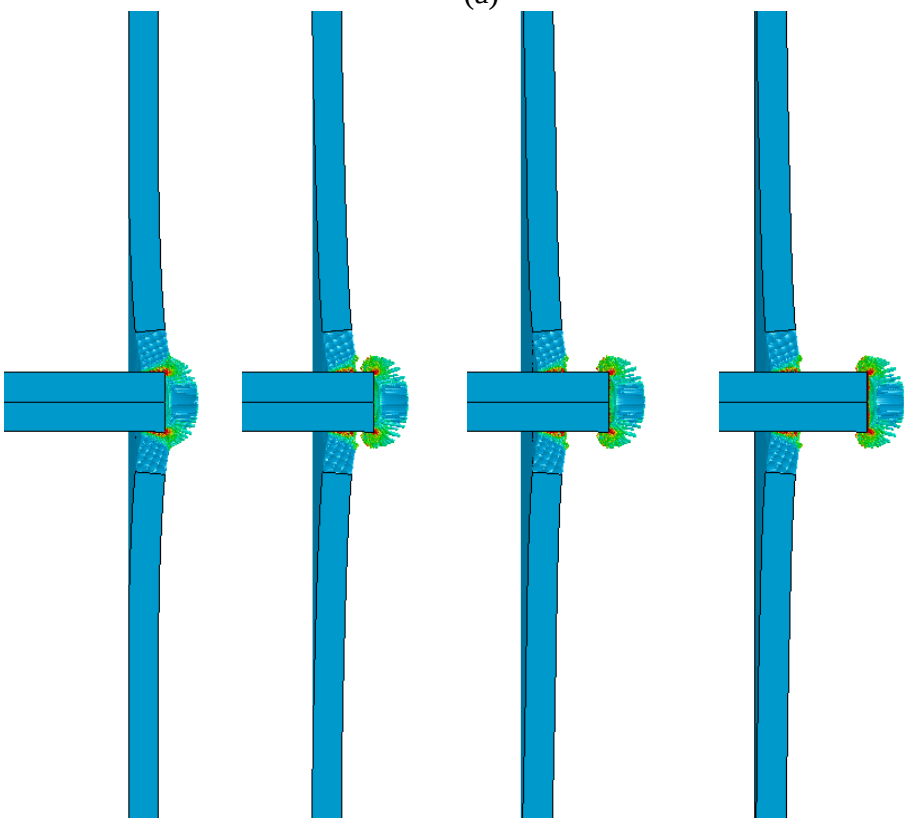

(b)

Figure 5.15 Progress of the projectile with (a) v_i = 160 m/s into a 6 mm thick plate; (b) v_i = 180 m/s into a 10 mm thick plate.

Ballistic limit velocities for all plate thicknesses are evaluated and demonstrated in Figure 5.16 that also contains numerical results from section 4.2.4 along with the experimental data. The SFM (MJC) results show a good agreement with the experimental data except for plate thicknesses of 6 and 8 mm. Although the SFM (MJC) is unable to simulate the change in failure patterns from global dishing and plugging for thin plates to adiabatic shear and plugging for thick plates, it predicts more accurate results than those of SFM (JC). Cross section of various target plate thicknesses after perforation at strike velocities close to the ballistic limit velocities are illustrated in Figure 5.17. Similar to the experimental observations illustrated in Figure 5.18, the global deformation decreases with increasing plate thicknesses. However, rear side bulging of the target plates are absent in the simulations. This is because of the prominent shear fracture than the adiabatic shear failure at the rear surface in the simulation.

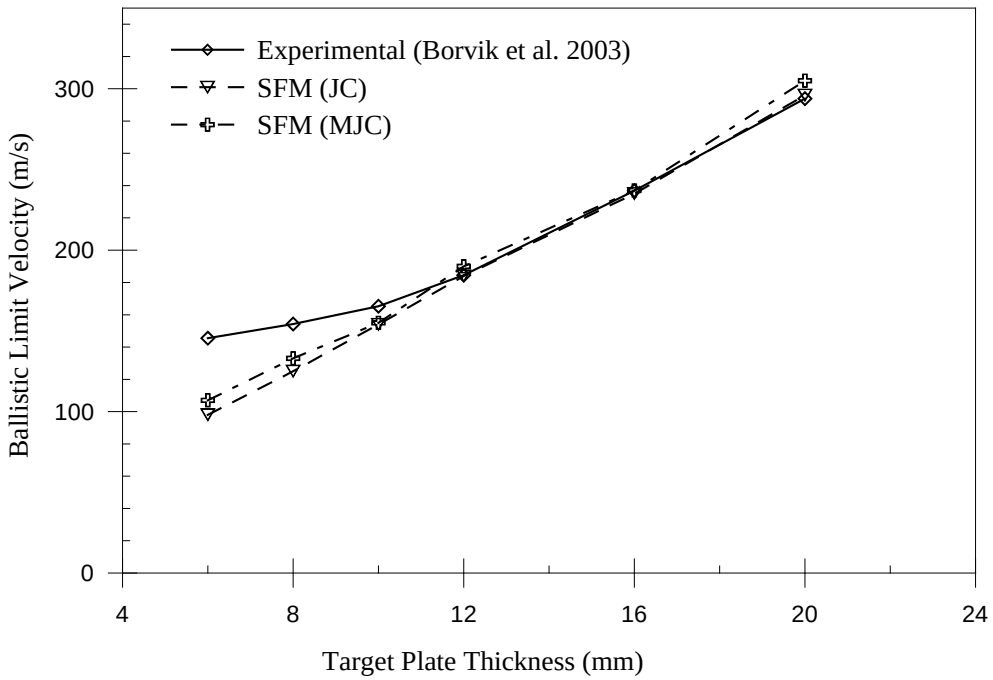

Figure 5.16 Experimental and numerical ballistic limit velocities for steel plates.

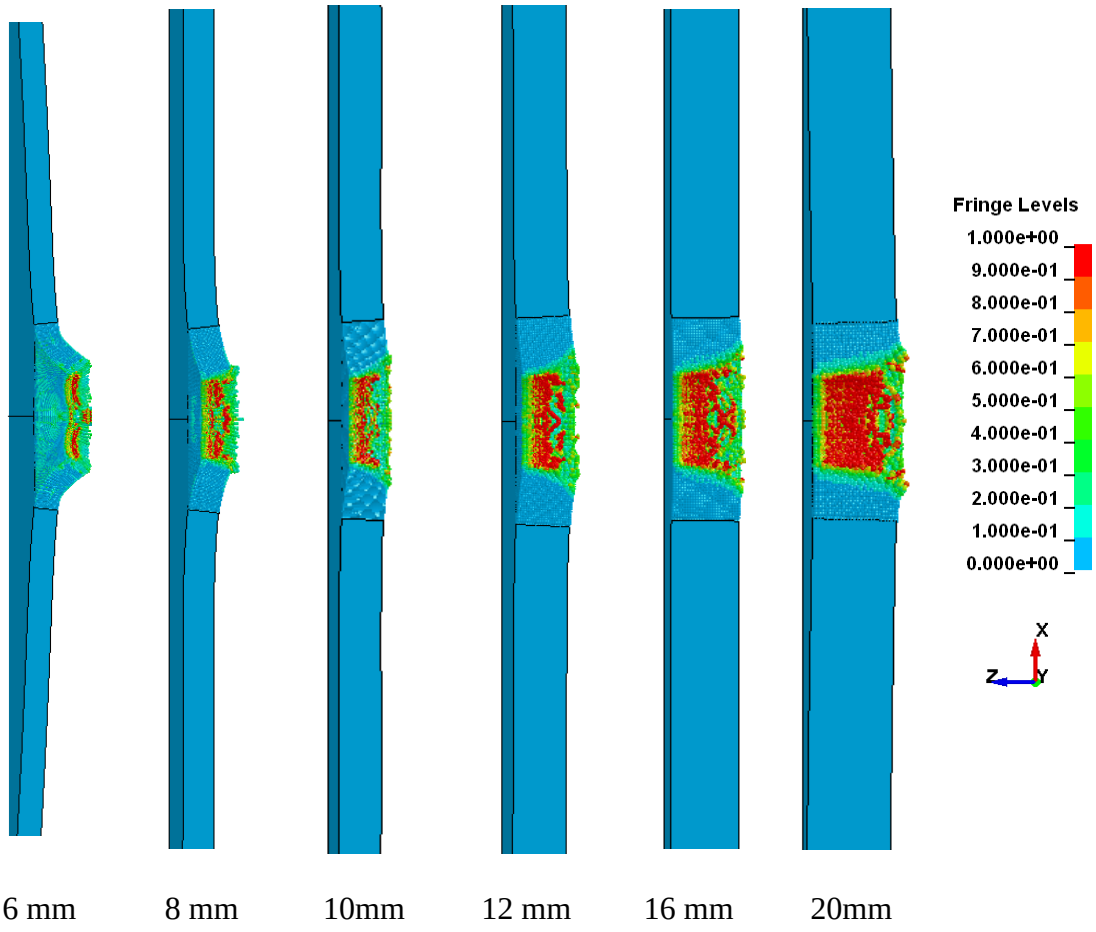

Figure 5.17 Cross sections of the perforated target plates at strike velocities (110, 135, 160, 195, 240 and 310 m/s respectively).

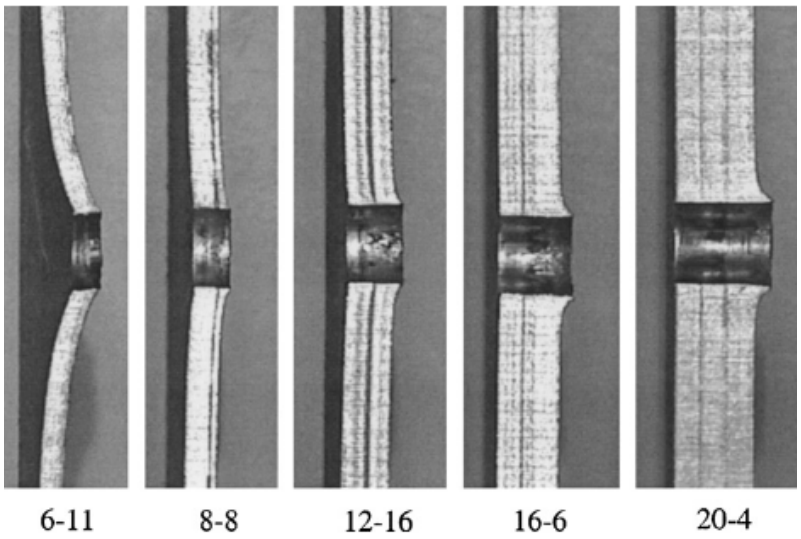

Figure 5.18 Cross sections of the perforated target plates at strike velocities (156.6, 173.7, 189.6, 242.4 and 307.2 m/s respectively) (after (Børvik et al., 2003)).

Effect of the projectile nose geometries on the Weldox 460 E steel target plate is also studied using the SFM (MJC). A 12 mm thick steel plate is impacted by projectiles with three different nose geometries (blunt, conical and ogival). Residual velocities of the projectile with maximum initial impact velocity up to 400 m/s are measured and compared with the experimental data (Dey, 2004). The SFM (MJC) simulation results give a very good prediction of the experimental data as shown in Figure 5.19. The figure also incorporates the SFM (JC) results in order to compare them with the SFM (MJC) data. Both models show identical behavior except for the blunt nose projectile.

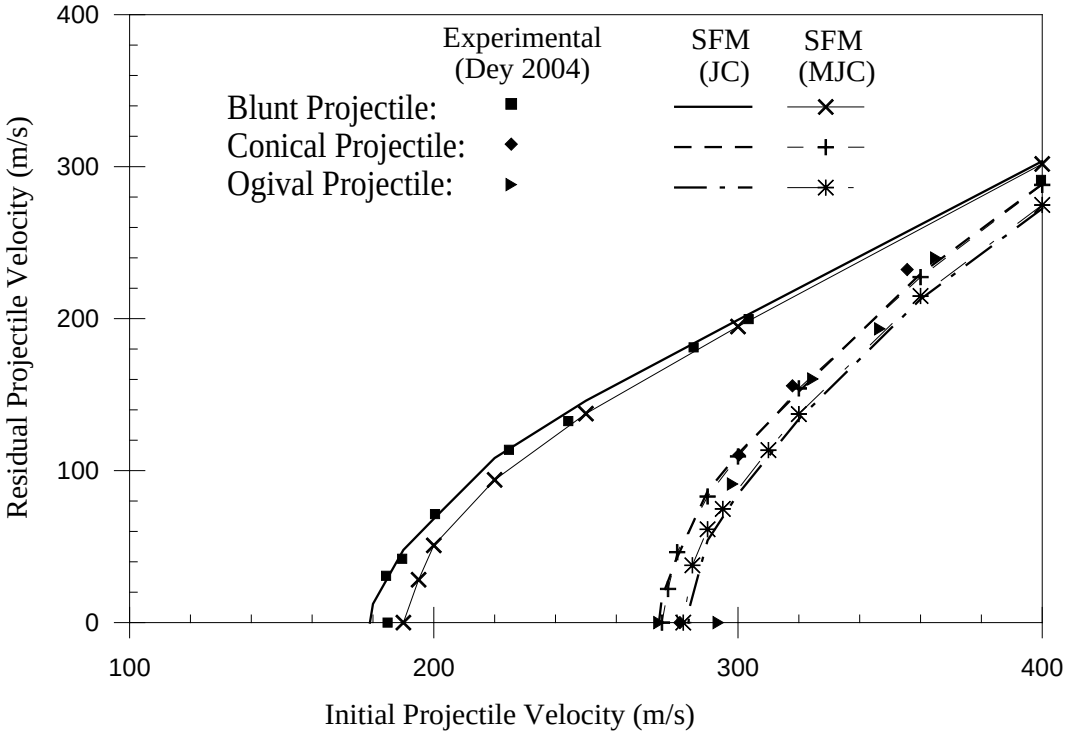

Figure 5.19 Comparison of experimental and numerical residual velocities for various nose projectiles.

5.5 Aluminum Plate Perforation by Conical Nose Projectile

Perforation of aluminum alloy AA5083-H116 plates by conical nose steel projectiles have been performed using the MJC model as target material model. All the simulation conditions are similar to the previous study mentioned in Section 4.3 except for the material model for the target.

5.5.1 Aluminum Alloy Material Properties

Aluminum-Magnesium (Al-Mg) alloys (AA5XXX class aluminum alloys) show negative strain rate effect, i.e. decrease in strength with increasing strain rate under certain conditions (temperature and strain rate). This behavior is the result of dynamic strain aging (Abbadi et al., 2002; Naka and Yoshida, 1999; Wagenhofer et al., 1999). At room temperature and low strain rates, magnesium in Al-Mg alloys diffuses and prevents dislocation that causes dynamic strain aging. However, at high strain rates, the dislocation process is too fast to be locked by any magnesium diffusion. Dynamic strain aging is limited to strain rates ranging from $10^{-4} \sim 1\,s^{-1}$ at room temperature (Clausen et al., 2004; Naka and Yoshida, 1999). Both the JC and MJC models are unable to consider the negative strain rate effects. However, high velocity impact problems are subjected to high strain rates (generally higher than 1 s^{-1}) and temperatures, hence, it is justifiable to use the MJC model for aluminum alloy AA5083-H116. For strain rate effect calculation, only strain rates higher than 1 s^{-1} are considered.

The MJC model is used for the numerical simulations of aluminum alloy AA5083-H116 plate perforation. Material parameters of AA5083-H116 are determined from the tensile tests conducted by Clausen et al. (2004) and Børvik et al. (2009) on smooth specimen at wide range of strain rates and temperatures. Detail calculation procedures of the material parameters are described in Chapter 3. Material strength properties (*A*, *B* and *a*) of AA5083-H116 vary with plate thicknesses due to the difference in the manufacturing process (Section 4.3), and hence, they are obtained from the quasi-static tests at room temperature (Børvik et al., 2009) for each plate (15, 20, 25 and 30 mm) using the least square method as shown in Figure 5.20.

The strength parameters for the 20 mm and 30 mm thick plates show similar stress – strain relationships, and the same material parameters are adopted for both cases.

It is assumed that the plate thickness does not influence strain rate and temperature effects and values for these two parameters are evaluated from the 25 mm thick plate test results. Strain rate parameter (*C*) is obtained next from test results at strain rates of 3.95, 122 and 1313 s^{-1}. Figure 5.21(a) illustrates the variation of *C* value with plastic strain value varying from 0.05 to 0.11. It also shows the average value of *C*. It should be noted that this value is only applicable for conditions where strain rate is larger than $1\,s^{-1}$. Temperature effect parameter is determined from the specimen test at temperatures between 200 - 500˚C. As shown in the Figure 5.21(b), the parameter *b* decreases with increasing plastic strain for temperatures 200˚C and 300˚C, but it predicts a constant value for temperatures 400˚C and 500˚C. Lack of enough experimental data makes it difficult to determine the relationship between *b* and plastic strain. Therefore, an average constant value of *b* is selected. Three average values from temperatures 200˚C and 300˚C, 400˚C and 500˚C, and all the four temperatures are measured as 0.77, 0.34 and 0.56. Perforation simulations of 15 mm thick plates are conducted using three *b* values, and the numerical residual velocities are compared with the test data (Figure 5.22). Following the figure, b value of 0.56 gives a good prediction of the experimental observations. Since, the temperature at the projectile and target interface varies from room to melting temperature; it makes sense to take the average from all temperatures. The MJC model properties are listed in Table 5.7.

Table 5.7 MJC Material properties for AA5083-H116 aluminum plate

ρ_0 (kg/m^3)	E (GPa)	ν	G (GPa)	C	b	C_p (J/kgK)	T_{melt} (K)	T_{room} (K)
2700	70.0	0.3	27.0	0.0114	0.56	910	893	293

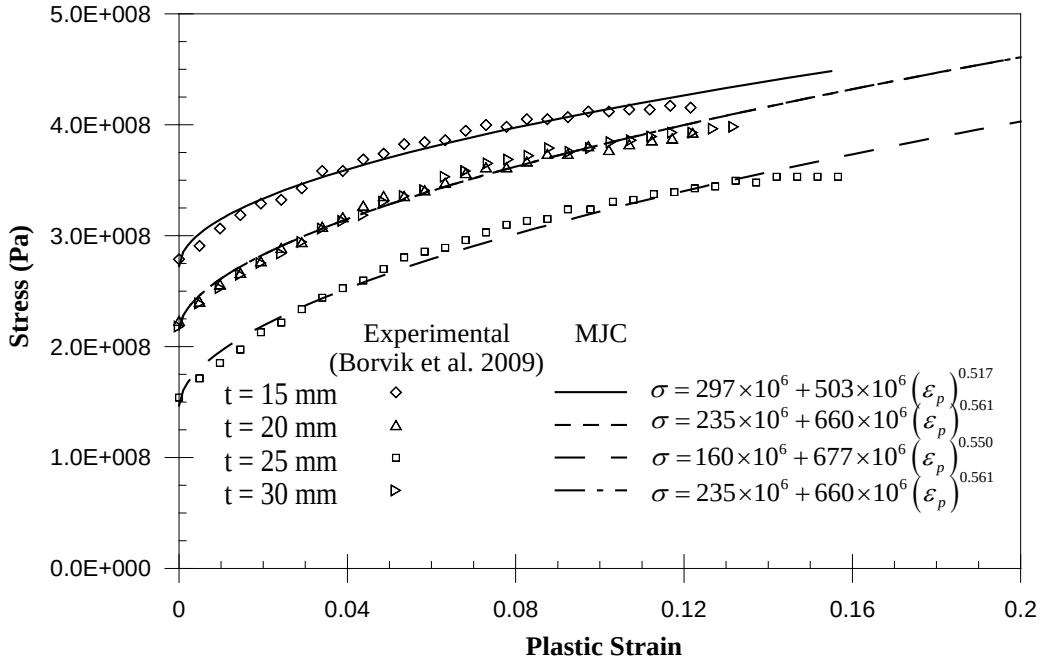

Figure 5.20 Comparison of the experimental and MJC model (with material properties) prediction for various plate thicknesses.

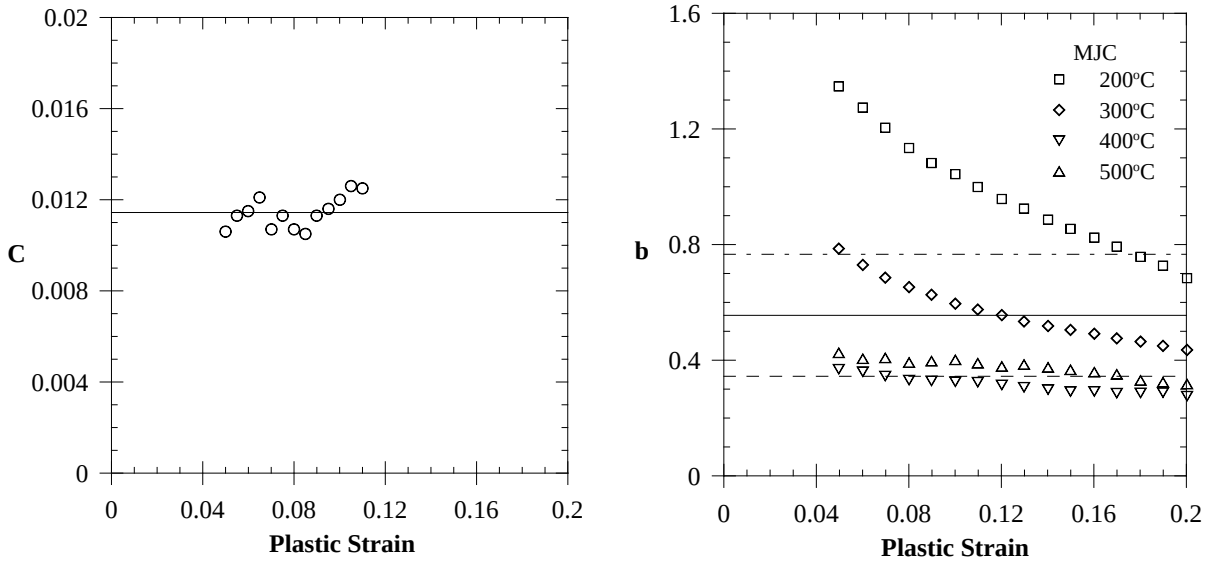

(a) (b)

Figure 5.21 MJC material properties for aluminum alloy AA5083-H116.

5.5.2 Ballistic Limit Velocity

Numerical residual and ballistic limit velocities are compared with the experimental data reported earlier by Børvik et al. (2004). Both JC and MJC models are used for aluminum target plates. Variation of the residual velocities with the initial

velocities for different plate thicknesses of 15, 20, 25 and 30 mm are presented in Figure 5.23.

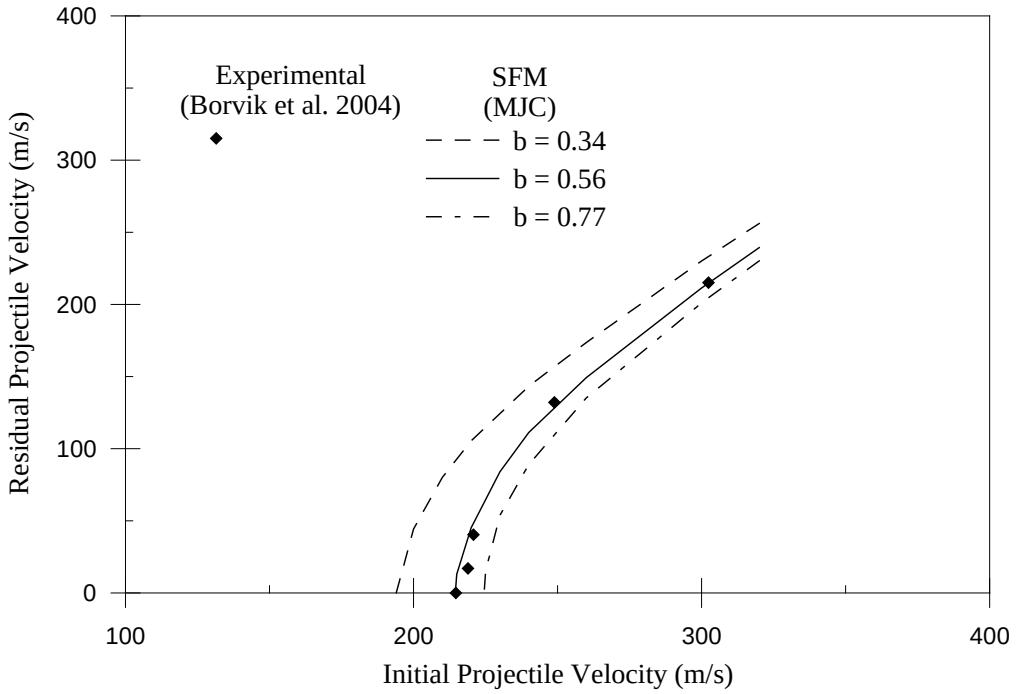

Figure 5.22 Effect of temperature parameter in conical projectile perforation of AA5083-H116.

Ballistic limit velocities increase linearly with the increasing plate thicknesses as shown in Figure 5.24 indicating a similar failure pattern for all plate thicknesses. The SFM results using the JC and MJC models show a good agreement with the experiment. However, the MJC model simulation results provide a better agreement than the JC model results. Both experimental and MJC model results demonstrate a close residual velocities for 20 mm and 25 mm plates. This is because of the lower strength for 25 mm aluminum plate compared to the other plates as can be observed in Figure 5.20. Because of this, 25 mm plate shows higher residual velocities which are nearly equivalent to the residual velocities of 20 mm plate. It also explains almost similar ballistic limit velocity for both 20 and 25 mm plates. Figure 5.25 presents the discrete time history of the perforation process of 15 mm thick aluminum plate perforated by a conical projectile using the SFM (MJC) model. The plate fails due to

ductile hole enlargement and forming petals at the rear surface of the target plates. Similar behavior is observed for all other plate thicknesses.

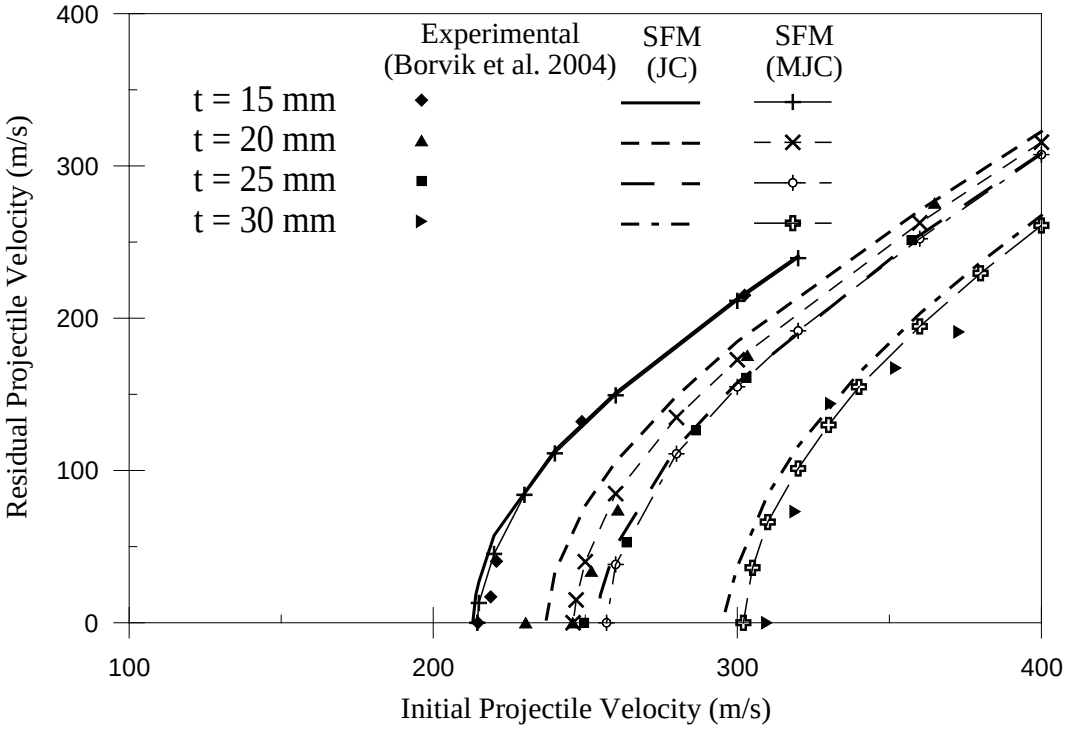

Figure 5.23 Numerical and experimental residual velocities of conical projectiles perforating aluminum plates.

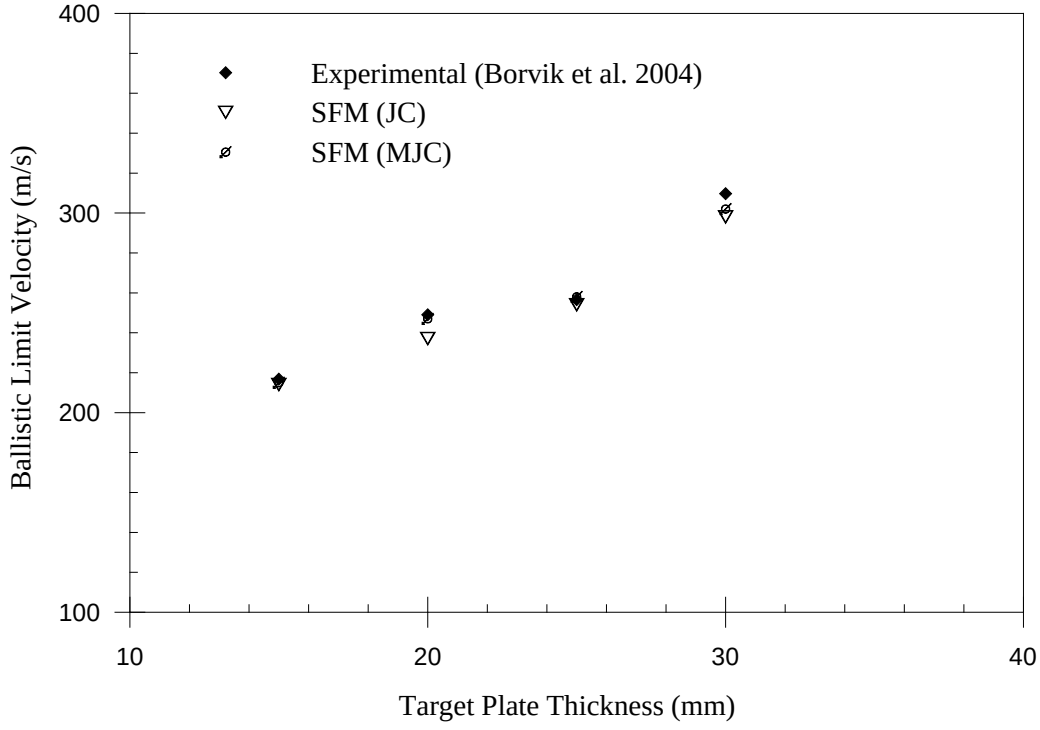

Figure 5.24 Numerical and experimental ballistic limit velocities for aluminum plate perforations.

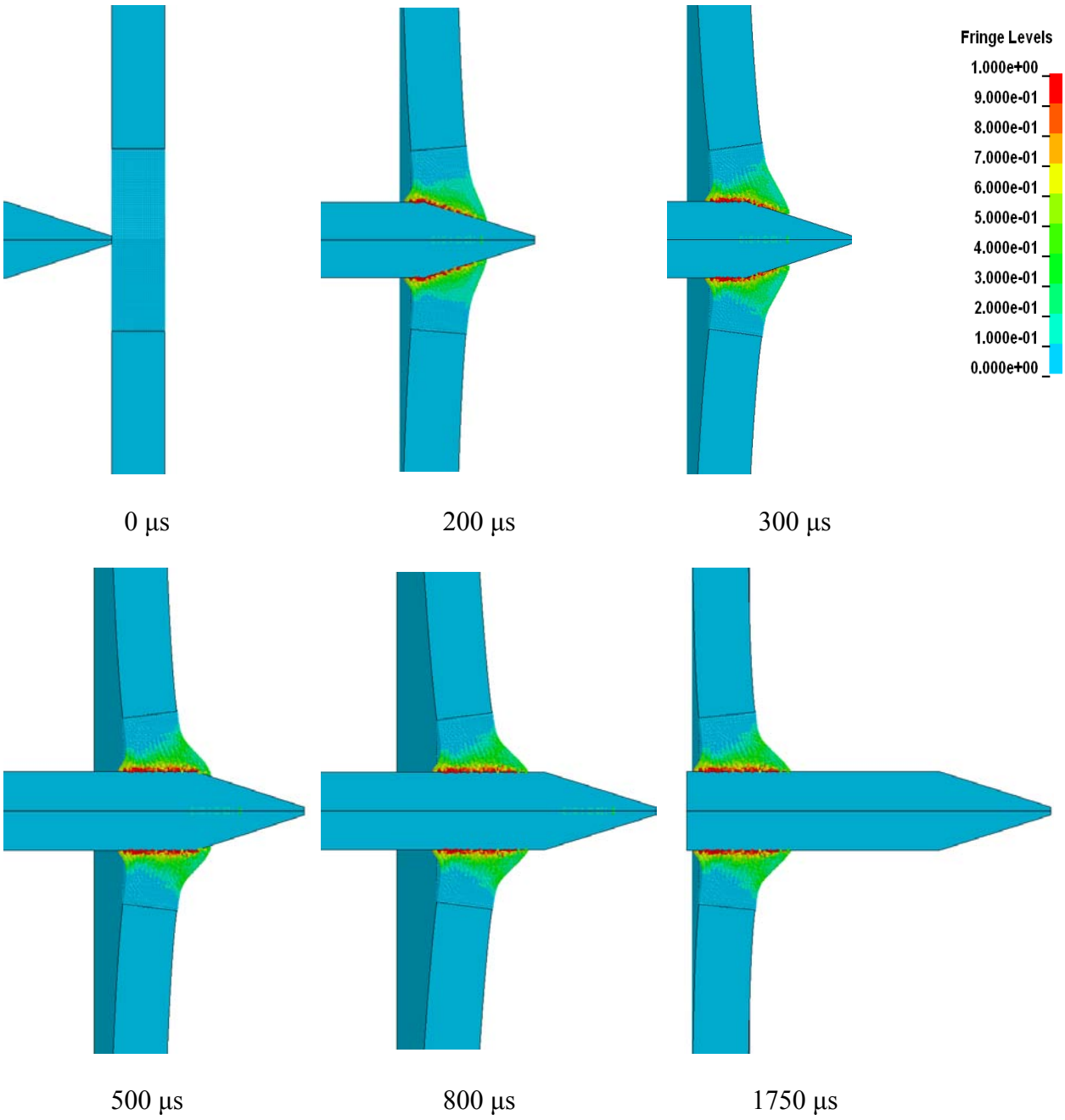

Figure 5.25 Time history of 15 mm thick aluminum plate perforated by conical projectiles at v_i = 214 m/s with effective plastic strain fringe contour.

5.6 Conclusions

The coupled SPH-FEM (SFM) and the modified Johnson-Cook (MJC) model are adopted to simulate high velocity perforation of titanium, steel and aluminum alloy target plates of different thicknesses impacted by steel projectiles with various

geometries. The MJC model parameters can be determined from uniaxial tensile tests at various strain rates and temperatures. Because of the improved computational model formulation, identification of the material parameters becomes straightforward using just three simple steps. The MJC model is applicable for both 2D and 3D problems as shown during the verification process. Numerical residual and ballistic limit velocities of perforation tests using the MJC material model show good agreement with the experimental results. Failure patterns of the target plates also agree with the experimental observations. Applications of the MJC model to wide varieties of material types validate the proposed model. Although the SFM is less accurate at low velocity impact problems, it provides excellent results for high velocity impact problems especially in the ordnance velocity region. Perforation simulations of 20 mm FSP with impact velocities at ordnance velocity region into the Ti-6Al-4V target plates are performed and good agreements with the experimental observations are achieved. Although variations in numerical results using the JC and MJC models are small, inclusions of accurate adiabatic temperature effect and simplified strain rate expression in the MJC model provide better results compared to the JC model. However, due to insufficient data for the JC model of Ti-6Al-4V, comparison of the JC and MJC models results are not available in the current study.

Chapter 6 Numerical Analysis of Projectile Impact on Concrete

6.1 Introduction

Concrete has been used against projectile impact for centuries. It has a wide assortment of applications for protective structures. Nuclear reactors must withstand automobile or aircraft impact as well as natural disasters (such as tsunami, tornado etc.) borne objects like rocks, trees and other flying objects. Ground/underground protective bunkers for personnel and storage facilities are often made of soil, concrete and steel. Several concrete composites with higher strength and ductility are under developments which are steadily replacing metals for protective applications.

Because of military interests in resisting projectile and blast impacts, a significant improvement of concrete as a material for protective structure has been observed. Various techniques namely, experimental, analytical and numerical have been developed to predict the resistance of concrete structures under projectile impacts. The finite element method (FEM) has been widely used to perform the projectile penetration/perforation into the concrete target. However, the FEM suffers from a major drawback, namely, severe element distortion under high pressure during the impact. This problem can be either solved by incorporating special measures, like element erosion approach in FEM or implementing the coupled smooth particle hydrodynamics – finite element method (SFM). In the element erosion approach, severely distorted elements are removed or 'eroded' from further analysis. The SFM is a promising new tool for high velocity impact simulations. However, it requires considerable computational resources. Since target domain for concrete plates are

significantly large, to the author's knowledge, presently it is not possible to employ the SFM for concrete penetration and/or perforation simulations. Therefore, the FEM with element erosion approach is incorporated in this study.

When a projectile impacts on a concrete target, a compressive wave is created at the contact surface and propagates along the target towards the other surface. Once the compressive wave reaches the free surface it reflects back as a tensile wave. If stresses generated by these waves are higher than the compressive/tensile strength of the concrete, fracture and fragmentation of concrete could occur. Therefore, in numerical studies of concrete penetration/perforation, both tensile and compressive failure criteria in the element erosion should be considered.

Maximum and minimum principal strains at failure are considered as the element erosion criteria in this study. Since these strain values are a numerical consideration not a failure of material and there are no direct methods available to determine these values, a calibration approach is adopted to establish these parameters. A wide range of maximum and minimum strains at failure parameters are used in numerical simulations while other parameters and conditions remain unchanged. A set of strains at failure is chosen based on the correlation with available experimental data. The same set of maximum and minimum strains is then verified with other experimental results.

6.2 Numerical Simulations of concrete penetration/perforation

Numerical analysis has been performed in the dynamic hydrocode LS-DYNA. To reduce computational effort, a Lagrangian mesh of 4-node two-dimensional (2D) axi-symmetric elements (y-axis of symmetry) is used for both projectile and target. Hourglass option is used to reduce the spurious zero energy modes. To define the conditions of contact between the steel projectile and the concrete target, a 2D automatic_surface_to_surface contact option is used for all cases. Pitch and yaw of

the projectiles observed in the experiment were significantly below the critical level (Forrestal et al., 1996; Frew et al., 1998; Hanchak et al., 1992), and hence, all the projectile impacts in the numerical models are considered normal impact in the current study.

Two perforations and one penetration tests of concrete with compressive strength of 48, 140 and 62.8 MPa, respectively are used to establish the erosion parameters. Hanchak et al. (1992) conducted two projectile perforation tests into concrete targets. In the perforation experiments, 48 and 140 MPa concrete slabs with dimension of 610 x 610 x 178 mm^3 were impacted by 25.4 mm diameter ogive-nose maraging steel (T-250) projectiles at striking velocity ranging from 300 m/s to 1100 m/s. The residual velocities of the projectiles obtained in the experiments were plotted against the initial projectile velocities. Other test includes the penetration test of the 20.3 mm diameter ogive-nose 4340 steel projectile into 62.8 MPa concrete (Forrestal et al., 1996) targets of cylindrical in shape with a diameter of 0.51 m and the length varying from 0.91 m to 1.83 m. The striking velocities of the projectile were varied from 450 m/s to 1224 m/s. A typical ogive-nose projectile is illustrated in Figure 6.1; whereas, dimensions and properties of the concrete targets and the steel projectiles are given in Table 6.1. Penetration depths of the projectiles are measured for various initial projectile velocities.

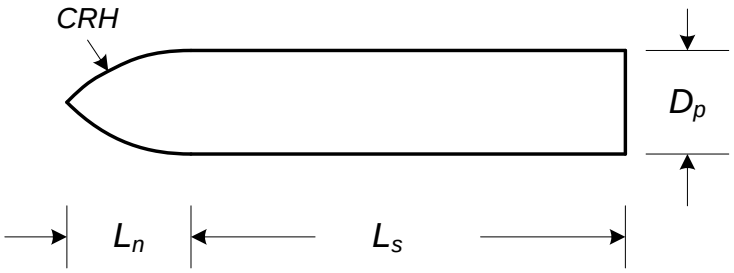

Figure 6.1 A typical ogive-nose projectile geometry (CRH - caliber-radius-head).

Table 6.1 Properties of concrete target and steel projectile

	Perforation (Hanchak et al., 1992)		Penetration (Forrestal et al., 1996)		Penetration (Frew et al., 1998)	
Concrete Target						
f_c' (MPa)	48.0	140.0	62.8	51.0	58.4	58.4
ρ_0 (kg/m^3)	2440	2520	2300	2300	2320	2320
Target dia. (m)	0.61	0.61	0.51	0.91	0.51	0.91
Target length (m)	0.178	0.178	0.91-1.52	1.83-2.74	0.94-1.93	1.07-3.05
Steel Projectile						
Mass, m (kg)	0.50	0.50	0.48	1.60	0.478	1.62
Density, ρ_0 (kg/m^3)	8020	8020	7850	7850	7850	7850
Yield Stress, σ_Y (GPa)	1.72	1.72	1.45	1.45	1.45	1.45
Shank dia., D_p (mm)	25.4	25.4	20.3	30.5	20.3	30.5
Shank length, L_s (mm)	101.6	101.6	169.5	254.3	169.5	254.2
Nose length, L_n (mm)	42.1	42.1	33.7	50.5	33.7	50.5
Caliber-radius-head	3	3	3	3	3	3

6.2.1 Material Models

Holmquist-Johnson-Cook (HJC) material model for concrete (Holmquist et al., 1993) is used to model the concrete targets. The HJC is an elastic-plastic damage model which considers high strain, strain rate effects and damage. Detail description of the HJC model is given in Chapter 2. Material properties of the HJC concrete model for plain concrete with compressive strength of 48 MPa are listed in Table 6.2.

The HJC concrete model does not have the element erosion option, and hence, the element erosion is adopted separately along with the material model. Both compression and tension strains at failure are used as erosion criteria in the element

erosion option. The present study covers the compression strain values at failure ranging from -0.4 to -1.2; and those associated with tension failure from 0.2 to 1.0.

Table 6.2 Material properties of HJC concrete model for 48 MPa concrete (Holmquist et al., 1993)

ρ_0 (kg/m^3)	E (GPa)	v	G (GPa)	T (MPa)	$\varepsilon^f_{\min}$	
2440	35.7	.2	14.86	4	0.01	
$\mathcal{A}$	$\mathcal{B}$	$\mathcal{N}$	C	$\sigma^*_{\max}$	D_1	D_m
0.79	1.60	0.61	0.007	7.0	0.04	1.0
P_{crush} (GPa)	μ_{crush}	P_{lock} (GPa)	μ_{lock}	K_1 (GPa)	K_2 (GPa)	K_3 (GPa)
0.016	0.001	0.80	0.1	85	-171	208

For the steel projectile material modeling, a simple elastic-plastic material model is used. As the projectile deformation is expected to be minimal except for limited erosion near the projectile nose, an effective strain value at failure is also adopted as an element erosion criterion in the constitutive model for the steel projectile.

6.2.2 Mesh Sensitivity Study

In order to perform the mesh sensitivity study, a uniform mesh is used in the concrete target domain along the path of the projectile and the rest of the domain is modeled with gradually coarser mesh towards the boundary. For the uniform mesh region, three different mesh sizes are chosen, 1 mm x 1 mm, 2 mm x 2 mm and 4 mm x 4 mm. Two cases are selected, (i) the perforation of 48 MPa concrete (Hanchak et al., 1992) and (ii) the penetration of 62.8 MPa concrete (Forrestal et al., 1996). The residual velocities and the penetration depths against the initial velocities of the projectile for 48 MPa and 62.8 MPa concretes with three mesh sizes are plotted in Figure 6.2 and 6.3 respectively. A mesh convergence is achieved with a mesh size of

2 mm x 2 mm for both cases and adopted in subsequent studies. Figure 6.4 shows the mesh of the projectile and the target for the perforation test of 48 MPa concrete.

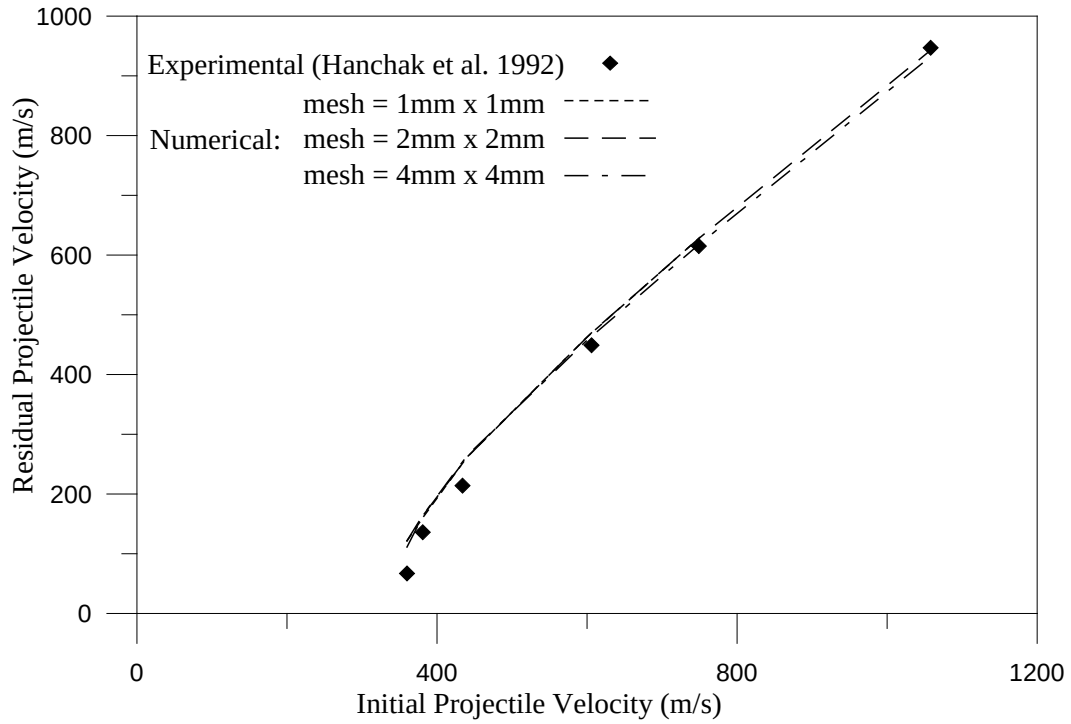

Figure 6.2 Comparison of projectile residual velocities against initial velocities in the perforation test of 48 MPa concrete with varying mesh size.

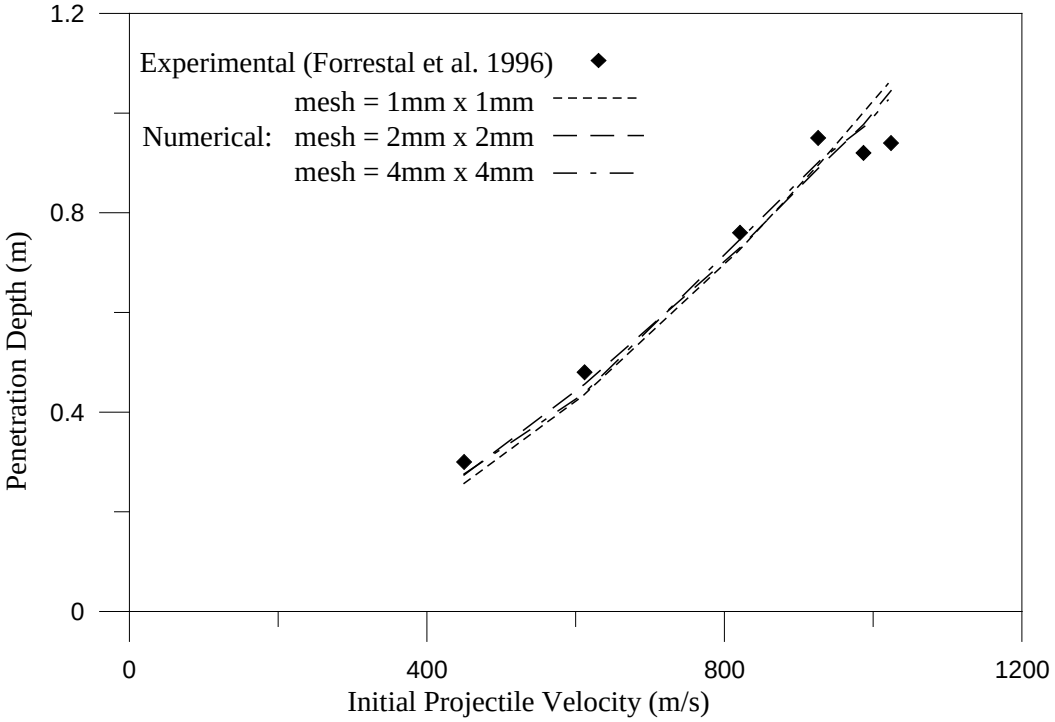

Figure 6.3 Comparison of projectile penetration depths against initial velocities in the penetration test of 62.8 MPa concrete with varying mesh size.

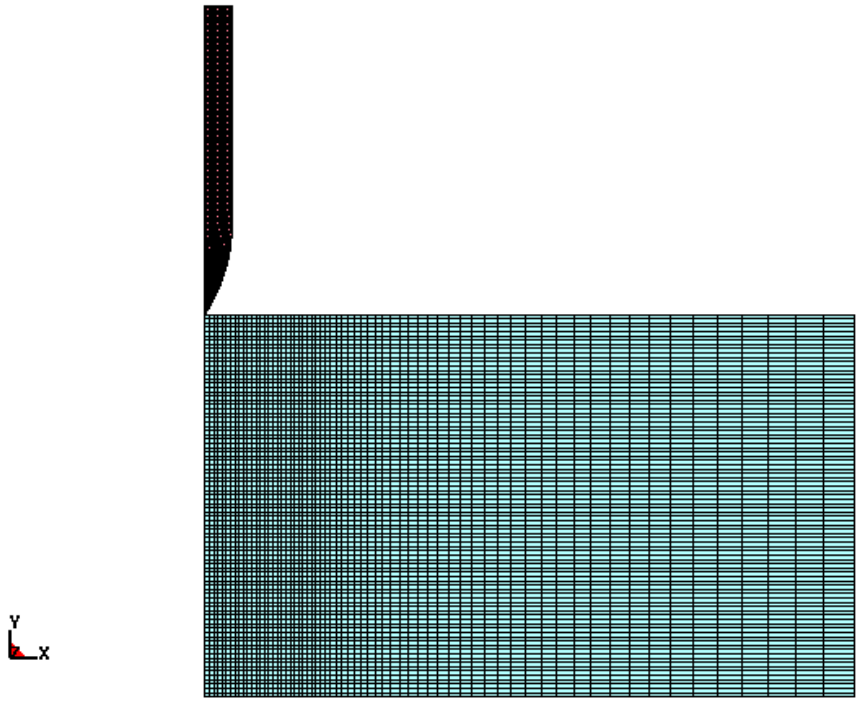

Figure 6.4 A typical mesh of the projectile and the target.

6.2.3 Determination of Element Erosion Parameters

The residual velocities and the penetration depths of the projectile from the perforation and penetration tests respectively are adopted in the calibration of the erosion parameters. The root mean square error (RMSE) is evaluated using the following expression,

$$RMSE = \sqrt{\frac{1}{n}\sum_{i=1}^{n}\left(\frac{(Exp)_i - (Num)_i}{(Exp)_i}\right)^2} \tag{6.1}$$

Here, n is the number of points, *Exp* is the observed experimental data and *Num* is the numerical results. Table 6.3 shows the root mean square errors for three different cases of concrete perforation/penetration for various combinations of tensile failure strain (tfs) and compressive failure strain (cfs) values. It is observed that a range of tfs values of 0.4 to 0.5 and cfs values of -0.8 to -1.0 provide results that are in good agreement with the test values as illustrated in Figures 6.5 and 6.6. As the variation of

numerical results is minimal, it is suggested that the tfs value of 0.5 and cfs value of -1.0 are adopted for the subsequent analyses. Projectile residual velocities plotted against the projectile initial velocities for high strength concrete (f_c' = 140 MPa) as illustrated in Figure 6.7, show good correlation with the test data.

Table 6.3 RMSE for various tfs and cfs
(Shaded portion encompassing the desirable range)

		Root mean square error (RMSE)		
tfs	cfs	Perforation (f_c' = 48 MPa)	Perforation (f_c' = 140 MPa)	Penetration (f_c' = 62.8 MPa)
0.2	-0.5	0.649	0.227	0.271
0.2	-0.7	0.659	0.228	0.252
0.2	-0.8	0.659	0.228	0.252
0.2	-1.0	0.668	0.228	0.252
0.2	-1.2	0.659	0.228	0.252
0.3	-0.5	0.617	0.094	0.219
0.3	-0.7	0.551	0.046	0.200
0.3	-0.8	0.579	0.046	0.195
0.3	-1.0	0.552	0.046	0.194
0.3	-1.2	0.579	0.046	0.195
0.4	-0.5	0.618	0.095	0.216
0.4	-0.7	0.341	0.189	0.072
0.4	-0.8	0.297	0.037	0.073
0.4	-1.0	0.311	0.198	0.077
0.4	-1.2	0.280	0.198	0.077
0.5	-0.5	0.619	0.108	0.212
0.5	-0.7	0.345	0.099	0.079
0.5	-0.8	0.262	0.104	0.082
0.5	-1.0	0.283	0.381	0.087
0.5	-1.2	0.314	0.058	0.091
0.7	-0.5	0.620	0.107	0.215
0.7	-0.7	0.330	0.149	0.080
0.7	-0.8	0.336	0.240	0.086
0.7	-1.0	0.050	0.164	0.142
0.7	-1.2	0.088	0.450	0.147
1.0	-0.5	0.618	0.099	0.219
1.0	-0.7	0.348	0.143	0.079
1.0	-0.8	0.312	0.448	0.085
1.0	-1.0	0.110	0.098	0.156
1.0	-1.2	0.084	0.450	0.166

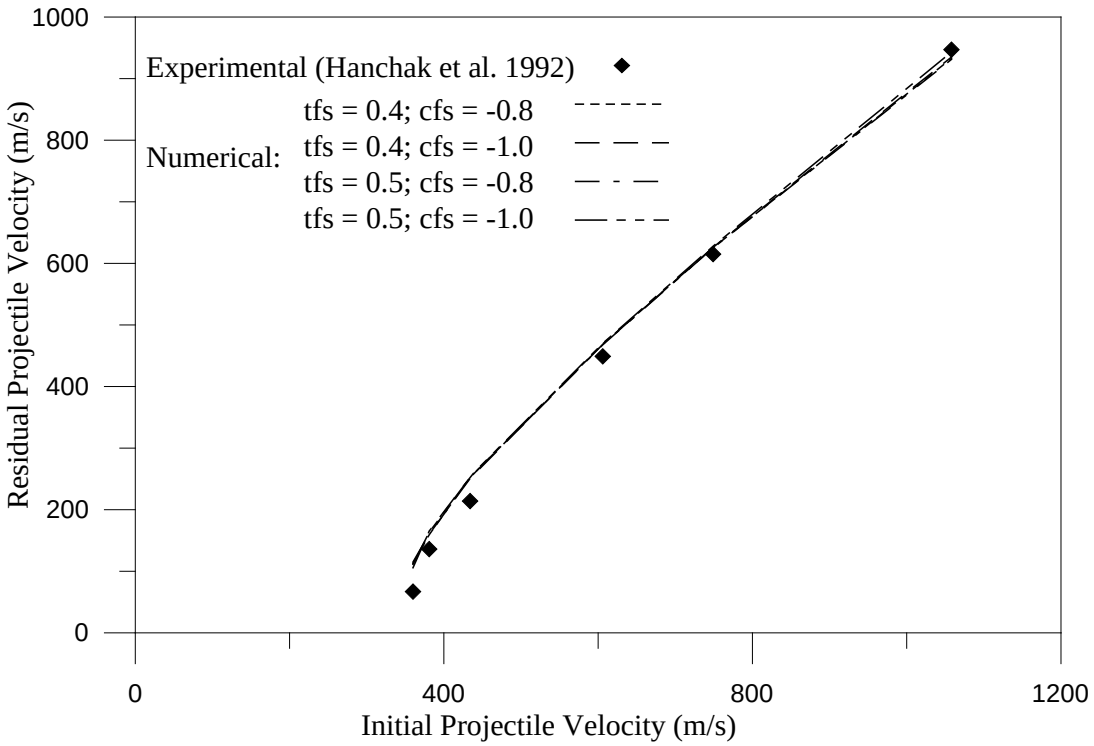

Figure 6.5 Comparison of projectile residual velocities against initial velocities in the perforation test of 48 MPa concrete with varying tfs and cfs.

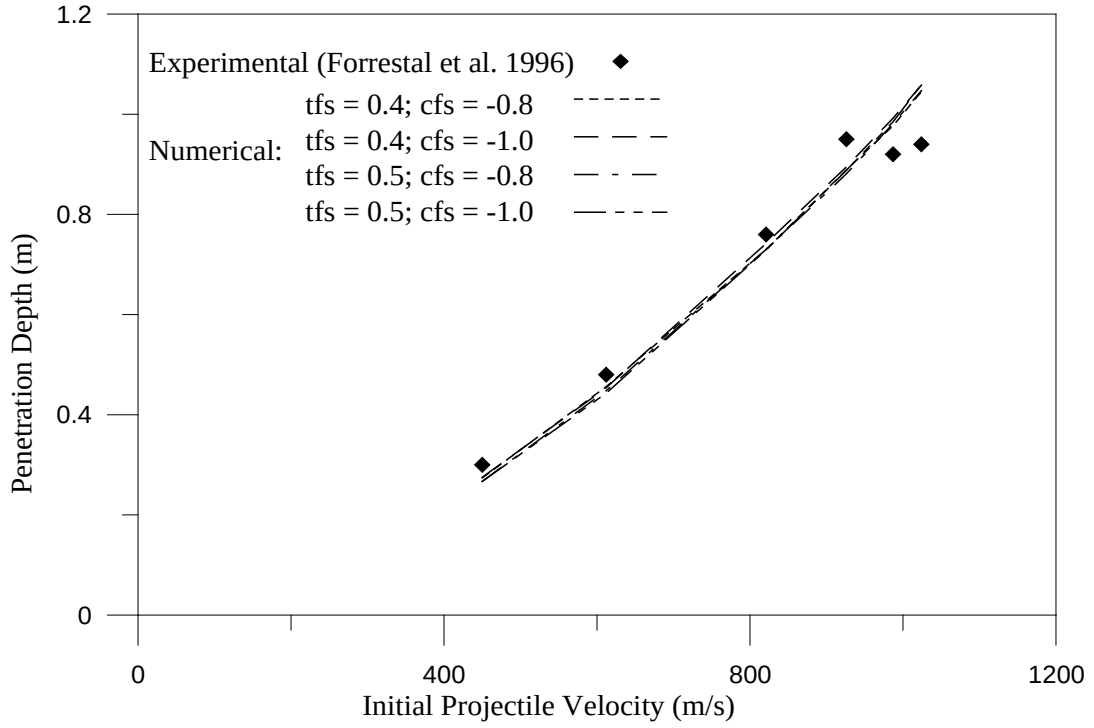

Figure 6.6 Comparison of projectile penetration depths against initial velocities in the penetration test of 62.8 MPa concrete with varying tfs and cfs.

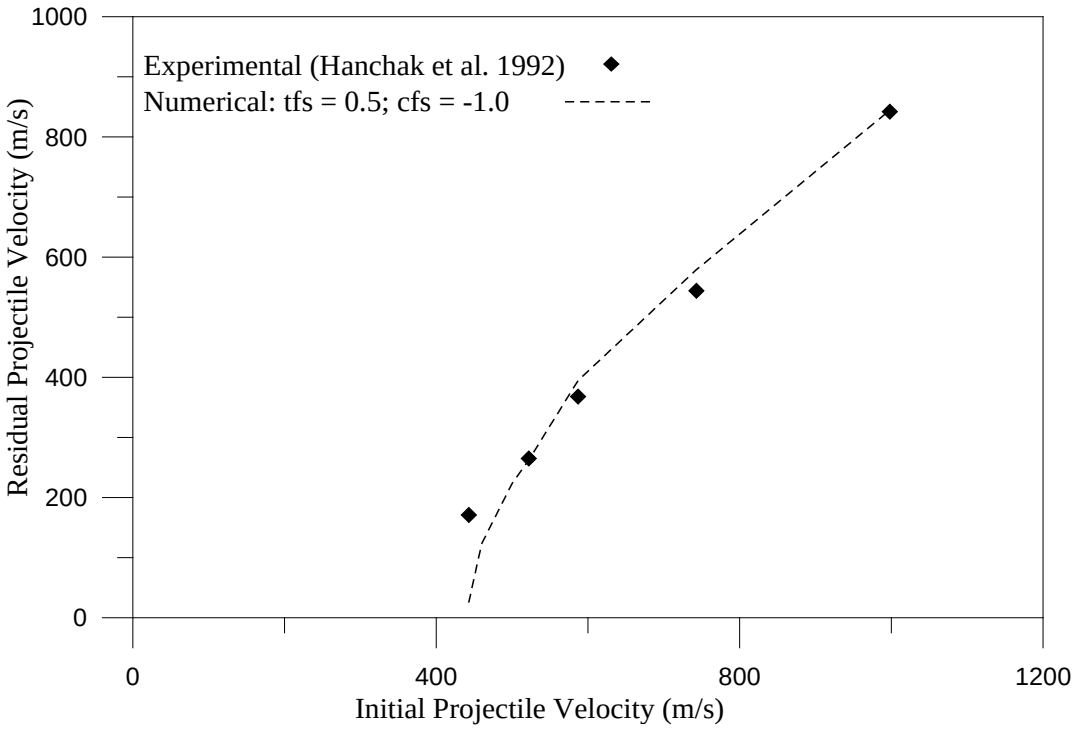

Figure 6.7 Comparison of projectile residual velocities against initial velocities in the perforation test of 140 MPa concrete.

In the perforation experiment, Hanchak et al. (1992) observed conical crater regions at both top and bottom surfaces and a cylindrical tunnel region in the middle portion. Figure 6.8 displays the concrete target after perforation by the projectile at a striking velocity of 749 m/s. The missing elements along the path of the projectile have been eroded from the analysis. It shows a tunnel region in between the top and bottom crater regions. It is observed that the conical top and bottom crater regions occur mostly due to the compressive and tensile waves involved in the impact process; whereas, the tunnel region forms when the projectile passes through the target by removing the elements in front of the projectile and the latter has a diameter similar to the diameter of the projectile. This indicates that the numerical approach with element erosion is able to recapture the failure patterns observed in the experiment.

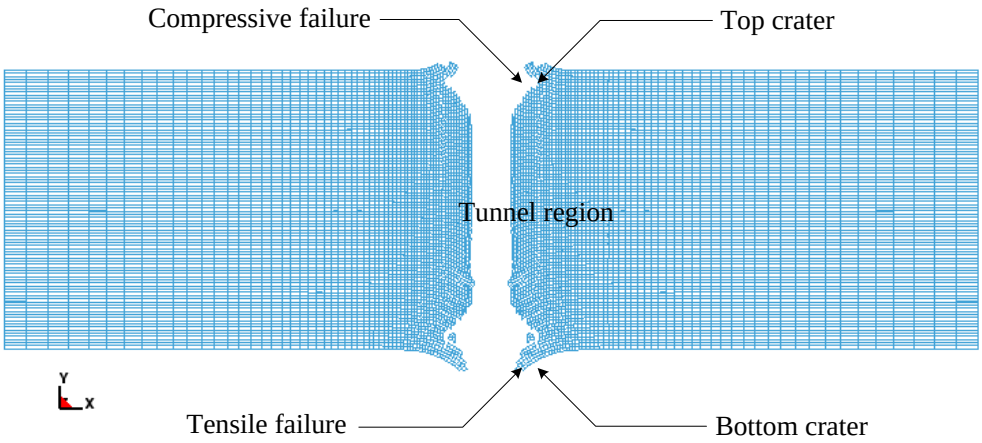

Figure 6.8 Concrete target after perforation of 48 MPa concrete with initial velocity of 749 m/s.

6.3 Verification of the Element Erosion Method

Three penetration cases are used herein to verify the selected erosion parameters (tfs = 0.5 and cfs = -1.0). The first one is the penetration of 30.5 mm ogive-nose 4340 steel projectile into 0.91 m diameter concrete target with unconfined compressive strength of 51.0 MPa (Forrestal et al., 1996), and initial projectile velocities varying from 405 m/s to 1201 m/s. The comparison of numerically obtained penetration depths with the experimental data are plotted in Figure 6.9. The other two are the penetration studies of 20.3 mm and 30.5 mm ogive-nose 4340 steel projectiles into 0.51 m and 0.91 m diameter concrete targets with unconfined compressive strength of 58.4 MPa (Frew et al., 1998), and initial projectile velocities varying from 440 m/s to 1176 m/s and 1.07 m to 3.05 m, respectively. Once again, Figure 6.10 demonstrates that the numerical results are in good agreement with experimental results.

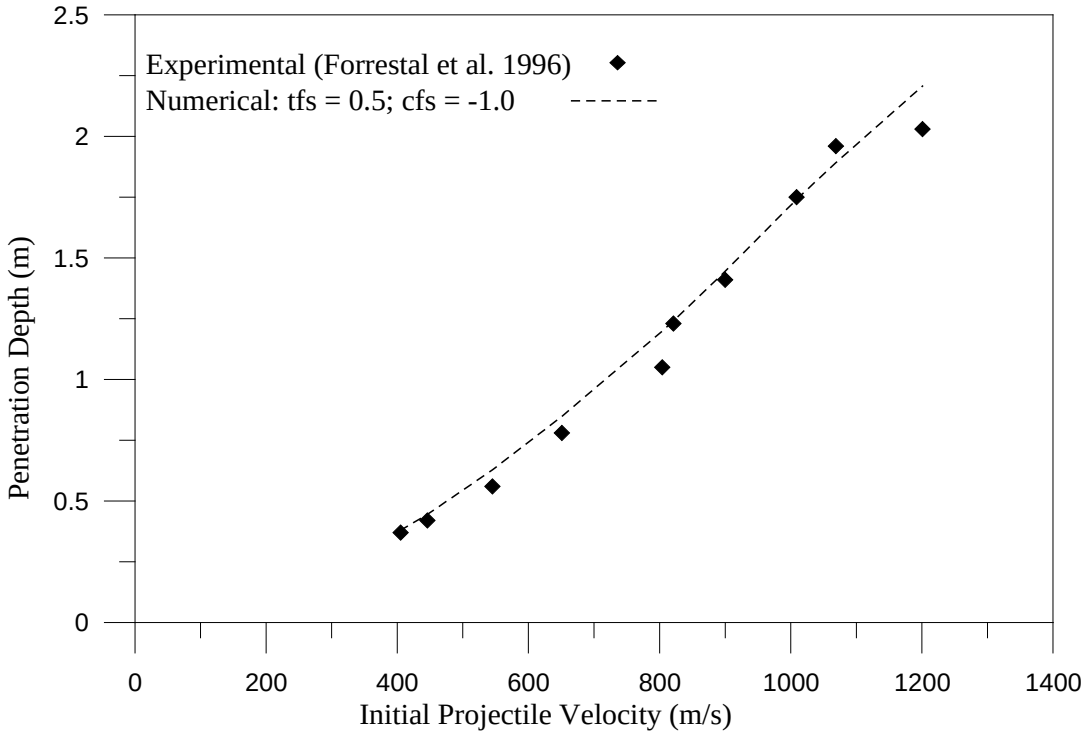

Figure 6.9 Comparison of penetration depths against initial velocities for the 51.0 MPa concrete penetration test with projectile diameter of 30.5 mm.

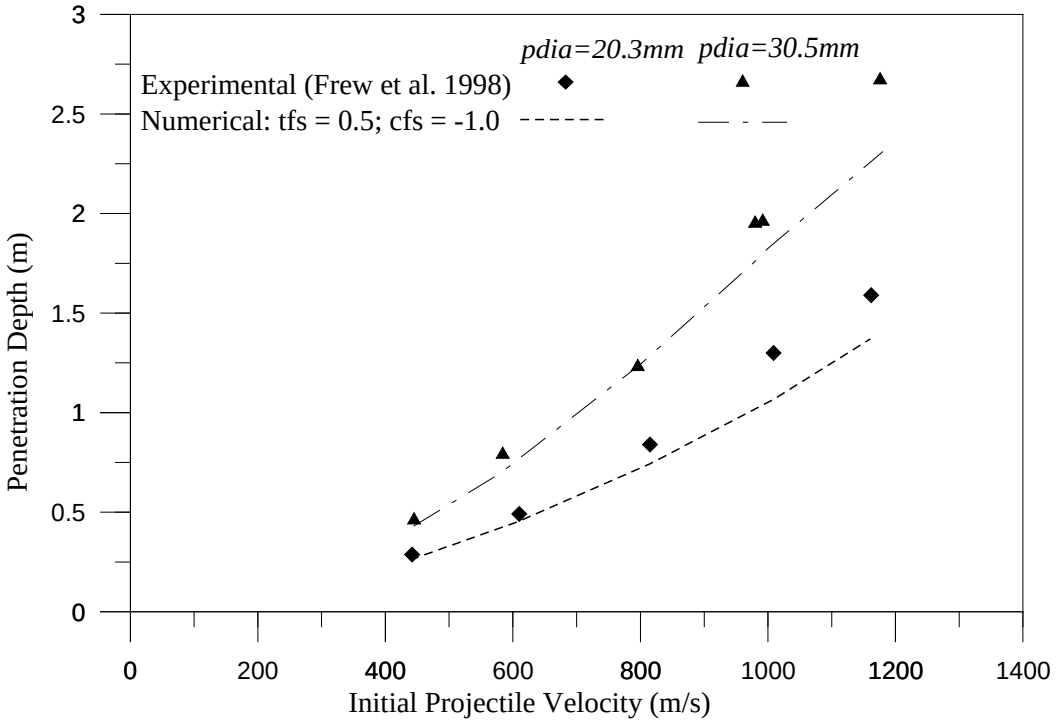

Figure 6.10 Comparison of penetration depths against initial velocities for the 58.4 MPa concrete penetration tests with projectile diameter (pdia) of 20.3 and 30.5 mm.

6.4 Verification of the Modified Holmquist-Johnson-Cook (MHJC) Model

To verify the MHJC model, concrete perforation simulation is performed and results are compared with the test data. Hanchak et al. (1992) conducted perforation study of 610 x 610 x 178 mm^3 concrete plates by ogive nose steel projectiles. Compressive and tensile strength of concrete are 48 MPa and 4 MPa respectively. Projectile has the length and diameter of 143.7 mm and 25.4 mm respectively. In the experiment, residual projectile velocities were recorded and a residual versus initial projectile velocities curve was constructed to determine the ballistic performance of the concrete plate. Three layers of steel reinforcement were included in concrete plates. Although steel reinforcements reduced rear surface damage, they provided little protection against projectile penetration.

Finite element method (FEM) with 2D axi-symmetrical elements is adopted for both projectile and concrete target in the numerical simulation. A 2D surface to surface contact is used between the projectile and target. Pitch and yaw of the projectile was negligible, and hence, ignored during the simulation. Based on the convergence study in Section 6.2.2, a uniform mesh of 2 x 2 mm^2 was employed in the target domain along the projectile path, but a gradually coarse mesh towards the boundary is implemented for the rest of the domain to optimize the computation resources. To eliminate the severe element distortion problem during the projectile penetration, element erosion option is utilized in this study.

The MHJC model is employed as a user defined material model for concrete. All the material properties for 48 MPa concrete are given in Tables 3.3 and 3.4. Element erosion option is included in the proposed model and maximum and minimum principal strain values of 0.5 and -1.0 are employed for this case. These

values are similar to the values obtained previously in Section 6.2.3. Projectile is made of steel and subjected negligible damage and/or deformation during the penetration event. Therefore, a simple elastic-plastic material model is used for the projectile. Material properties for the projectile are given in Table 6.4.

Initial projectile velocities varied between 340 m/s to 1160 m/s. Numerical residual velocities are compared with experimental observations (Hanchak et al., 1992) as displayed in Figure 6.11. Simulations results show a close correlation with the test data. Figure 6.11 also includes simulations results using the HJC material model for concrete. Although both MHJC and HJC model data agree well with the experimental observation, the HJC model overestimates the projectile residual velocities. This signifies the improvement of the MHJC model for concrete. Figure 6.12 illustrates perforation of process of the ogive-nose projectile with an initial velocity of 606 m/s. Similar to those observed in the test, the simulated target plate exhibits conical entry and conical exit crater regions with a cylindrical tunnel region in between.

Table 6.4 Material properties for steel projectile

σ_Y (GPa)	ρ_0 (kg/m^3)	E (GPa)	ν	E_t (GPa)
1.720	8020	200	0.30	15.0

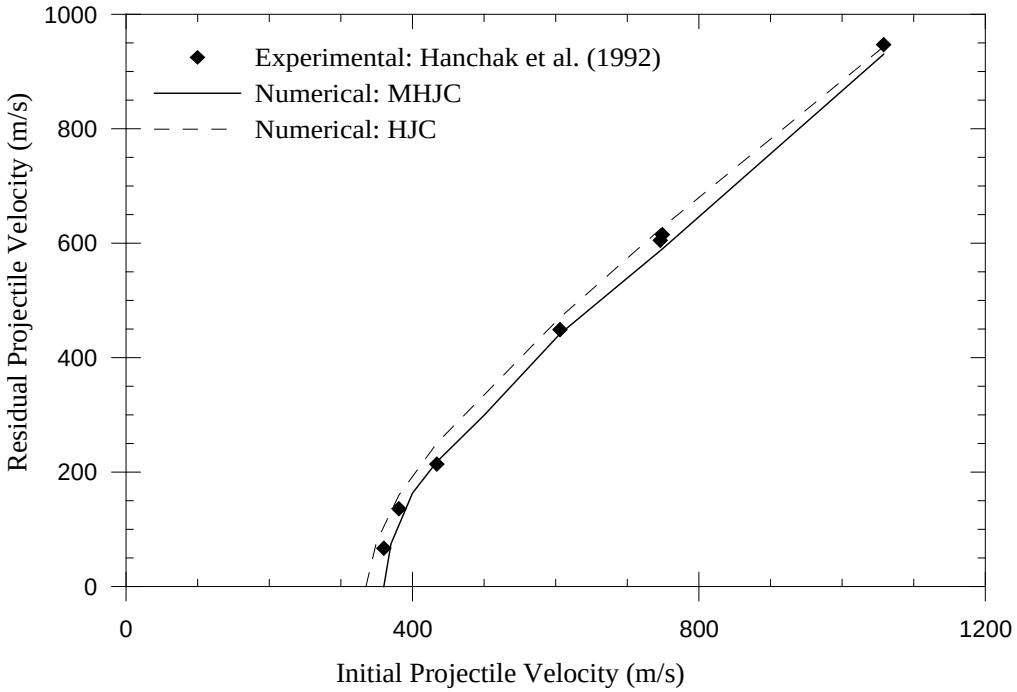

Figure 6.11 Comparison of the numerical and experimental residual velocities for concrete with compressive strength of 48 MPa.

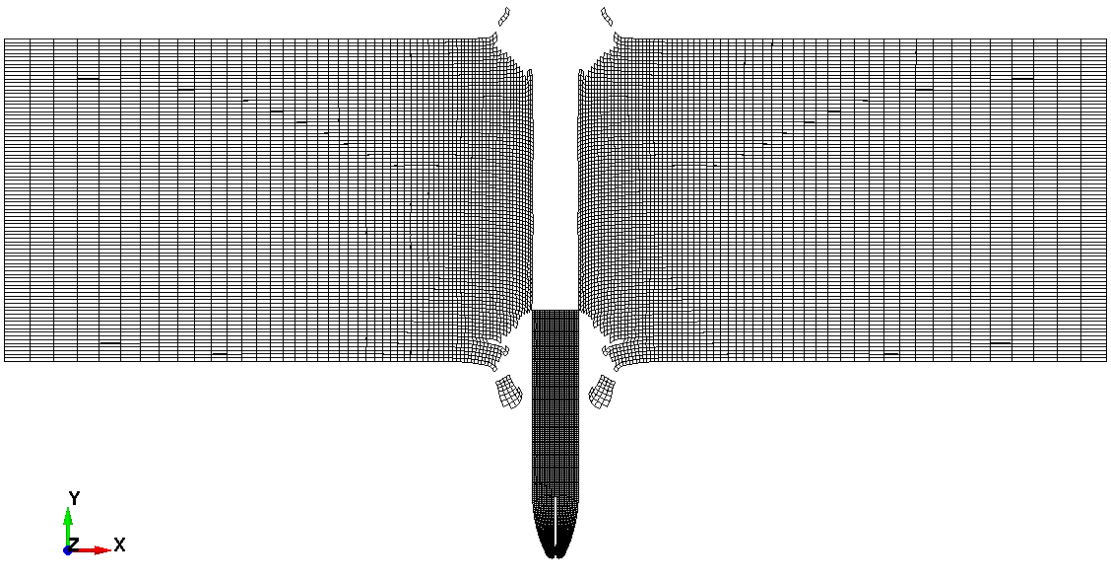

Figure 6.12 Perforation of concrete target with initial projectile velocity of 606 m/s.

6.5 Penetration of Concrete using MHJC Model

Tai (2009) conducted penetration/perforation test of normal concrete (NC) and reactive powder concrete (RPC) plates. Compressive strengths of NC and RPC plates are about 25 MPa and 160 MPa respectively. Tai (2009) also studied the effect of

steel fiber reinforcement in concrete against projectile impact. Inclusion of fiber reinforcement increases tensile and flexural strengths of concrete which indeed improve impact resistance of the target plate. Although high strength concrete exhibits better performances, the relationship between the resistance and strength is not clear from the test results.

In the experiment, blunt projectile with length, diameter and mass of 75 mm, 25 mm and 0.297 kg, respectively was used. Projectile was made of SKH-51 tool steel with considerable hardness to minimize plastic deformation. Material properties of the projectile are given in Table 6.5. Strike velocities of the projectile vary between 27 m/s – 104 m/s. Dimensions of the concrete target plates are 310 x 310 x 50 mm^3. A square frame was used to clamp the target plate. In the experiment, penetration depths and final damage states of the target plates were documented. Three examples are considered herein for numerical simulation. They are (i) normal concrete plates with no reinforcement (NC-F0), (ii) normal concrete with 2% steel fiber reinforcement (NC-F2), and (iii) high strength concrete plate with 2% steel fiber reinforcement (RPC-F2).

Numerical simulation is performed using finite element method (FEM) with 2D axi-symmetrical elements for both projectile and target plate. Figure 6.13 presents the numerical model of the projectile and target. A uniform mesh of 2 x 2 mm^2 is used near the impact zone; however a gradually coarser mesh towards the boundary is adopted for the rest of the target domain. The projectile and target plate are modeled using 150 and 50000 elements, respectively. Appropriate boundary condition is applied for the target plate which is clamped at the outer edge. A surface to surface contact option is used where the projectile is the master surface. Effect of reinforcement in the projectile penetration depth is negligible for high velocity

penetration of concrete slabs. In the FE simulation, reinforcement is ignored and the concrete slab is considered as an isotropic material.

The modified Holmquist-Johnson-Cook (MHJC) is adopted for the concrete target plate as a user defined material model. Procedure for obtaining material properties are described in Section 3.2.5. Material properties for normal and high strength concrete with 2% steel fiber reinforcement are presented in Table 6.6 and 6.7. To eliminate the element distortion problem, element erosion approach is employed and maximum and minimum principal strains at failure are adopted as erosion criteria herein. Earlier study (Section 6.2.3) indicated maximum and minimum principal strain value of 0.5 and -1.0 as erosion criteria for ogive-nose projectile. Similar values are selected for this study. In the experiment, the projectile exhibited negligible plastic deformation and damage. Therefore, a simple elastic plastic material model is implemented for the projectile.

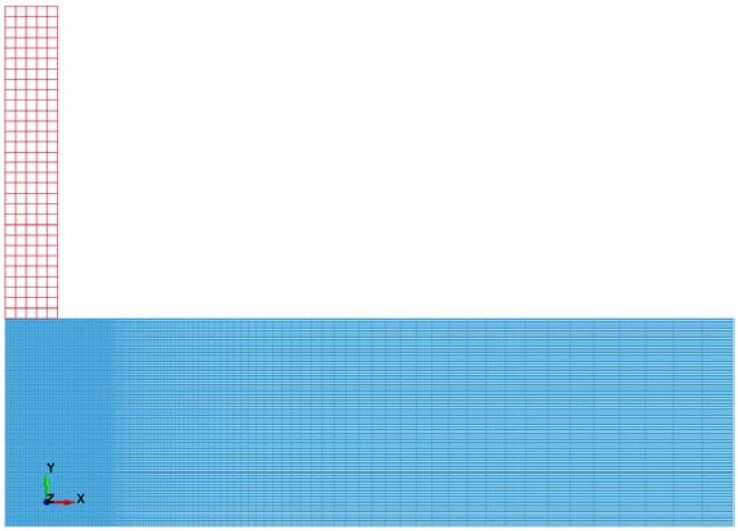

Figure 6.13 Numerical model of the projectile and target plate.

Table 6.5 Material properties for SKH-51 tool steel projectile

σ_Y (GPa)	ρ_0 (kg/m^3)	E (GPa)	ν
1.910	7890	214	0.30

Table 6.6 MHJC model parameters for NC-F2 concrete

K (GPa)	f_c' (MPa)	f_t' (MPa)	ρ_0	$\mathcal{A}$	$\mathcal{B}$	$\mathcal{N}$
13.6	25.2	3.1	2350.0	0.7	2.0	0.80
P_{crush} (MPa)	μ_{crush}	μ_m	P_{comp} (GPa)	μ_{comp}	K_m (GPa)	
8.33	0.000615	0.177	1.343	0.1884	118.0	
d_g	d_h	$\left(\varepsilon_p^f\right)_{\min}$				
0.04	2.0	0.008				

Table 6.7 MHJC model parameters for RPC-F2 concrete

K (GPa)	f_c' (MPa)	f_t' (MPa)	ρ_0	$\mathcal{A}$	$\mathcal{B}$	$\mathcal{N}$
42.29	178.3	21.9	2600.0	0.7	1.35	0.52
P_{crush} (MPa)	μ_{crush}	μ_m	P_{comp} (GPa)	μ_{comp}	K_m (GPa)	
59.43	0.0014	0.0842	4.602	0.1232	118.0	
d_g	d_h	$\left(\varepsilon_p^f\right)_{\min}$				
0.40	2.0	0.015				

Penetration depths for NC-F0, NC-F2 and RPC-F2 concrete are determined at initial projectile velocity ranging between 27 m/s to 104 m/s. Figure 6.14 compares the experimental and numerical penetration depths. For NC-F0 and NC-F2 concrete plates only low projectile impact velocities of 27 m/s and 41.7 m/s respectively achieve partial penetrations. Projectiles with higher impact velocities complete the perforation process in both experiments and numerical simulations. Therefore, penetration depths for only strike velocities of 27 m/s and 41.7 m/s are plotted in Figure 6.14. Numerical results show good correlation with the test observations. Penetration process of the projectile is illustrated in Figure 6.15 where blunt projectile

with initial impact velocity of 41.7 m/s strikes the NC-F2 concrete plate. It also includes damage fringe contour. As observed in the figure, cracks propagate from the impact surface towards the rear surface. However, damage in the rear surface is considerably small compared to the entry surface for this case. Compared to the experimental penetration depth of 5.3 mm, penetration depth of 7.96 mm is achieved in the numerical simulation. Although numerical penetration depth is slightly higher than the test data, numerical simulation describes the failure pattern with reasonable success.

Figure 6.16 – 6.18 demonstrates failure patterns of the NC-F0, NC-F2, and RPC-F2 concrete plates, respectively. Normal strength concrete plates with no reinforcement (NC-F0) are subjected to heavy damage at low impact velocities (27 – 56.8 m/s). For impact velocities of 35.7 m/s and 56.8 m/s, concrete plates are perforated completely by the projectiles, except for impact velocity of 27 m/s where a partial penetration is achieved. Inclusion of 2% steel fiber reinforcement in normal concrete plate (NC-F2) has improved its resistance against impact. In this case fiber reinforcement constrains crack propagation, and hence, reduces the damage area. For projectile strike velocity of 41.7 m/s a partial penetration with little damage is observed as shown in Figure 6.17. However, in cases of projectile with impact velocities of 56.8 m/s and 64.1 m/s complete perforation with heavy damage are monitored. In both NC-F0 and NC-F2 cases complete perforation occurs due to formation of shear cracks. These observations are consistent with the test procedure. High strength reactive powder concrete with 2% steel fiber reinforcement (RPC-F2) has strength about 7 times higher than that of the NC-F2 concrete. Because of this damage, in the concrete plate is more localized and only partial penetration is achieved for projectile impact velocities of 76 m/s, 85 m/s and 104 m/s. Although few shear cracks are formed during the penetration, none of them reach the rear surface,

and thus, causing fragmentation and/or spalling of concrete materials as observed in Figure 6.18.

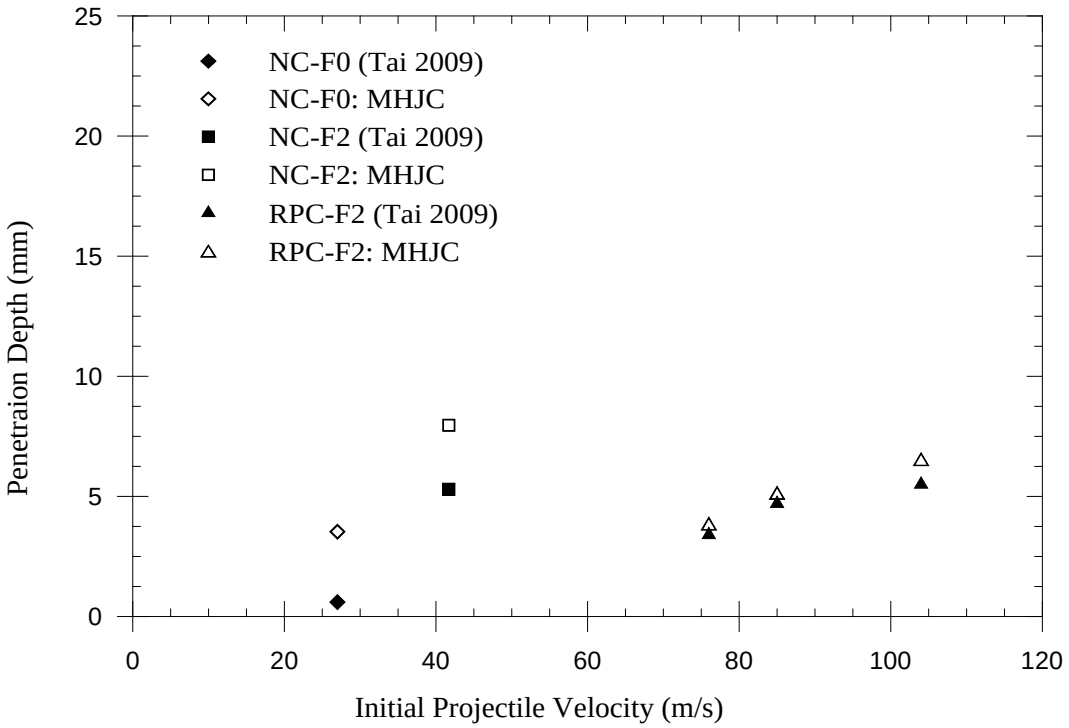

Figure 6.14 Experimental and numerical penetration depths comparison for various strengths concrete.

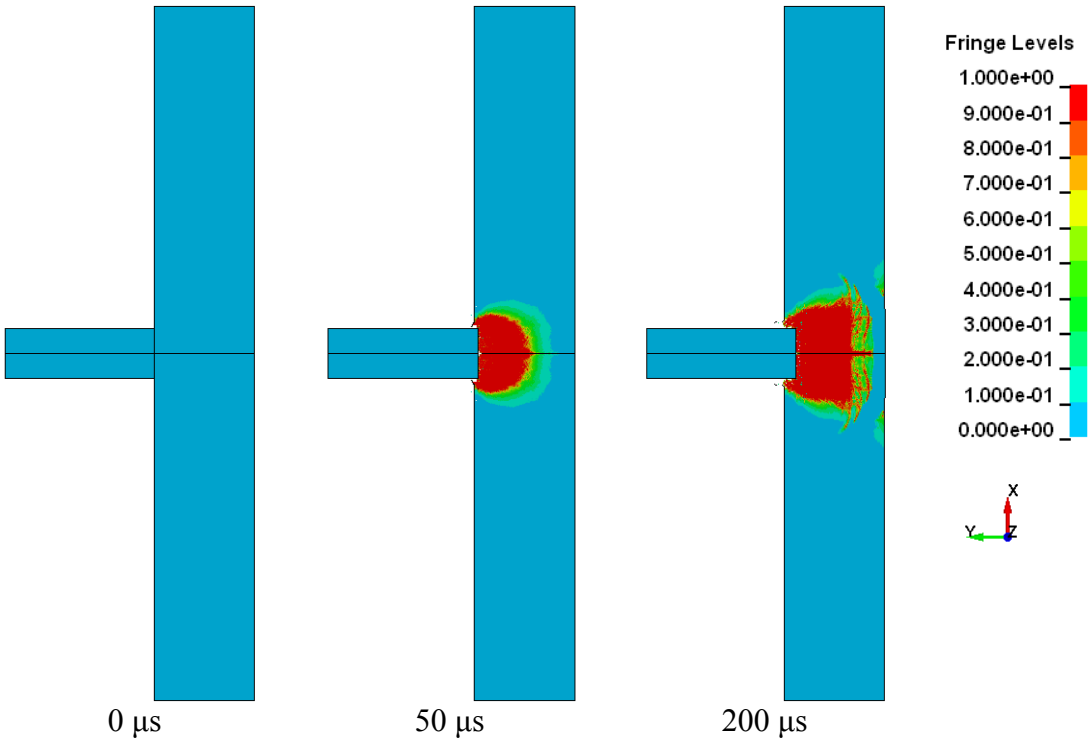

Figure 6.15 Penetration time history of NC-F2 concrete plate by projectile at v_i = 41.7 m/s with damage fringe contour.

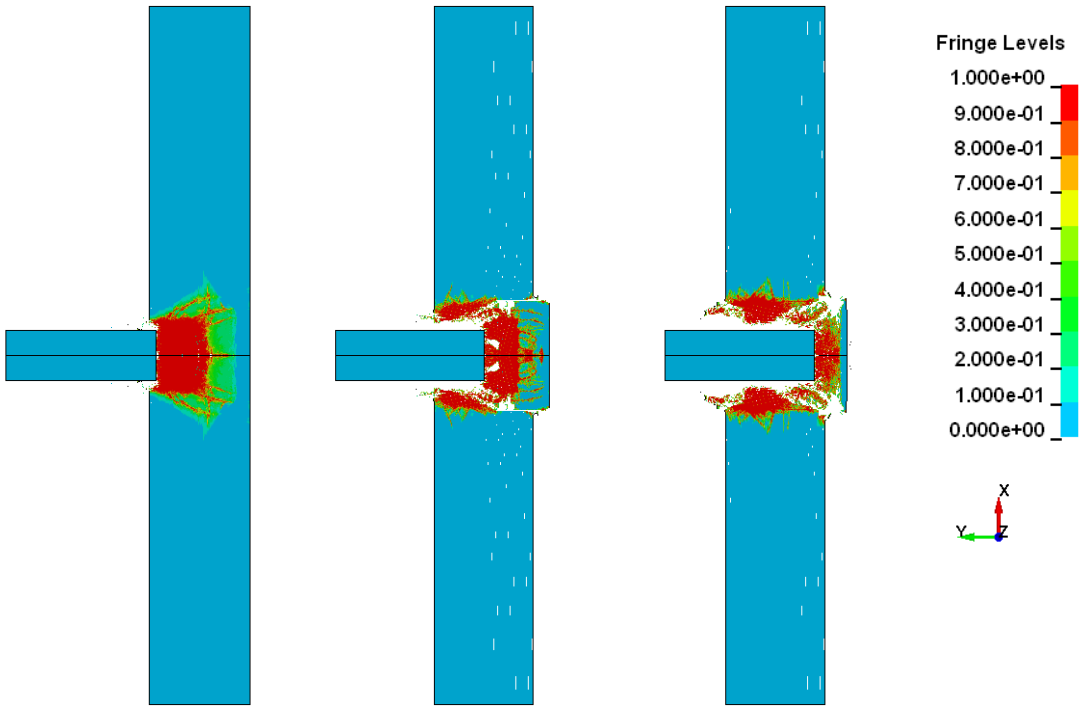

v_i = 27.0 m/s v_i = 35.7 m/s v_i = 56.8 m/s

Figure 6.16 NC-F0 concrete plates failure with damage fringe contour.

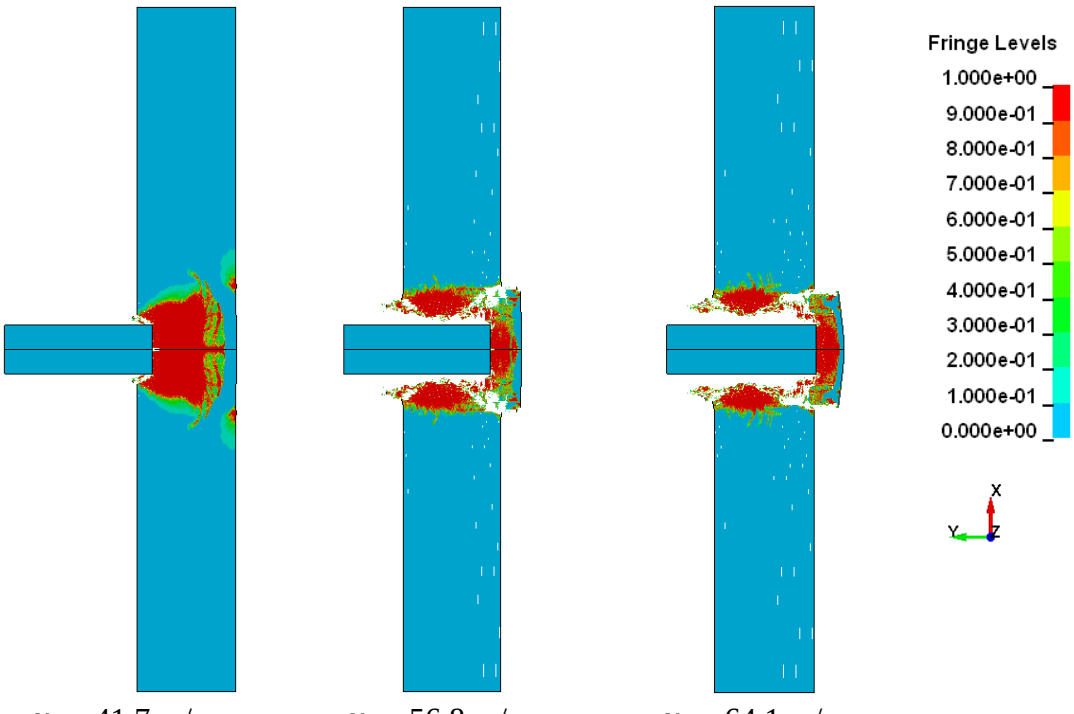

v_i = 41.7 m/s v_i = 56.8 m/s v_i = 64.1 m/s

Figure 6.17 NC-F2 concrete plates failure with damage fringe contour.

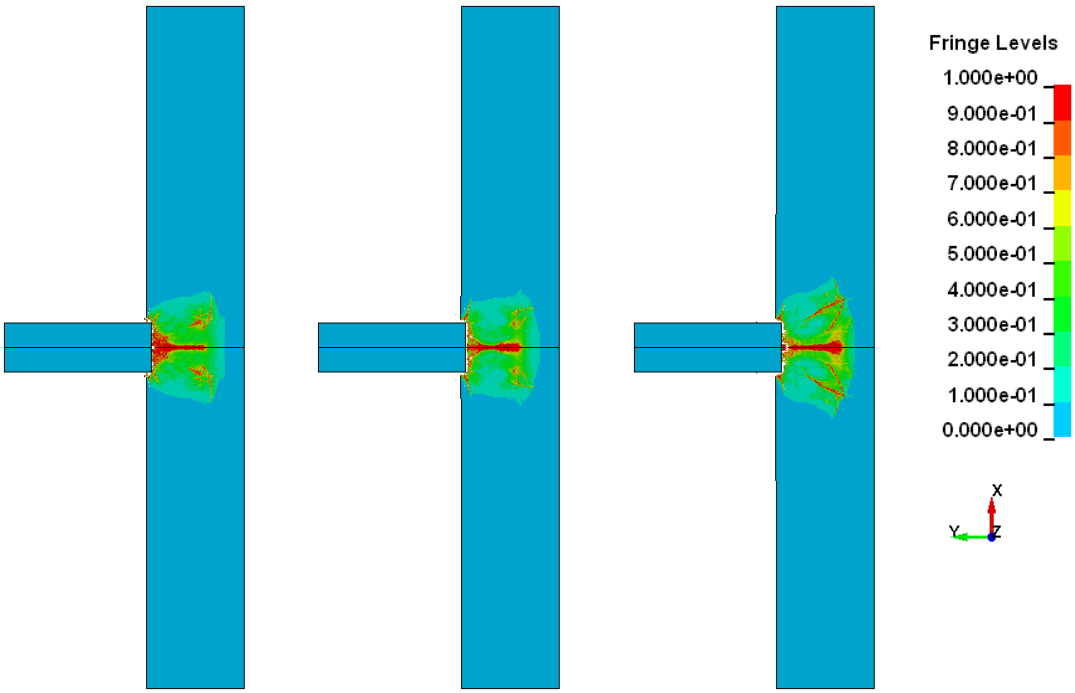

v_i = 76 m/s v_i = 85 m/s v_i = 104 m/s

Figure 6.18 RPC-F2 concrete plates failure with damage fringe contour.

6.6 Conclusions

Numerical analyses of penetration and perforation of concrete targets by high velocity ogive-nose steel projectiles are presented in this study. The Holmquist-Johnson-Cook (HJC) is incorporated for the concrete targets. Severe element distortion problem is mitigated by the use of the element erosion method. Principal strain values of 0.5 and -1.0 are selected as failure criteria for tension and compression failure, respectively. These values are verified with other published experimental results. It is noted that the failure patterns of concrete targets obtained numerically recreate those observed experimentally. The approach as presented herein adopts a consistent set of values of material properties and numerical parameters covering both the penetration and perforation of steel projectiles with ogive-nose into concrete targets with unconfined compressive strength of 48 MPa to 140 MPa, and hence, can be used for similar concrete penetration and perforation problems.

The modified Holmquist-Johnson-Cook (MHJC) model is adopted for penetration and perforation studies of concrete. The MHJC model consists of an improved strain rate expression and requires less number of material parameters. Good agreement with the experimental data is observed when the proposed model is implemented for perforation simulations of 48 MPa concrete by ogive-nose projectile. Although simulation results using both MHJC and HJC models exhibit similar results for 48 MPa concrete perforations, the MHJC model seems promising, and hence, employed for further study. Penetration study of normal concrete (NC) and reactive powder concrete (RPC) with compressive strength of 25 MPa and 178.3 MPa is also conducted using the MHJC model. Numerical results are reasonably consistent with the test observations. This indicates that the proposed model is robust and is able to emulate characteristics behavior of concrete subjected to high pressure, high strain rate and damage. This study is limited to normal weight and fiber-reinforced concrete with compressive strength ranging between 25 MPa to 180 MPa.

Chapter 7 Conclusion

7.1 Reviews on Completed Research Work

Material response under high velocity impact is considered in this study. Failure patterns of several materials, such as steel, aluminum, titanium and concrete are observed through numerical simulations. Various numerical methods for high velocity impact simulations are discussed. It is observed that Lagrangian finite element method is subjected to severe element distortion problem and requires special treatment, like element erosion approach, to complete the numerical simulations. In the element erosion method, severely distorted elements are removed from the numerical analysis based on user defined failure criteria. Although it is a simple approach, to the author's knowledge there are yet any direct techniques available to determine the element erosion criteria. Another option to avoid the severe element distortion problem is to adopt mesh free methods especially the smooth particle hydrodynamics (SPH) method. Because of their changeable nodal connectivity, the SPH method is capable of handling large deformation of structures with no severe element distortion problem. However, the SPH method has several disadvantages, namely tensile instability and computationally more expensive. Considering the advantages and disadvantages of both the FEM and SPH methods, the couple SPH-FEM (SFM) is proposed for the high velocity impact simulations. In the present study, perforation simulations of metal plates with relatively thinner thickness are performed using the SFM and perforation and/or penetration simulations of thicker concrete slabs are simulated using Lagrangian FE formulations with element erosion.

For a successful high velocity impact simulation, it is imperative to select a robust material model with a limited number of attainable material constants. Materials under high velocity impact are subjected to high pressure, high strain rate and damage, and the material models have to include these effects. Moreover, effect of temperature in metals is significant, and has to be considered. The Johnson-Cook (JC) material model consists of strength, strain rate, temperature and damage expressions. It is widely popular for high velocity impact simulations and has a vast library of material properties for various metals. In this study, the JC model is used for the high velocity impact simulations of steel and aluminum. Although the simulation results using the JC model give a good prediction of the test data, the model does not consider the temperature effect due to adiabatic condition. The strain rate expression of the JC model is also subjected to numerical problem and can be further improved. To rectify the problem, a new model namely modified Johnson-Cook (MJC) is proposed in this study.

For concrete, the Holmquist-Johnson-Cook (HJC) is implemented in this study. The HJC model is capable of handling high strain rate, pressure and damage, and is applied in several penetration and perforation simulations of concrete targets. However, the HJC model requires a good number of material constants to describe the pressure-volume behavior and the strain rate expression of the model does not consider the two distinct characteristics of concrete for strain rates below and above of the critical strain rate. Hence a simple but efficient material model known as the modified Holmquist-Johnson-Cook (MHJC) is developed for in this study.

7.2 Summary and Conclusion

A new material model for metals (MJC model) is developed. Temperature effect due to adiabatic condition is adopted in the MJC model. A simple but robust strain rate expression is also included. The MJC model parameters can be determined

from uniaxial tensile tests for metals at various strain rates and temperatures. Because of the improved computational model formulation, identification of the material parameters becomes straightforward comprising three steps. The proposed model is adopted through user defined material model and simulation results are verified against two different test procedures, (i) split Hopkinson pressure bar (SHPB) simulation of Ti-6Al-4V at various temperatures, and (ii) perforation of 6 mm thick Weldox 460 E steel plates by blunt projectile. Numerical results show good agreement with the experimental observations. Perforation simulation of steel plate also gives a detailed description of the plugging failure of the target plate.

The modified Holmquist-Johnson-Cook (MHJC) material model concrete is capable of handling high strain rates, large pressure and damage. Concrete exhibits a significant increase in strength above a critical strain limit value. A new expression independent of the compressive strength of concrete is proposed for strain rate above the critical strain limit. Below the critical strain value, strength increment with strain rate is negligible, and hence, ignored in the proposed model. Based on the experimental data, critical strain rate values of 40 s^{-1} and 0.2 s^{-1} are achieved for compression and tension, respectively. Pressure – volume relationship of concrete is important. Therefore, a three stage pressure – volume relation is implemented in the proposed model. The first and third regions characterize the elastic behavior of undamaged and fully compacted concrete. The second region is the transition region where cracks formed and compaction of concrete pores happens. Material properties obtaining procedure for the MHJC model is described and verified through perforation study of concrete with compressive 48 MPa concrete by ogive-nose steel projectile. Numerical residual velocities show a good correlation with the test observations.

Ballistic limit and residual velocities are the most common notions to determine the performance of structures against high velocity projectile impact. Failure patterns of the targets change with the target thickness to projectile diameter ratio and projectile nose geometries, which indeed affect the ballistic response of structures. The SFM is adopted to simulate high velocity perforation of steel and aluminum plates of different thicknesses perforated by steel projectiles with various nose geometries. The value of target plate thickness to projectile diameter ratio vary between 0.3 to 1.5 and three different projectile nose geometries such as, blunt, conical and ogival are used. The SFM method is able to predict rather accurately the different modes of failure, the projectile residual and ballistic limit velocities as compared with those observed in the test reported earlier except for those due to blunt projectile impact at low velocity of 170 m/s or less. This deviation in results is observed for the perforation of thin plates (especially for target plate with thickness to projectile diameter ratio of less than 0.5), as the change in failure pattern is not reflected in the solution obtained from the adopted method at low impact velocity mostly due to the tensile instability problem inherent in the SPH method. At lower range of impact velocities, FE solutions are in better agreement and may be adopted for this range of impact velocities. Although the SFM is less accurate at low velocity impact of 170 m/s and lower, the method is robust and efficient for high velocity impact penetration and/or perforation of metal target plates.

The modified Johnson-Cook (MJC) model are adopted in the SFM to simulate high velocity perforation of titanium, steel and aluminum alloy plates of different thicknesses impacted by steel projectiles with various geometries. Simulation results of Ti-6Al-4V target plate perforations using the fragment-simulating projectile (FSP) with impact velocities in the range of 1000 – 1300 m/s exhibit good agreements with the experimental observations. Numerical residual and ballistic limit velocities of

perforation tests provide a prediction of the experimental results. Numerical simulations also give a detail description of the perforation process which was not available for experimental case. The MJC model is also applied for perforation of steel and aluminum alloy target plates. Residual and ballistic limit velocities of the SFM (MJC) simulations are compared with the experimental and numerical simulations of JC model data. Like those of SFM (JC), the SFM (MJC) results are less accurate at low velocity impact problems, but the method provides promising results for high velocity impact problems especially in the ordnance velocity range. Failure patterns of the target plates agree well with the experimental observations. Although distinctions of numerical results for SFM (MJC) and SFM (JC) are small, SFM (MJC) provides better results due to the implementation of effective adiabatic temperature and strain rate expressions. Applications of the MJC model to wide varieties of material types validate the proposed model.

In order to avoid severe element distortion problem, element erosion technique is adopted in the finite element penetration and/or perforation analysis of concrete target materials. Residual velocities and penetration depths of ogive-nose steel projectiles are compared for the high velocity perforation and penetration tests, respectively of concrete target with various strengths and dimensions. Concrete under high velocity impact subjected to both tensile and compressive failure, and hence, both tensile and compressive failure criteria are adopted for element erosion. Based on the correlation with two perforations and one penetration test data, principal strain values of 0.5 and -1.0 are selected as erosion criteria for tensile and compressive failure, respectively. These erosion values are verified with other published experimental results. Failure patterns of the concrete targets obtained numerically resemble those of the experimental observations. The approach as presented herein adopts a consistent set of values of material properties and numerical parameters

covering both the penetration and perforation of steel projectiles with ogive-nose into concrete targets with unconfined compressive strength of 48 MPa to 140 MPa.

Penetration simulations of normal concrete without and with fiber reinforcement (NC-F0 and NC-F2), and high strength reactive powder concrete with fiber reinforcement (RPC-F2) have been conducted. The MHJC material model is implemented for concrete as a user defined material model. The element erosion option is integrated into the material model, and maximum and minimum strain values of 0.5 and -1.0 are adopted as erosion criteria respectively. Numerical penetration depths for all three concrete plates show reasonable correlation with test data. Furthermore, concrete plate failure patterns are consistent with the experimental observations. Close relation with the experimental results indicates that the MHJC model is capable of performing high velocity penetration and/or perforation with considerable success.

7.3 Recommendation for Future Studies

Possible areas of significance and further studies along the lines of present interest pursued herein and some of which are recommended as follows:

- To adopt the SFM for high velocity impact penetration/perforation studies of concrete targets.
- To resolve the inaccuracy problem of the SFM for relatively thin plate and/or low initial projectile velocity.
- Impact problems with large projectile deformation and damage can be studied using the SFM in the projectile, and use the SPH method at the front of the projectile where large deformation and damage is expected.
- Effect of confining pressure on strain rate during the dynamic tests of concrete can be studied to further improve the proposed concrete constitutive model.

- Numerical simulation of double layer composite with concrete as the front layer and metal as the backup layer can be carried out using the SFM and the proposed material models.

References

Abbadi, M., Hähner, P., Zeghloul, A., 2002. On the characteristics of Portevin-Le Chatelier bands in aluminum alloy 5182 under stress-controlled and strain-controlled tensile testing. Materials Science and Engineering: A 337, 194-201.

ACI Committee, 2001. Control of cracking in concrete structures. American Concrete Institute, Farmington Hills, Michigan.

Air Force Flight Dynamics Lab Tech Rpt. JTCG/AS-74-D-002, 1976. Wright-Patterson Air Force Base, Ohio.

Anderson, J.C.E., 1987. An overview of the theory of hydrocodes. International Journal of Impact Engineering 5, 33-59.

Attaway, S.W., Heinstein, M.W., Swegle, J.W., 1994. Coupling of smooth particle hydrodynamics with the finite element method. Nuclear Engineering and Design 150, 199-205.

Backman, M.E., Goldsmith, W., 1978. The mechanics of penetration of projectiles into targets. International Journal of Engineering Science 16, 1-99.

Bathe, K.-J., 1996. Finite Element Procedure. Prentice Hall, New Jersey.

Beissel, S.R., Johnson, G.R., 2000. An abrasion algorithm for projectile mass loss during penetration. International Journal of Impact Engineering 24, 103-116.

Bischoff, P.H., Perry, S.H., 1991. Compressive behaviour of concrete at high strain rates. Materials and Structures 24, 425-450.

Bodner, S.R., Partom, Y., 1975. Constitutive equations for elastic-viscoplastic strain hardening materials. Journal of Applied Mechanics 42, 385-389.

Bodner, S.R., Rajendran, A.M., 1995. On the strain rate and temperature dependence of hardening of copper, in: Schmidt, S.C., Tao, W.C. (Eds.), Proceedings of the Conference of the American Physical Society Topical Group on Shock Compression of Condensed Matter. American Institute of Physics Press, 499-502.

Bodner, S.R., Rubin, M.B., 1994. Modeling of hardening at very high strain rates. Journal of Applied Physics 76, 2742-2747.

Børvik, T., Clausen, A.H., Hopperstad, O.S., Langseth, M., 2004. Perforation of AA5083-H116 aluminium plates with conical-nose steel projectiles--experimental study. International Journal of Impact Engineering 30, 367-384.

Børvik, T., Forrestal, M.J., Hopperstad, O.S., Warren, T.L., Langseth, M., 2009. Perforation of AA5083-H116 aluminium plates with conical-nose steel projectiles - Calculations. International Journal of Impact Engineering 36, 426-437.

Børvik, T., Hopperstad, O.S., Berstad, T., Langseth, M., 2001a. A computational model of viscoplasticity and ductile damage for impact and penetration. European Journal of Mechanics - A/Solids 20, 685-712.

Børvik, T., Hopperstad, O.S., Berstad, T., Langseth, M., 2001b. Numerical simulation of plugging failure in ballistic penetration. International Journal of Solids and Structures 38, 6241-6264.

Børvik, T., Hopperstad, O.S., Berstad, T., Langseth, M., 2002. Perforation of 12 mm thick steel plates by 20 mm diameter projectiles with flat, hemispherical and conical noses: Part II: numerical simulations. International Journal of Impact Engineering 27, 37-64.

Børvik, T., Hopperstad, O.S., Langseth, M., Malo, K.A., 2003. Effect of target thickness in blunt projectile penetration of Weldox 460 E steel plates. International Journal of Impact Engineering 28, 413-464.

Burkins, M.S., Paige, J.I., Hansen, J.S., 1996. A ballistic evaluation of Ti-6Al-4v vs. long rod penetrators. U.S. Army Research Laboratory, Aberdeen Proving Ground, MD 21005-5066.

Burkins, M.S., Wells, M., Fanning, J., Roopchand, B., 2001. The mechanical and ballistic properties of an electron beam single melt of Ti-6Al-4V plate. U.S. Army Research Laboratory, Aberdeen Proving Ground, MD 21005-5066.

Buyukozturk, O., Nilson, A.H., Slate, F., 1971. Stress-strain response and fracture of a concrete model in biaxial loading. ACI Journal Proceedings 68, 590-599.

Camacho, G.T., Ortiz, M., 1997. Adaptive Lagrangian modelling of ballistic penetration of metallic targets. Computer Methods in Applied Mechanics and Engineering 142, 269-301.

Candappa, D.P., Setunge, S., Sanjayan, J.G., 1999. Stress versus strain relationship of high strength concrete under high lateral confinement. Cement and Concrete Research 29, 1977-1982.

Chen, E.P., 1990. Finite element simulation of perforation and penetration of aluminum targets by conical-nosed steel rods. Mechanics of Materials 10, 107-115.

Chen, E.P., 1993. Numerical simulation of perforation of concrete targets by steel rods, in: Chen, E.P., Luk, V.K. (Eds.), Advances in Numerical Simulation Techniques for Penetration adn Perforation of Solids, ASME Annual Winter Meeting, New Orleans, LA, 181-188.

Chen, X.W., Zhou, X.Q., Li, X.L., 2009. On perforation of ductile metallic plates by blunt rigid projectile. European Journal of Mechanics - A/Solids 28, 273-283.

Chou, P.C., Liang, D., Wu, L., Flis, W., 1988. Mesh rezoning for a dynamic triangular finite-elements hydrocode. Finite Elements in Analysis and Design 4, 175-192.

Clausen, A.H., Børvik, T., Hopperstad, O.S., Benallal, A., 2004. Flow and fracture characteristics of aluminium alloy AA5083-H116 as function of strain rate, temperature and triaxiality. Materials Science and Engineering A 364, 260-272.

Corbett, G.G., Reid, S.R., Johnson, W., 1996. Impact loading of plates and shells by free-flying projectiles: A review. International Journal of Impact Engineering 18, 141-230.

Corran, R.S.J., Shadbolt, P.J., Ruiz, C., 1983. Impact loading of plates - An experimental investigation. International Journal of Impact Engineering 1, 3-22.

Davies, E.D.H., Hunter, S.C., 1963. The dynamic compression testing of solids by the method of the split Hopkinson pressure bar. Journal of the Mechanics and Physics of Solids 11, 155-179.

Dey, S., 2004. High-strength steel plates subjected to projectile impact - an experimental and numerical study. Norwegian University of Science and Technology, Trondheim.

Dey, S., Børvik, T., Hopperstad, O.S., Langseth, M., 2007. On the influence of constitutive relation in projectile impact of steel plates. International Journal of Impact Engineering 34, 464-486.

Donzé, F.V., Magnier, S.-A., Daudeville, L., Mariotti, C., Davenne, L., 1999. Numerical study of compressive behavior of concrete at high strain rates. Journal of Engineering Mechanics 125, 1154-1163.

Dumoulin, S., Louche, H., Hopperstad, O.S., Børvik, T., 2010. Heat sources, energy storage and dissipation in high-strength steels: Experiments and modelling. European Journal of Mechanics - A/Solids 29, 461-474.

Dyka, C.T., Randles, P.W., Ingel, R.P., 1997. Stress points for tension instability in SPH. International Journal of Numerical Methods in Engineering 40, 2325-2341.

Farrokh, B., Khan, A.S., 2009. Grain size, strain rate, and temperature dependence of flow stress in ultra-fine grained and nanocrystalline Cu and Al: Synthesis, experiment, and constitutive modeling. International Journal of Plasticity 25, 715-732.

Follansbee, P.S., Frantz, C., 1983. Wave propagation in the Split Hopkinson Pressure Bar. Journal of Engineering and Technology 105, 61-66.

Forrestal, M.J., Frew, D.J., Hanchak, S.J., Brar, N.S., 1996. Penetration of grout and concrete targets with ogive-nose steel projectiles. International Journal of Impact Engineering 18, 465-476.

Forrestal, M.J., Luk, V.K., Brar, N.S., 1990. Perforation of aluminum armor plates with conical-nose projectiles. Mechanics of Materials 10, 97-105.

Forrestal, M.J., Okajima, K., Luk, K.V., 1988. Penetration of 6061-T651 aluminum targets with rigid long rods. Journal of Applied Mechanics 55, 755-760.

Freund, L.B., 1972. Crack propagation in an elastic solid subjected to general loading – I. Constant rate of extension. Journal of the Mechanics and Physics of Solids 20, 129-140.

Frew, D.J., Hanchak, S.J., Green, M.L., Forrestal, M.J., 1998. Penetration of concrete targets with ogive-nose steel rods. International Journal of Impact Engineering 21, 489-497.

Gary, G., Klepaczko, J.R., 1992. Essai de compression dynamique sur béton, GRECO Geomaterial scientific report, 105-118.

Gebbeken, N., Greulich, S., Pietzsch, A., 2006. Hugoniot properties for concrete determined by full-scale detonation experiments and flyer-plate-impact tests. International Journal of Impact Engineering 32, 2017-2031.

Gebbeken, N., Ruppert, M., 2000. A new material model for concrete in high-dynamic hydrocode simulations. Archive of Applied Mechanics 70, 463-478.

Gingold, R.A., Monaghan, J.J., 1977. Smoothed particle hydrodynamics - Theory and application to non-spherical stars. Royal Astronomical Society, Monthly Notices 181, 375-389.

Hallquist, J.O., 1998. LS-DYNA Theoretical Manual-Nonlinear Dynamic Analysis of Structures. Livermore Software Technology Corporation, Livermore, California, USA.

Hallquist, J.O., 2006. LS-DYNA Theory Manual. Livermore Software Technology Corporation, Livermore, California, USA.

Hanchak, S.J., Forrestal, M.J., Young, E.R., Ehrgott, J.Q., 1992. Perforation of concrete slabs with 48 MPa (7 ksi) and 140 MPa (20 ksi) unconfined compressive strengths. International Journal of Impact Engineering 12, 1-7.

Hatch, J.E., 1984. Aluminum: Properties and Physical Metallurgy. Aluminum Association Inc. and ASM International.

Holmquist, T.J., Johnson, G.R., Cook, W.H., 1993. A computational constitutive model for concrete subjected to large strains, high strain rates, and high pressures, 14th International Symposium on Ballistics, Quebec City, Canada, 591-600.

Hsu, T.T.C., Slate, F.O., Sturman, G.M., Winter, G., 1963. Microcracking of plain concrete and the shape of the stress-strain curve. ACI Journal Proceedings 60, 209-224.

Imran, I., Pantazopoulou, S.J., 1996. Experimental study of plain concrete under triaxial stress. ACI Materials Journal 93, 589-601.

Islam, M.J., Liu, Z.S., Swaddiwudhipong, S., 2011. Numerical study on concrete penetration/perforation under high velocity impact by ogive-nose steel projectile. Computers and Concrete 8, 111-123.

Johnson, G.R., 1977. High velocity impact calculations in three dimensions. Journal of Applied Mechanics, Transactions ASME 44, 95-100.

Johnson, G.R., 1994. Linking of Lagrangian particle methods to standard finite element methods for high velocity impact computations. Nuclear Engineering and Design 150, 265-274.

Johnson, G.R., Beissel, S.R., Holmquist, T.J., 1998. Computed radial stresses in a concrete target penetrated by a steel projectile, in: Jones, N., Talaslidis, D.G., Brebbia, C.A., Manolis, G.D. (Eds.), Structures Under Shock and Impact V. Computational Mechanics Publications, 793-806.

Johnson, G.R., Cook, W.H., 1983. A constitutive model and data for metals subjected to large strains, high strain rates and high temperatures, 7th International Symposium on Ballistics, The Hague, The Netherlands, 541-547.

Johnson, G.R., Cook, W.H., 1985. Fracture characteristics of three metals subjected to various strains, strain rates, temperatures and pressures. Engineering Fracture Mechanics 21, 31-48.

Johnson, G.R., Holmquist, T.J., 1994. An improved computational constitutive model for brittle materials, in: Schmidt, S.C., Shaner, J.W., Samara, G.A. (Eds.), High-Pressure Science and Technology - American Institute of Physics Conference Proceedings, 981-984.

Johnson, G.R., Petersen, E.H., Stryk, R.A., 1993. Incorporation of an SPH option into the EPIC code for a wide range of high velocity impact computations. International Journal of Impact Engineering 14, 385-394.

Johnson, G.R., Stryk, R.A., Beissel, S.R., 1996. SPH for high velocity impact computations. Computer Methods in Applied Mechanics and Engineering 139, 347-373.

Jones, N., 1983. Structural aspects of ship collisions, in: Jones, N., Wierzbickie, T. (Eds.), Structural Crashworthiness, Butterworths, London, 308-337.

Kapoor, R., Nemat-Nasser, S., 1998. Determination of temperature rise during high strain rate deformation. Mechanics of Materials 27, 1-12.

Khan, A.S., Huang, S., 1992. Experimental and theoretical study of mechanical behavior of 1100 aluminum in the strain rate range 10^{-5}-$104s^{-1}$. International Journal of Plasticity 8, 397-424.

Khan, A.S., Liang, R., 1999. Behaviors of three BCC metal over a wide range of strain rates and temperatures: experiments and modeling. International Journal of Plasticity 15, 1089-1109.

Khan, A.S., Sung Suh, Y., Kazmi, R., 2004. Quasi-static and dynamic loading responses and constitutive modeling of titanium alloys. International Journal of Plasticity 20, 2233-2248.

Kipp, M.E., Grady, D.E., Chen, E.P., 1980. Strain-rate dependent fracture initiation. International Journal of Fracture Mechanics 16, 471-478.

Kirk-Othmer, 2010. Kirk-Othmer Encyclopedia of Chemical Technology, in: Seidel, A. (Ed.), Encyclopedia of Chemical Technology, 5th ed. John Wiley & Sons, Inc., New Jersey, 838-867.

Krieg, R.D., Key, S.W., 1976. Implementation of a time dependent plasticity theory into structural computer programs. Constitutive Equations in Viscoplasticity: Computational and Engineering Aspects (American Society of Mechanical Engineers) 20, 125-137.

Leppin, S., Woodward, R.L., 1986. Perforation mechanisms in thin titanium alloy targets. International Journal of Impact Engineering 4, 107-115.

Li, Q.M., Meng, H., 2003. About the dynamic strength enhancement of concrete-like materials in a split Hopkinson pressure bar test. International Journal of Solids and Structures 40, 343-360.

Li, S., Liu, W.K., 2004. Meshfree Particle Methods. Springer.

Liang, R., Khan, A.S., 1999. A critical review of experimental results and constitutive models for BCC and FCC metals over a wide range of strain rates and temperatures. International Journal of Plasticity 15, 963-980.

Libersky, L.D., Petschek, A.G., 1991. Smooth particle hydrodynamics with strength of materials, in: Trease, H.E., Fritts, M.F., Crowley, W.P. (Eds.), Advances in the Free-Lagrange Method Including Contributions on Adaptive Gridding and the Smooth Particle Hydrodynamics Method: Proceedings of the Next Free-Lagrange Conference Held at Jackson Lake Lodge, Moran, WY, USA 3–7 June 1990. Springer Berlin / Heidelberg, 248-257.

Libersky, L.D., Petschek, A.G., Carney, T.C., Hipp, J.R., Allahdadi, F.A., 1993. High strain Lagrangian hydrodynamics: A three-dimensional SPH code for dynamic material response. Journal of Computational Physics 109, 67-75.

Liu, Z.S., 2002. Contact impact dynamic response of plate and shell structures, Department of Civil Engineering. National University of Singapore, Singapore, 248.

Liu, Z.S., Islam, M.J., Swaddiwudhipong, S., 2010. High velocity penetration/perforation using coupled smooth particle hydrodynamics-finite element method. International Journal of Protective Structures 1, 489-506.

Liu, Z.S., Swaddiwudhipong, S., Koh, C.G., 2002. Stress wave propagation in 1-D and 2-D media using smooth particle hydrodynamics method. Structural Engineering and Mechanics 14(4), 455-472.

Liu, Z.S., Swaddiwudhipong, S., Koh, C.G., 2004. High velocity impact dynamic response of structures using SPH method. International Journal of Computational Engineering Science 5, 315-326.

Lucy, L.B., 1977. A numerical approach to the testing of the fission hypothesis. Astronomical Journal 82, 1013-1024.

Macdougall, D.A.S., Harding, J., 1999. A constitutive relation and failure criterion for Ti6Al4V alloy at impact rates of strain. Journal of the Mechanics and Physics of Solids 47, 1157-1185.

Malvar, L.J., Crawford, J.E., Wesevich, J.W., Simons, D., 1997. A plasticity concrete material model for DYNA3D. International Journal of Impact Engineering 19, 847-873.

Malvern, L.E., Jenkins, D.A., Tang, D.A., Ross, C.A., 1985. Dynamic compressive testing of concrete, Proceedings of 2nd Symposium on the Interaction of Non-Nuclear Munitions with Structures, Florida, 194-199.

Mason, J.J., Rosakis, A.J., Ravichandran, G., 1994. On the strain and strain rate dependence of the fraction of plastic work converted to heat: an experimental study

using high speed infrared detectors and the Kolsky bar. Mechanics of Materials 17, 135-145.

McVay, M.K., 1988. Spall damage of concrete structures. Army Engineer Waterways Eexperiment Station Vicksburg Miss. Structures Lab, Vicksburg, Miss., 431.

Mellinger, F.M., Birkimer, D.L., 1966. Measurement of stress and strain on cylindrical test specimens of rock and concrete under Impact loading, Technical Report 4-46. U.S. Army Corps of Engineers, Ohio River Division Laboratories Cincinnati, Ohio.

Monaghan, J.J., Gingold, R.A., 1983. Shock simulation by the particle method SPH. Journal of Computational Physics 52, 374-389.

Montgomery, J.S., Wells, M.G.H., 2001. Titanium armor applications in combat vehicles. JOM Journal of the Minerals, Metals and Materials Society 53, 29-32.

Montgomery, R.S., 1976. Surface melting of rotating bands. Wear 38, 235-243.

Murray, Y.D., Lewis, B.A., 1995. Numerical simulation of damage in concrete. APTEK Inc. Colorado Springs Co.

Naka, T., Yoshida, F., 1999. Deep drawability of type 5083 aluminium-magnesium alloy sheet under various conditions of temperature and forming speed. Journal of Materials Processing Technology 89-90, 19-23.

Nemat-Nasser, S., Guo, W.-G., Nesterenko, V.F., Indrakanti, S.S., Gu, Y.-B., 2001. Dynamic response of conventional and hot isostatically pressed Ti-6Al-4V alloys: experiments and modeling. Mechanics of Materials 33, 425-439.

Pitler, R., Hurlich, A., 1950. Some mechanical and ballistic properties of titanium and titanium alloys. Watertown Arsenal Laboratory, Watertown, MA.

Polanco-Loria, M., Hopperstad, O.S., Børvik, T., Berstad, T., 2008. Numerical predictions of ballistic limits for concrete slabs using a modified version of the HJC concrete model. International Journal of Impact Engineering 35, 290-303.

Ravid, M., Bodner, S.R., 1983. Dynamic perforation of viscoplastic plates by rigid projectiles. International Journal of Engineering Science 21, 577-591.

Recht, R.F., Ipson, T.W., 1963. Ballistic perforation dynamics. Journal of Applied Mechanics 30, 384-390.

Riedel, W., Thoma, K., Hiermaier, S., Schmolinske, E., 1999. Penetration of reinforced concrete by BETA-B-500 numerical analysis using a new macroscopic concrete model for hydrocodes, International Symposium, Interaction of the Effects of Munitions with Structures.

Rösler, J., Harders, H., Bäker, M., 2007. Mechanical behaviour of engineering materials. Springer, Germany.

Ross, C.A., Jerome, D.M., Tedesco, J.W., Hughes, M.L., 1996. Moisture and strain rate effects on concrete strength. ACI Materials Journal 93, 293-300.

Ross, C.A., Thompson, P.Y., Tedesco, J.W., 1989. Split-Hopkinson pressure-bar tests on concrete and mortar in tension and compression. ACI Materials Journal 86, 475-481.

Schwer, L.E., Day, J., 1991. Computational techniques for penetration of concrete and steel targets by oblique impact of deformable projectiles. Nuclear Engineering and Design 125, 215-238.

Seo, S., Min, O., Yang, H., 2005. Constitutive equation for Ti-6Al-4V at high temperatures measured using the SHPB technique. International Journal of Impact Engineering 31, 735-754.

Shang, J.L., Shen, L.T., Zhao, J., 2000. Hugoniot equation of state of the Bukit Timah granite. International Journal of Rock Mechanics and Mining Sciences 37, 705-713.

Solberg, J.K., Leinum, J.R., Embury, J.D., Dey, S., Børvik, T., Hopperstad, O.S., 2007. Localised shear banding in Weldox steel plates impacted by projectiles. Mechanics of Materials 39, 865-880.

SSAB, 1999. Data sheet of Weldox 460.

Swaddiwudhipong, S., Islam, M.J., Liu, Z.S., 2011. High velocity perforation simulations of lightweight target plates using a modified Johnson-Cook model. International Journal of Aerospace and Lightweight Structures 1, 67-88.

Tai, Y.S., 2009. Flat ended projectile penetrating ultra-high strength concrete plate target. Theoretical and Applied Fracture Mechanics 51, 117-128.

Taylor, G.I., Quinney, H., 1934. The latent energy remaining in a metal after cold working. Proceedings of the Royal Society Series A 143, 307-326.

Taylor, L.M., Chen, E.P., Kuszmaul, J.S., 1986. Microcrack-induced damage accumulation in brittle rock under dynamic loading. Computer Methods in Applied Mechanics and Engineering 55, 301-320.

Tedesco, J.W., Powell, J.C., Ross, C.A., Hughes, M.L., 1997. A strain-rate-dependent concrete material model for ADINA. Computers & Structures 64, 1053-1067.

Tedesco, J.W., Ross, C.A., 1998. Strain-rate-dependent constitutive equations for concrete. ASME Journal of Pressure Vessel Technology 120, 398-405.

Tedesco, J.W., Ross, C.A., Kuennen, S.T., 1993. Experimental and numerical analysis of high strain rate splitting tensile tests. ACI Materials Journal 90, 162-169.

Wagenhofer, M., Erickson-Natishan, M., Armstrong, R.W., Zerilli, F.J., 1999. Influences of strain rate and grain size on yield and serrated flow in commercial Al-Mg alloy 5086. Scripta Materialia 41, 1177-1184.

Wilkins, M.L., 1978. Mechanics of penetration and perforation. International Journal of Engineering Science 16, 793-807.

Wingrove, A.L., 1973. The influence of projectile geometry on adiabatic shear and target failure. Metallurgical and Materials Transactions B 4, 1829-1833.

Woodward, R.L., 1979. Metallographic features associated with the penetration of titanium alloy targets. Metallurgical and Materials Transactions A 10, 569-573.

Woodward, R.L., 1984. The interrelation of failure modes observed in the penetration of metallic targets. International Journal of Impact Engineering 2, 121-129.

Zerilli, F.J., Armstrong, R.W., 1987. Dislocation-mechanics-based constitutive relations for material dynamics calculations. Journal of Applied Physics 61, 1816-1825.

Zerilli, F.J., Armstrong, R.W., 1990. Description of tantalum deformation behavior by dislocation mechanics based constitutive relations. Journal of Applied Physics 68, 1580-1591.

Zerilli, F.J., Armstrong, R.W., 1997. Dislocation mechanics based analysis of material dynamics behavior: enhanced ductility, deformation twinning, shock deformation, shear instability, dynamic recovery. Journal de Physique IV France 07, 637-642.

Zukas, J.A., 1990. High velocity impact dynamics. John Wiley & Sons, Inc., New York, 935.

Zukas, J.A., 1995. Numerical modeling of high velocity impact of non-metallic materials. High Strain Rate Effects on Polymer, Metal and Ceramic Matrix Composites and Other Advanced Materials, ASME 48, 49-62.

List of Publications

Journal Publications:

Swaddiwudhipong S., Islam M. J., Liu Z. S., 2010. High Velocity Penetration/Perforation Using Coupled Smooth Particle Hydrodynamics-Finite Element Method. International Journal of Protective Structures 1(4), 489-506.

Islam M. J., Liu Z. S., Swaddiwudhipong S., 2011. Numerical study on concrete penetration/perforation under high velocity impact by ogive-nose steel projectile. Computers and Concrete 8(1), 111-123.

Swaddiwudhipong S., Islam M. J., Liu Z. S., 2011. High velocity perforation simulations of lightweight target plates using a modified Johnson-Cook model. International Journal of Aerospace and Lightweight Structures 1(1), 67-88.

Liu Z. S., Swaddiwudhipong S., Islam M. J., 2011. Perforation of Steel and Aluminum Targets Using a Modified Johnson-Cook Material Model. Submitted for publication.

Islam M. J., Swaddiwudhipong S., Liu Z. S., 2011. Penetration and Perforation of Concrete Targets Using a Modified Holmquist-Johnson-Cook Material Model. Submitted for publication.

Conference Presentations:

Islam M. J., Liu Z. S., Swaddiwudhipong S., 2008. Coupled FE-SPH method for steel plate impact simulations, in: 4th International Conference on Advances in Structural Engineering and Mechanics (ASEM'08), Jeju, Korea.

Islam M. J., Swaddiwudhipong S., and Liu Z. S., 2008. Numerical simulations of concrete penetration/perforation when subjected to high velocity impact, in: 21st KKCNN Symposium on Civil Engineering, Singapore.